Stony Brook University

Development of the Simplified Land Model (SLM) and its application to the diurnal cycle of precipitation over land

A Dissertation Presented

by

Jungmin Lee

to

The Graduate School

in Partial Fulfillment of the

Requirements

for the Degree of

Doctor of Philosophy

in

Marine and Atmospheric Science

Stony Brook University

May 2016

Stony Brook University

The Graduate School

Jungmin Lee

We, the dissertation committee for the above candidate for the

Doctor of Philosophy degree, hereby recommend

acceptance of this dissertation.

Dr. Marat Khairoutdinov – Dissertation Advisor
Associate Professor
School of Marine and Atmospheric Sciences, Stony Brook University

Dr. Minghua Zhang - Chairperson of Defense
Professor, Dean of School of Marine and Atmospheric Sciences
School of Marine and Atmospheric Sciences, Stony Brook Universiyt

Dr. Brian A. Colle
Professor
School of Marine and Atmospheric Sciences, Stony Brook University

Dr. Andrew Vogelmann
Adjunct Assistant Professor
School of Marine and Atmospheric Sciences, Stony Brook University

Dr. Scott A. Denning
Professor
Department of Atmospheric Science, Colorado State University

This dissertation is accepted by the Graduate School

Charles Taber
Dean of the Graduate School

Abstract of the Dissertation

Development of the Simplified Land Model (SLM) and its application to the diurnal cycle of precipitation over land

by

Jungmin Lee

Doctor of Philosophy

in

Marine and Atmospheric Science

Stony Brook University

2016

The diurnal cycle of convection is a key to understanding the climate and weather in the context of the Earth's energy and water cycles. Yet, the well-observed late afternoon to early evening precipitation maximum over most of inland regions still remains one of the poorly understood features of continental convection. Many numerical weather and global climate models (GCMs) have had difficulty capturing the correct diurnal cycle of convection over land. Not only does this deficiency create a concern regarding the consistency of GCMs' physical parameterizations, but it also requires a better understating of physical processes that control the land-atmosphere interactions. Therefore, it is crucial to design models that can represent the coupling between land and atmosphere to advance our knowledge of the convection over land on subdiurnal timescales.

A Simplified Land Model (SLM) has been developed to be used in the System for Atmospheric Modeling (SAM) cloud-resolving model, which can explicitly resolve convection over land with prescribed surface fluxes but lacks a realistic scheme to represent the explicit land-atmosphere interaction. By design, the SLM is considerably simpler in its formulation than other, more sophisticated land models. It uses a minimalist set of external parameters to define the

vegetation and soil characteristics and physical process, and focuses mainly on the heat, moisture and momentum exchange between land and atmosphere. This allows coupled SAM-SLM model users to easily understand and modify the land surface component to meet their research requirements. Validation tests of SLM using measurements from several sites reveal that it is capable of reproducing rather well the observed surface radiation and enthalpy fluxes over various vegetated land sites. The coupled SAM-SLM model has been applied to a problem of diurnal development of clouds in the PBL over land as well as to an idealized case of the diurnal cycle of precipitation over 2D islands. The islands are of various sizes and are surrounded by an ocean using a radiative-convective equilibrium framework with prescribed and constant sea-surface temperature. The model is able to reproduce the observed timing of the precipitation maximum at 5 pm (17:00) local time for the inland regions of simulated islands far away from the sea-breeze zone. It has also been shown that the timing of precipitation can shift earlier in the case of warmer ocean. The sensitivity of the diurnal cycle of precipitation to planetary rotation as well as vegetation type and landmass size has also been tested. In particular, it has been found that, over large enough islands, changing the land cover from forest to grassland or baresoil can switch the convection regime from a regular diurnal cycle with the late-afternoon precipitation maximum to an organized propagating convection system with a timespan longer than 24-hour.

Table of Contents

List of Tables

Chapter 2 **page**

Chapter 4 **page**

List of Figures

Chapter 1 **page**

Chapter 2 **page**

Chapter 3 **page**

Chapter 4 **page**

Acknowledgments

I would like to express my sincere gratitude to my advisor **Professor Marat Khairoutdinov**. I would like to thank you for time, ideas and funding to my research and for helping me to complete the program even at hardship. Your advice on both research as well as on my career have been priceless. I would also like to thank my committee members, **professor Minghua Zhang, professor Brian Colle, professor Andy Vogelmann**, and **professor Scott Denning** for your brilliant comments, suggestions and warm encouragement through serving on this committee.

I also would like to thank **Dr. Behling, Dr. Byrne, Carol**, **Haewon and Maryann** who stayed by my side throughout the journey, and continued to remind myself who I was, who I am and who I can be. Special thanks to my family and my precious Miki for showing me the continuous support, care and love. In spite of the several setbacks at times, I could still enjoy the life and see the humor in it, and stay focused on my graduate study, thanks to all of you. None of this would have been possible without you fighting alongside me to strive to the goals. Although only my name appears on the cover, your contribution in this production will never go unnoticed.

The text of this dissertation in part is a reprint of the materials as it appears in Lee, J. M., and M. Khairoutdinov (2015), A Simplified Land Model (SLM) for use in cloud-resolving models: Formulation and evaluation, J. Adv. Model. Earth Syst., 7, 1368–1392. The co-author, **Professor Marat Khairoutdinov**, listed in the publication directed and supervised the research that forms the basis for this dissertation.

Chapter 1: Introduction

1.1 Background

Moist convection plays a major role in modulating energy and water budgets in the Earth's climate system. Clouds can shield the underlying surface from the solar radiation, while trapping the terrestrial radiation escaping to space (e.g., Mahrt 1991; Ek and Mahrt, 1994). The effect of radiation on the surface temperature is particularly strong over the land because of low heat capacity of the thermally active layer of soil and vegetation compared to the ocean. Therefore, the effect of clouds on the land surface can be dramatic, especially on the diurnal and sub-diurnal time scales. Because the exchange of heat, moisture and momentum between the land and overlying atmosphere strongly depends on the thermal contrast between the surface and the air above, the presence of clouds also can greatly modulate the surface fluxes (e.g., Businger et al., 1971; Betts and Silva Dias, 2010; Rabin et al., 1990; Ek and Holtslag, 2004). The modulation of the surface fluxes in response to radiation shielding by clouds may have implications on the temperature and moisture profiles in the PBL and, ultimately, the whole troposphere so that the moist convection may itself have to adjust. Thus, the clouds and the land processes are closely coupled, especially on sub-diurnal timescales.

Clouds also produce precipitation, which is a big part of hydrological cycle and a moisture source for land surface. The diurnal cycle of precipitation over land and over ocean has been observed to be quite different. Over land, the precipitation usually reaches a maximum during the late afternoon – early evening hours, while, over the ocean, it is most freqeunt during the early morning hours (e.g., Dai 2001; Nesbitt and Zipser, 2003; Dai et al., 2007; Yang and Slingo, 2001; Matsui et al., 2010). This is well demonstrated by the timing of the rainfall maximum over the continental United States shown in Fig. 1.1, obtained from the radar observations. One can see that most of the Eastern and Western United States have the rainfall maximum around 4-5 pm local

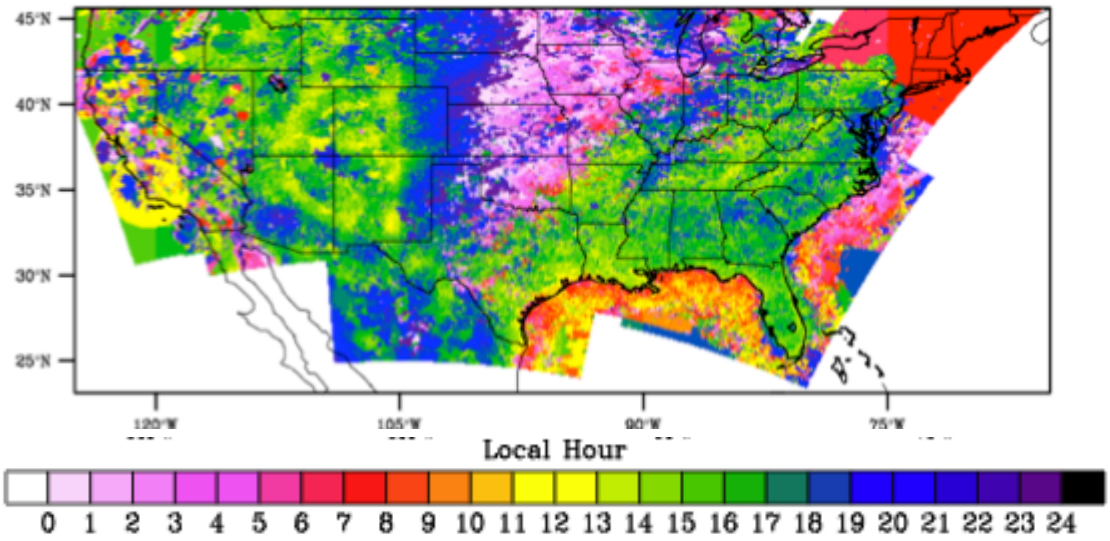

Figure 1.1. Map of maximum precipitation hour over the US from NCEP/CPC Four Kilometer Precipitation Set, Gauge and Radar (Stage IV analysis) averaged over 2002-2011 period (except 2003). [Dataset available online at http://rda.ucar.edu/datasets/ds507.5/.]

time. A notable exception is in the Mid-West, where the nocturnal rainfall maximum is not entirely due to local effects but rather due to eastward propagating meso-scale convective systems developing in the lee slopes of the Rockies (e.g., Carbone and Tuttle, 2008; Jiang et al., 2006). Meanwhile, the ocean areas off the East Coast of the United States have a clear early-morning maximum.

One of the long-standing problems with general circulation models, or global climate models (GCMs), is that the GCMs generally have a great deal of difficulty replicating the late-afternoon precipitation maximum observed over land. In fact, many GCMs produce a maximum that is too early, being around local noon, which is close to being in phase with the diurnal variation of surface solar heating. (e.g. Yang and Slingo, 2001; Dai 2006; Guichard et al., 2004). A successful prediction of the diurnal variation in the hydrological and energy cycles over land has been recognized to be an essential test for evaluation of the physical parameterizations in the atmospheric models (e.g., Slingo et al., 1987; Randall et al., 1991; Lin et al., 2000; Yang and Slingo, 2001; Betts and Jakob, 2002; Guichard et al., 2004). Hence, better understanding of physical mechanisms behind such a short timescale (diurnal/sub-diurnal) variation may further improve model parameterization schemes and lead to more accurate weather forecasting as well as the more reliable future climate change projections.

Dirmeyer et al. (2012) documented the large regional dependencies of the rainfall dynamics over land based on global observational studies. Their analysis suggests the variations in the timing of the rainfall peak are due to: 1) local convective instability by solar heating over relatively flat terrain, and 2) mesoscale circulation driven by differential surface heating for the elevated surfaces or land–ocean thermal contrast. Beyond the relatively well-understood mechanisms that explain the observed diurnal cycle of precipition in some regions under synoptic-scale forcing, there is still much left to be understood in terms of the mechanisms that modulate the diurnal cycle of precipitation over the landlocked regions, which have the least influence from the tropography or nearby ocean.

The remainder of this chapter reviews currently known mechanisms that control the diurnal cycle of precipitation over land and ocean, and the previous literature that documents the recent progresses made in the simulation of diurnal rainfall. The dissertation goals and the approach conclude this chapter.

1.1.1 Diurnal cycle of rainfall over land and thermodynamic processes

Even though the diurnal cycle of insolation is ubiquitous, diurnal cycle of rainfall has large geographical dependency (e.g. Wallace 1975; Gray and Jacobson, 1977; Yang and Smith, 2006; Johnson et al., 2010). As mentioned above, the diurnal cycle of rainfall over land mostly maximizes in the late afternoon to early evening lagging the solar forcing and corresponding surface latent and sensible heat fluxes by several hours. It has been generally agreed that under weak synoptic forcing, the daytime insolation fundamentally plays a crucial role in the development of deep convection over land (Wallace 1975; Dai 2001). The surface is quickly warmed by solar radiation after the sunrise, and the resultant turbulence erodes the shallow stable boundary layer formed the night before. After reaching the base of a weakly stable residual layer, the deepening of the convective boundary layer accelerates. Convective eddies in PBL redistribute the heat and moisture vertically, and promote the deepening of the PBL by entraining air from the free troposphere. If the moist air parcel is lifted, it cools adiabatically and may eventually become saturated. Any excess water vapor in the moist air parcel condenses out to form a cloud. Then, the release of latent heat during the condensation process provides additional buoyancy to the parcel. The release of latent heat partially offsets the cooling by adiabatic expansion, thus the moist air is

expected to be more buoyant than the dry air. Therefore, moistening of PBL from the surface fluxes can theoretically induce the quick growth and the subsequent generation of deep convection from the added buoyancy. However, the exact mechanism that is responsible for such a pronounced 'lag' between the surface forcing maximum and rainfall maximum over land is not well understood.

Beyond boundary layer, the low-tropospheric humidity can also be important for development of deep convection. Guichard et al. (2004) emphasized the importance of the gradual moistening of free troposphere to decouple the phase of surface heat fluxes and the rainfall maximum. Similarly, other studies (Derbyshire et al., 2004; Kuang and Bretherton, 2006) pointed out the important role of the free tropospheric humidity in the development of deep clouds. Mixing of cloudy air with the dry environmental air by entrainment induces evaporative cooling, hence the negative buoyancy; thus, until the atmosphere has a certain elevated level of humidity, the growth of clouds by mixing may be delayed or even suppressed. Chaboureau et al. (2004) suggested the sensitivity of the simulated deep convection initiation to the low level humidity and found that when the air around the cloud base is close to being saturated, their model tended to initiate deep convection.

Many studies have highlighted the role of the convectively generated cold pools in the gradual transition from shallow to deep convective regimes (e.g., Tompkins 2001; Khairoutdinov and Randall, 2006; Kuang and Bretherton, 2006). Although the evaporatively cooled sub-cloud layer provides unfavorable conditions to sustain the existing convection because of low equivalent potential temperature and high CIN (convective inhibition; Zipser 1977), the cold pool spreads out as a density current, and it is conducive to a formation of new and bigger clouds cells due to the enhanced local moisture convergence over the spreading edges (e.g., Khairoutdinov and Randall, 2006). The common finding of the aforementioned studies has been that the wider clouds are less likely to be diluted by the entrainment of the environment air, preserving undiluted core, and thus have higher chance to grow deeper. This notion has further been supported by the subsequent studies (e.g., Böing et al., 2012; de Rooy et al., 2013). Later, Schlemmer and Hohenegger (2014) have also confirmed that the generation of bigger clouds by the cold pool dynamics does indeed accelerate the transition from shallow to deep convection.

Another meteorological variable that has been known to control the diurnal cycle of precipitation is the lapse rate of the lower troposphere. Environmental temperature is known to

control the initiation of deep convection by changing the level of free convection (LFC; Ziegler et al., 1997; Johnson and Mapes, 2001). Houston and Niyogi (2007) found that the initiation of deep convection can be controlled by the temperature lapse rate above the LFC ("active cloud-baring layer"). In their study, deep convection does not begin when the lapse rate is smaller than a certain critical value, even though the air parcels can potentially reach the LFC. They suggest that the parcels lose more buoyancy by entrainment than gained by lifting. Thus, the more unstable the environment is in comparison to the critical lapse rate, the easier the initiation or transition of clouds to deep convection becomes. Wu et al. (2009) also suggested that the transition through the different convection regimes is highly dependent on the timing when the lapse rate of virtual potential temperature of clouds exceeded that of the environment, that is, when the cumulus clouds growing from the turbulent eddies in the convective boundary layer becomes suddenly positively buoyant at the top of PBL.

Observational study by Zhang and Klein (2010) over the Atmospheric Radiation Measurement (ARM) Program's Southern Great Plains (SGP) site have corroborated the importance of the relative humidity and mid-tropospheric stability at 2-4 km altitudes for the shallow-to-deep transition. Supporting previous modeling studies, they found that the high humidity in the few kilometers above the boundary layer prevents clouds from losing buoyancy by entrainment, while the increased lapse rate in mid-troposphere directly increases the buoyancy when the parcel is lifted, with both effects favoring the initiation of deep convection.

1.1.2 Diurnal cycle of rainfall over land and mesoscale circulations

In this section, we review the dynamic mechanisms that may help the rainfall to maximize in the late afternoon – late afternoon.

Several observational studies (e.g., Holton 1967; Wallace 1975) argued that the delayed precipitation maximum could be attributed to the enhancement of the mass convergence and mechanical convection at the top of PBL. Such convergence can be caused by coastal land-sea breeze circulation, heating over elevated topography and the associated lifting, and also by frictional drag associated with the diurnal variations in the static stability.

The diurnal land-ocean temperature contrast arises from the differences in heat capacity of land and the ocean, with the latter being much larger. The resultant thermally induced mesoscale

land-sea breeze circulation can affect the development of convective systems in coastal areas (Miller et al., 2003). Embedded in the circulation, the low-level flow is directed to the warmer land surface with the flow convergence located over land, which promotes the convective lifting over sea breeze front. As a result, a cloud system develops a narrow band parallel to the coastline favoring precipitation in the late afternoon. A good example of such process is a development of late afternoon thunderstorms over Florida peninsula (Boybeyi and Raman, 1992). Initiation of moist convection by the sea breeze fronts has been extensively documented by both observational and modeling studies (e.g., Estoque 1961; Pielke 1974; Simpson et al., 1977; Kingsmill et al., 1995; Shepherd et al., 2001; Fovell et al., 2005; Carbone et al., 2000; Chemel et al., 2009). Due to the land-sea temperature contrast, surface convergence of air flow is induced, so that the cooler, denser marine air collides with warmer, lighter continental air mass, initiating the frontogenesis. Uplift over the sea breeze front can support the formation of clouds provided enough moisture supply. Inland penetrating sea breeze fronts have been observed to collide with other fronts and form even stronger convection in the late afternoon (Saito et al., 2001; Qian 2008). When the temperature contrast reverses at night, the precipitation over land is suppressed under the subsidence branch of the land breeze circulation, while there is net ascent and precipitation over the ocean, mostly with drizzle or light rain that maximizes early in the morning before the land breeze reverses into the sea breeze. The vertical extent of the sea breeze circulation is generally too shallow to initiate the deep convection. However, especially in the subtropics and tropics, the deep convection can be initiated with the high-humidity maritime air supplied by the sea breeze front, which may lower the lifting condensation level (LCL) and the level of free convection (LFC).

Thermally direct mesoscale circulation has known to be another mechanism that can trigger convection over land. One example is the differential heating over the sloping terrain or elevated land in comparison to the surrounding areas. The surface temperature at higher altitudes rises more quickly during daytime and falls more rapidly during nighttime in comparison to the air temperature at the same altitude in the atmosphere, which creates pressure gradients and upslope circulations that reach their maximum intensity in the late afternoon, and downslope flows at nighttime (e.g., McNider and Pielke 1984). During the day, the upslope flow converges near the top of the mountains, providing the lifting necessary for the formation of thunderstorms, and the subsequent propagation towards the lower elevations. By similar mechanism, the precipitation

systems first appear over the lee slopes of the Rockies in the late afternoon, and then travel eastward. As the result, the high plains east of Rockies tend to have nocturnal rainfall maximum, while the further eastward low plains have the early morning maximum (e.g., Jiang et al., 2006; Carbone and Tuttle, 2008; Pritchard et al., 2011). Similarly, large variability in the rainfall peak timing in some regions can be due to the propagation of the organized moist convective systems, which tend to form the previous day in response to the surface solar heating (e.g., Mapes and Houze, 1993; Chen and Houze, 1997; Sherwood and Wahrlich, 1999).

Land surfaces with significant heterogeneity in their vegetation cover and soil moisture, partition differently the net absorbed radiation into sensible and latent heat fluxes (Giorgi and Avissar, 1997), which create a horizontal gradient of PBL heating. Recent cloud-resolving modeling studies with interactive land models have shown that the organized mesoscale circulations may indeed arise over the heterogeneous land surfaces following the surface heating variability, which may further affect the location and timing of the development of the deep precipitating clouds (van Heerwaarden and Vilà-Guerau de Arellano, 2008; Garcia-Carreras et al., 2011; Huang and Margulis, 2013; Kang and Bryan, 2011; Rieck et al., 2014, 2015).

1.1.3 Contrast in the diurnal rainfall variability over land and ocean

The rainfall over the ocean generally has a maximum in the late night - early morning hours. During the day, the absorption of solar radiation by the water vapor tends to stabilize the troposphere, supressing convection. At night, the radiative cooling tends to distabilize the troposphere, and the resultant deep convection would enhance radiative cooling at cloud anvils and warming by absorbing the terrestrial infrared radiation at cloud bases. These vertical heating anomalies associated with clouds would continuously destabilize the cloud layer and maintain the cloud structures over night (Dudhia 1989; Xu and Randall, 1995; Sui et al., 1997). Another mechanism for the nighttime rainfall maximum over ocean is the propagation of gravity waves excited from strong convection over land in the previous late afternoon, especially forced by the topography effects (e.g., Liu and Moncrieff, 1998; Zuidema, 2003; Mapes et al., 2003; Kikuchi and Wang, 2008; Houze and Betts, 1981; Mori et al., 2004; Zhou and Wang, 2006). A detailed review of the various mechanisms that would explain the early morning peak of precipitation over ocean is offered by Yang and Smith (2006). Some regions over ocean also have been reported to

show a diurnal life cycle of deep convection with a late afternoon precipitation peak (e.g, Hendon and Woodberry, 1993; Chen and Houze, 1997; Johnson et al., 2001). The reason for this different characteristic of convection over ocean is associated with with the synoptic weather condition. Under clear and calm weather conditions, the sea surface temperature can reach a maximum in the afternoon, although the range is small, and promote the occurrence of the deep convection.

Besides the timing of the precipitation maximum, the intensity also has a large contrast between land and ocean. In coastal areas, the difference could be due to the sea breeze circulations being stronger than the land breeze circulations (e.g., Burpee and Lahiff, 1984). Over land masses in general, there is stronger diurnal cycle of temperature and sensible heat fluxes, which drives a deeper planetary boundary layer, and leads to bigger thermals and updrafts with less entrainemnt (Jorgensen and Lemone, 1989; McCaul and Cohen, 2002; Zipser 2003). Also, the differences in rain characteristics over land and ocean can be due to very different concentrations and composition of aerosols, which can have a strong effect on cloud microphysics (e.g., Williams et al., 2002). The topography effects and the stronger turbulence from the higher level of surface roughness can also enhance precipitation over land relative to the ocean (Souza et al., 2000; Ekman et al., 2004).

1.1.4 Improvement in the simulation of the diurnal cycle of rainfall

Despite the improvement in understanding of the mechanisms that drive the diurnal cycle of convection over land, many global climate models (GCMs) have shown difficulty in obtaining the correct representation of the observed timing of the rainfall maximum over land. Many studies (e.g., Yang and Slingo 2001; Betts and Jakob 2002; Dai and Trenberth 2004; Bechtold et al., 2004) reported that many GCMs have convection onset that is too soon after sunrise and a precipitation maximum that is too early, being around local noon. This rather common behavior of many GCMs has been generally blamed on the deficiencies of the convection parameterization schemes. For example, Arakawa and Kitoh and Arakawa (2005) employed a high-resolution GCM with a 20 km grid spacing over the Maritime Continent to see whether the model is capable of replicating a realistic land-sea breeze and orographic influences on convection, and the associated diurnal cycle. Their relatively high-resolution simulations of the diurnal cycle of precipitation over the inland region of a relatively large sized island such as Borneo still remained rather poor with a maximum

that is too early. Apparently, the 20-km grid spacing was still too coarse to represent the mesoscale circulations associated with the coastal convection.

To avoid the cumulus parameterization problem altogether, a new modeling framework, named super-parameterization, or Multi-scale Modeling Framework (MMF), has been proposed, where a two-dimensional cloud-resolving model (CRM) replaces all the cloud parameterizations including the cumulus parameterization in each GCM grid column (Grabowski 2001; Khairoutdinov and Randall, 2001). For example, Khairoutdinov and Randall (2001) have developed a super-parameterized version of the National Center for Atmospheric Research (NCAR) Community Atmosphere Model (CAM) called SP-CAM, using a 2-D CRM as a super-parameterization. The performance of SP-CAM in simulating the diurnal cycle of precipitation has been reported by several studies (e.g., Khairoutdinov et al., 2005; DeMott et al., 2007; Zhang et al., 2008; Pritchard and Somerville, 2009a, b; Pritchard et al., 2011). Among them, Khairoutdinov et al. (2005) and DeMott et al. (2007) found that the SP-CAM reproduced the observed late afternoon (early morning) precipitation maximum over land (ocean) in the tropical and extra-tropical regions, while CAM has a tendency to produce too early precipitation maximum over land. Zhang et al. (2008) also found that the SP-CAM simulation of the diurnal phase of rainfall is similar to observations both over tropical ocean and land; however, the dry biases remain. Tao et al. (2009) used their own MMF developed at NASA Goddard to show that it also replicated the diurnal cycle of rainfall over the South America and Center Africa during summer. Pritchard et al. (2009) reported the detailed analysis of SP-CAM results with the emphasis on the diurnal cycle of rainfall. SP-CAM was successful at reproducing the diurnal cycle of rainfall with large amplitude (e.g., tropical land and ocean), as well as the coastal diurnal rainfall, where the sea breeze mesoscale circulations were well captured by SP-CAM. At the same time, the model overestimated the diurnal amplitudes over the regions where a weak diurnal cycle is typically observed (e.g., open ocean), and it did not produce the topography-induced nocturnal maximum of precipitation observed over the Central U.S. However, later, Pritchard et al. (2011) was able to reproduce the eastward propagating mesoscale convective systems over the Central U.S. in the updated version of SP-CAM with a different dynamical core that retains the sub-grid response rather than smearing it out. Generally, the overall conclusion from the aforementioned studies is that a more realistic treatment of deep convection as in MMF approach improves simulations of

the diurnal cycle of convection over land. However, the exact reason for the improvement remains unclear.

One method to improve the parameterization schemes used in GCMs is to take advantage of higher resolution simulations performed using CRMs, to supplement the insufficient observations. Several idealized CRM studies, based on observations over the ARM SGP, verified that a gradual transition from shallow cumulus to deep convection during daytime resulted in later onset of convection and delayed precipitation maximum (e.g., Bechtold et al., 2004; Chaboureau et al., 2004). For example, Bechtold et al. (2004) proposed that such difficulty shared by many GCMs might be attributable to the inability of a single convective scheme to distinguish between the shallow and deep convective clouds. Separate treatment of shallow cumulus clouds and deep convection parameterizations has indeed shown to improve the representation of the diurnal cycle of convection in GCMs (e.g., Rio et al. 2009). Also, many CRM studies (e.g. Khairoutdinov and Randall, 2006; Kuang and Bretherton, 2006; Del Genio and Wu, 2010) have found that the impact of entrainment on the developing cloud system is inversely proportional to the horizontal cloud size, so that, until a certain cloud size is reached, no transition from shallow to deep convection can occur. Those findings have been applied to several GCMs by altering entrainment rates in the convective parameterization schemes (e.g., ECMWF model in Bechtold et al., 2004; Regional Climate Model (RegCM) in Wang et al., 2007; Unified Model (UM) in Stratton and Stirling, 2012). All of them have shown improved performance of simulating the diurnal cycle of the rainfall.

Albeit with high computational costs, there has been attempts to use a global cloud-resolving model. One such model, NICAM, has been used to explicitly resolve most of convective and mesoscale circulation to study the diurnal cycle of precipitation (Sato et al., 2009). The overall performance of the NICAM generally exceeded the performances of the conventional GCMs in simulating the hydrological cycle and precipitation variability, except over the large islands. The simulated diurnal rainfall over the central regions of large islands has been shown to exhibit a precipitation maximum that is too early; however, the mechanism behind such a deficiency has not been well understood.

As mentioned above, the MMF has been consistently better at reproducing the diurnal cycle of precipitation in comparison to the conventional GCMs. Also, the knowledge obtained from the high resolution LES/CRM studies, such as reported by Khairoutdinov and Randall (2006), have been used to make improvements in the convective parameterization schemes in GCMs with the

results showing some promise. However, many of the previous studies have had a tendency to focus on improving the results obtained using the convective parameterization schemes, and ignore the dynamically interactive processes between the land and atmosphere. In particular, the GCMs tend to ignore the sub-grid scale interactions between the land surface and convection. For instance, GCMs may have a land scheme that computes the surface heat fluxes in response to a particular atmospheric state (such as temperature, specific humidity, wind, precipitation, radiation at a reference level), and the bottom boundary of atmosphere receives the surface heat fluxes computed by the land scheme. However, due to the coarse scales resolved by the GCM (O(100km)), the sub-grid variability is generally ignored, which may distort the response of the moist convection to the surface heating. In the MMF, convection is explicitly resolved by the CRM on much finer scales (O(1km)); however, the surface fluxes are still computed by the land scheme using GCM grid. Therefore, the land and atmosphere are still not properly coupled to each other. The reproduction of the correct diurnal cycle of precipitation in MMF may be a result of processes different than in nature because the PBL turbulent eddies cannot be properly resolved even when using 1 km grid spacing in the embedded CRM.

1.2 Study goals and approach

In nature, land surface thermal properties are characterized by a well pronounced variability at sub-daily time scales. The land surface heats up quickly by the solar radiation and the partitioning of the resultant surface heat flux into sensible and latent heat fluxes are highly dependent upon the bulk land surface properties (e.g., vegetation type, soil moisture content, etc.). Interactions between the land surface and overlying atmosphere redistribute the heat and moisture within the planetary boundary layer (PBL), which in turn affects the strength and phase of the diurnal cycle of convection. Moist convection over land is hence influenced by a variety of different mechanisms, all interacting among themselves. Therefore, any study of moist convection over land would require understanding the interactions of various processes at the various time and spatial scales in the dynamically coupled land - atmosphere system.

The application of LES/CRM to the diurnal-cycle studies over land have been highly dependent upon the availability of observational data, as the surface fluxes have usually been prescribed in those models. One of the reasons is lack of land-surface schemes in many LES/CRM

models that are usually used in idealized studies of convection. Due to prescribed surface fluxes, changes in the near-surface atmosphere have no feedback into the state of the land surface, which has limited our ability to study land-atmosphere coupling and, consequently, the diurnal development of moist convection over land in many previous idealized CRM/LES studies. Thus, the fine-resolution LES/CRM simulations that explicitly resolve interactions between land, boundary layer, and convection are needed to study the physical processes over land.

The main scientific objective of this dissertation is to improve understanding of the physical mechanisms that control the diurnal cycle of precipitation over land by using a high-resolution cloud-resolving model coupled to a newly developed land model, in which the land and atmosphere dynamically interact with each other. Using this modeling tool, the diurnal cycle of convection over islands of various sizes is analyzed for different processes: local thermodynamic effects of different vegetation types, the large scale impact of changing sea surface temperature of the surrounding ocean, and also the effect of adding the planetary rotation. The repeating diurnal cycle of rainfall will be examined after the land-ocean-atmosphere system approaches a state of quasi-equilibrium on the diurnal scales, rather than a specific convection event that may depend highly on the initial conditions.

The specific questions addressed by this dissertation are as follows:

- Can a simplified version of a land model coupled with a cloud-resolving model represent the land-atmosphere interactions via turbulent exchange of heat, moisture and momentum?
- Can such a modeling framework reproduce the observed diurnal evolution of PBL and convective systems over various land surfaces?
- Is there a sensitivity of diurnal development of convective systems over land to vegetation type?
- How does the landmass size may affect the development and evolution of precipitation on the diurnal time scales?
- How is the diurnal cycle of precipitation over land affected by the sea-surface temperature of the ocean surrounding a landmass?

- What are the systematic differences in the simulated diurnal cycle of precipitation over land under relatively large and small planetary rotation, which characterizes midlatitudes and the deep tropics, respectively?

The rest of this dissertation is composed of three main parts. Chapter 2 describes a newly developed land model that uses a relatively limited set of externally controlled parameters, compared to the mainstream land models, and the evaluation of its performance against the observation data at several sites covering different land types. Chapter 3 introduces the modeling framework of land model coupled to a CRM, which is used throughout the remaining part of the dissertation research. Chapter 3 also shows the results of simulating the daytime development of shallow clouds over land, and the sensitivity to the soil moisture and vegetation types. Chapter 4 applies the new model to simulate the diurnal cycle of convection over islands of various sizes surrounded by the ocean. Chapter 5 summarizes the findings of this thesis and discusses potential future research.

Chapter 2: Development of Simplified Land Model (SLM) and its validation

2.1 Introduction

Over time, a wide diversity of land surface schemes has been emerged with various levels of complexity. Land models (LMs) have evolved to encompass a wide range of land surface characteristics and processes such as, for instance, river discharge, snow/ice treatment, land surface sub-grid inhomogeneity, regional geography, vegetation dynamics, biogeochemical recycling among land, vegetation and atmosphere, among others. Consequently, the LMs are loaded with a large number of empirical parameters. However, it is uncertain whether those details and complexity are essential for qualitative understanding of such interactions on the diurnal time scales, especially when idealized simulations are carried out with large-eddy simulation (LES) or cloud-resolving models (CRMs). In my dissertation research, I developed a somewhat idealized or simplified land surface model that would not be simply treated as a 'black box' with large number of parameterizations and prescribed parameters but, rather, be easy to understand and, most importantly, easy to modify and improve by other users.

This chapter documents a newly developed land model, named the Simplified Land Model (SLM) that has been specifically designed to be coupled to the System for Atmospheric Modeling (SAM; Khairoutdinov and Randall, 2006) CRM. While it has a relatively limited set of externally specified parameters compared to mainstream land models, it will be shown to still be physically consistent with our understanding of the processes that are essential for the atmosphere-vegetation-soil interactions, particularly, on the diurnal time scales.

This chapter is organized as follows. The existing land models will be briefly reviewed in Section 2.2. A detailed description of the equations and parameters used in SLM is presented in Section 2.3. Appendix B contains the entire list of variables and parameters used in SLM. Section 2.4 presents the result of SLM performance tests that compares the evolution of simulated surface

fluxes and soil variables to summertime observations. Section 2.5 discusses the uncertainties related with the empirical parameters that define the land surface characteristics and its impact on the hydrological cycle. Section 2.6 summarizes this chapter.

2.2 History of modeling land surface processes

Here is a brief review of other land models that had an important influence on the SLM development. This section heavily drew on the historical review by Yang (2004).

It was three decades ago when the land schemes became part of GCMs (Dickinson et al., 1988; Sellers et al., 1986; Abramopoulos et al., 1988). Before that, the ground hydrology was typically represented by the "bucket model" (Manabe 1969). In that simple model, the soil is modeled as a water-filled bucket that is replenished by precipitation and drained by evaporation. If the moisture amount exceeds a certain capacity, the excess is lost out of a grid box as a runoff. Manabe's model employed a linear dependence of evaporation on soil moisture, which made the results rather unrealistic due to the nonlinearity of such a process (Sellers and Dorman, 1987). Also, the bucket representation of hydrology was based on diurnally averaged data; therefore, it might not be adequate for a GCM that allows for diurnally varying insolation.

Deardorff (1978) was the first who added a simple representation of vegetation to modeled land surface processes. His model had a layer of vegetation with a two-layered soil. Evaporation was computed from the soil moisture and water interception on the canopy, transpiration from the dry part of vegetation, and a force-restore model was applied to the heat and moisture transport between upper and deeper soil layers. The structure of his model has become an archetype for the future more sophisticated contemporary land schemes.

Among the early versions of land models was also the Biosphere-Atmosphere Transfer Scheme (BATS) developed by Dickinson et al. (1986). A single vegetation layer and three soil layers were used with 8 prognostic variables (temperature and water storage of the canopy, topsoil and root zone, total soil water, and snow coverage). The heat capacity and photosynthetic process of vegetation were ignored. The soil temperature was determined by force-restore model of Dickinson (1988). Effects of snow was applied to the soil thermal properties, albedo and surface fluxes.

The first generation of the Simple Biosphere Model (SiB; Sellers et al., 1986) employed two vegetation layers (upper story and ground cover) and 3 soil layers with 8 prognostic equations (temperature of the canopy, ground cover and deep soil layer, and water storage in each vegetation layer and each soil layer). Ground vegetation cover and the soil surface were assumed to share the same temperature. The main feature of SiB was the inclusion of 12 types of vegetation; the properties of each biome controlled the transpiration, radiation absorption, and momentum transfer. Vegetation was assumed to have heat storage. Soil moisture transport in all three layers was determined from diffusion processes, while only the bottom soil temperature was defined by the force-restore relationship (Deardorff, 1977) with the ground cover temperature. Snow effects were reflected in the ground albedo, roughness length, heat capacity of vegetation and topsoil, evaporation and runoff, though snow temperature was regarded equivalent with the ground temperature. The SiB required incident radiation to be partitioned into the direct and diffusive components of visible and near-infrared, and the thermal infrared diffuse radiation. Later, the original SiB was revised to have one vegetation layer with predefined 9 biomes, snowmelt processes, and a submodel of vegetation photosynthesis (Sellers et al. 1996).

The SiB and BATS models have been the two principal models from which the subsequent land surface model have heavily adopted the design philosophy (e.g. Noilhan and Planton, 1989; Dai et al., 2003). The modern land surface models have focused more on the detailed representation of land surface processes (e.g., Noilhan and Mahfouf, 1996; Kucharik et al., 2000; Chen and Dudhia, 2001; Koster et al., 2000; Essery et al., 2003; Van den Hurk et al., 2000; Krinner et al., 2005; Coudert and Ottlé, 2007; Graham and Butts, 2005; Gusev et al., 2006). The model that I developed, SLM, has also been constructed mostly following the earlier versions of SiB and BATS for simplicity, but some parameterizations and land properties have been adopted from more recent land models. The detail of SLM formulation and its sources are discussed in the following section.

2.3 Formulation of SLM

A simple schematic diagram for SLM is given by Fig. 2.1, which introduces what the model is designed to do. The diagram also presents how the vegetation, topsoil and the reference level are coupled via aerodynamic resistances and interact with the canopy air space. Much of the

foundation of SLM stems from previously developed land schemes, but some are modified in its adaptation to keep it simple.

2.3.1 External forcing dataset

SLM requires a set of 14 parameters that define the vegetation and soil properties, in comparison to 20 and 70 approximately for the earliest version of BATS and SiB, respectively. Vegetation is described by the optical and morphological properties, such as vegetation height z_c, displacement height z_{disp}, roughness length z_0, leaf area index (LAI), leaf angle distribution factor χ_L, albedo α_v, parameters related with root structure (L_{root}, L_a, and L_b) and the parameters for the stomatal resistance (r_{cmin}, R_{gl}, and f_{F2}). Two textural parameters that are the percentage of sand and clay define the type of soil. The SLM prognostic variables evolve in response to temperature, specific humidity, horizontal velocity, net downwelling radiation and precipitation at a reference level above canopy. These external parameters can be specified from observations or supplied by the coupled CRM.

2.3.2 Prognostic variables

The SLM solves the prognostic equations for: 1) vegetation temperature T_v, 2) vegetation moisture storage M_v, 3) soil temperature T_{si} and 4) volumetric soil moisture content θ_i, where subscript i indicates the soil layer, with index 1 being the soil top and N being the bottom. These equations are defined as

$$c_{pvege}\frac{dT_v}{dt} = R_{nv} - H_v - E_v \tag{1}$$

$$\frac{\partial M_v}{\partial t} = P_v - D_v - \frac{E_{wv}}{L_v \rho_a} \tag{2}$$

$$c_{si}\frac{dT_{si}}{dt} = -\frac{\partial G_i}{\partial z} = -\left(-\lambda_{hi}\frac{\partial T_{si}}{\partial z}\right) \quad \text{for } 1 \le i \le N \tag{3}$$

$$\theta_s d_1 \frac{\partial \theta_1}{\partial t} = P_I - Q_1 - \frac{E_s}{L_v \rho_a} - F_{root1} \frac{E_{tr}}{L_v \rho_a}$$
$$\theta_s d_i \frac{\partial \theta_i}{\partial t} = Q_{i-1} - Q_i - F_{rooti} \frac{E_{tr}}{L_v \rho_a} \quad \text{for } 2 \le i \le N \tag{4}$$

2.3.3 Radiative transfer

The net radiation of the canopy (R_{nv}) and by topsoil (R_{ns}) are the sums of the absorbed fractions of the incoming solar radiation and incoming longwave radiation, reduced by the emission of infrared radiation. There are various ways to represent the radiative transfer over vegetated land surfaces. In SLM, the canopy layer is treated as a porous medium with a reflectance. The fraction of downwelling shortwave radiation flux $S_{\downarrow}$ that is absorbed by vegetation is given by

$$S_{nv} = S_{\downarrow}\left[1 - \alpha_v + \left(\alpha_s - 1\right) e^{-k_a LAI}\right] \tag{5}$$

where the vegetation albedo α_v is a function of vegetation type, and α_s is the soil surface albedo. The bottom surface of the canopy layer is assumed to be black for the reflected solar radiation by the soil surface. Following Ross (1975) and Goudriaan (1977), the extinction coefficient per unit leaf area k_a depends on the leaf distribution angle χ_L and solar zenith angle θ_z as

$$k_a = \frac{G(\mu)}{\mu} = \frac{\phi_1 + \phi_2 \mu}{\mu} \tag{6}$$

where

$$\phi_1 = 0.5 - 0.633\chi_L - 0.33\chi_L^2$$
$$\phi_2 = 0.877\left(1 - 2\phi_1\right) \tag{7}$$

and $G(\mu)$ is the mean projected area of the solar radiation over canopy in the direction of sun's inclination and $\mu = \cos\theta_z$. The parameter χ_L represents the deviation between actual and the spherical leaf angle distribution, while the extinction coefficient k_a is known to work best in the range of $-0.4 < \chi_L < 0.6$ (Goudriaan, 1977).

Note that equation (5) should be used with caution as it represents a simplification that is only applicable to the case of non-sparse vegetation (LAI > 1). The reflecting and penetrating fractions of the incident solar radiation are treated independently from each other, simplifying the radiative processes that are intercepted by the canopy layer in SLM. As will be shown further, this

approximation seems to work well over the typical vegetated land where the LAI is higher than 1. However, applying (5) to sparse vegetation (small LAI) can lead to significant errors, even negative absorption. In Fig.2.2, the net solar radiation of the canopy is plotted as a function of LAI assuming that the topsoil is 50% saturated ($\alpha_s = 0.14$), the sun is overhead and downwelling radiation is 1000 W/m^2. One can see that the net solar radiation of the canopy may become negative for very small values of LAI. However, as shown by Table 2.1, the actual LAI in those two cases are 2 and 5.5, respectively. The radiative transfer in the case of sparse vegetation becomes rather complicated and requires consideration of the fractional vegetation coverage. In the spirit of simplicity of SLM, the fractional coverage of vegetation within a given grid point has not been included in the current stage of SLM development, but it may be addressed in the future.

The fraction of the incident solar radiation $S_{\downarrow}$ that is absorbed by the soil is determined by the topsoil albedo α_s and the optical properties of the overlying canopy. The net solar radiation of the topsoil S_{ns} is given by

$$S_{ns} = (1-\alpha_s) S_{\downarrow} e^{-k_a LAI} \tag{8}$$

where $S_{\downarrow} e^{-k_a LAI}$ represents the amount of incident solar radiation that penetrates through the canopy on to the topsoil. From Idso et al. (1975), soil surface albedo is expressed in terms of surface topsoil wetness $W_{s1}(=\theta_1/\theta_s)$, and is given by

$$\alpha_s = \begin{cases} \alpha_{s1} - \alpha_{s2} W_{s1} & W_{s1} \le 0.5 \\ \alpha_{s3} & W_{s1} > 0.5 \end{cases} \tag{9}$$

where α_{s1}, α_{s2}, and α_{s3} are given as 0.31, 0.34 and 0.14, respectively. It needs to be cautioned that the soil albedo parameters in (9) were empirically obtained for Avondale loam soil and may not be universally applicable to all soil types. The net solar radiation of the land surface is balanced by the downwelling solar radiation that is reduced by the reflection at the surface of canopy (baresoil) in the case of vegetated (non-vegetated) land.

The downwelling longwave radiation $L_{\downarrow}$ can also be partly absorbed by the canopy layer and transmitted through to the underlying soil surface. The net longwave radiation flux for the vegetation canopy L_{nv} is given by

$$L_{nv} = \varepsilon_v \delta_{tv} L_{\downarrow} + \varepsilon_v \delta_{tv} \sigma T_{s1}^4 - 2\varepsilon_v \delta_{tv} \sigma T_v^4 \tag{10}$$

where ε_v represents the vegetation emissivity for infrared radiation. δ_{tv} is the measure of canopy closure defined as $1-e^{-LAI}$ where the exponential term is interpreted as the fraction of sky the under-canopy ground sees. Thus, $\varepsilon_v\delta_{tv}$ represents the fraction of longwave radiation absorbed or emitted by the vegetation. The net longwave radiation absorbed by the soil surface L_{ns} under the vegetation layer can be similarly written as

$$L_{ns} = \left(1-\varepsilon_v\delta_{tv}\right)L_{\downarrow} + \varepsilon_v\delta_{tv}\sigma T_v^4 - \sigma T_{s1}^4 \tag{11}$$

where the longwave radiation emissivity for soil surface is taken to be unity. Equations (5-11) can be applied to the non-vegetated surfaces to compute the net radiation at surface by setting $LAI = 0$, $\varepsilon_v = 0$ and $\alpha_v = 0$.

2.3.4 Precipitation

The fraction of the precipitation rate at the top of the canopy P that falls through to the underlying soil is modeled following Sellers et al. (1986):

$$P_f = P\exp\left(-k_a LAI\right) \tag{12}$$

The extinction coefficient k_a is assumed to be the same as for the shortwave radiation (6), but with zero zenith angle:

$$k_a = \frac{G(1)}{1} = \phi_1 + \phi_2 \tag{13}$$

The rate of precipitation intercepted by the canopy P_v becomes

$$P_v = P - P_f = P\left[1-\exp\left(-k_a LAI\right)\right] \tag{14}$$

When the leaf water storage M_v exceeds its maximum, S_v, all the excess is drained from the canopy with the rate given by

$$D_v = \begin{cases} 0 & M_v < S_v \\ P_v + \dfrac{\left(M_v - S_v\right)}{\Delta t} & M_v \geq S_v \end{cases} \tag{15}$$

Thus, the total precipitation at the soil surface P_0 is given simply by

$$P_0 = P - P_v + D_v \tag{16}$$

The governing equations of the precipitation in the vegetation layer generally follow Sellers et al. (1986) with the following exceptions. SLM does not have an additional canopy layer near soil surface, called ground vegetation cover. Moisture transfer processes such as precipitation interception and dripping are considered only on the single canopy layer. For the case where the vegetation moisture storage exceeds its capacity, precipitation interception is not allowed. The water dripping rate (second term in the vegetation drainage rate equation (15)) is also included in case when the dew flux adds moisture on leaves exceeding its capacity. For non-vegetated surfaces, the precipitation rate at the reference level P becomes the rate of precipitation incident on the soil surface P_0.

2.3.5 Surface sensible and latent heat fluxes

Using the analogy of the electric current flowing through a conductor with some resistance as the response to the difference in electric potential, the bulk fluxes can also be defined in the similar way (See Figure 2.1). For vegetated surfaces, total heat exchange between the land and reference level is the sum of the under-canopy flux H_s and the canopy flux H_v defined as

$$H_a = \rho_a c_p \frac{(T_a - T_r)}{r_a} = H_v + H_s \tag{17}$$

$$H_v = \rho_a c_p \frac{(T_v - T_a)}{r_b} \tag{18}$$

$$H_s = \rho_a c_p \frac{(T_{s1} - T_a)}{r_d} \tag{19}$$

The total latent heat flux, which is transferred from the canopy air space to the reference level, is the sum of evaporation from topsoil and vegetation:

$$E_a = L_v \rho_a \frac{(q_a - q_r)}{r_a} = E_{tr} + E_{wv} + E_s \tag{20}$$

$$E_{tr} = L_v \rho_a (1 - W_v) \frac{(q_*(T_v) - q_a)}{(2r_b + r_c)} \tag{21}$$

$$E_{wv} = L_v \rho_a W_v \frac{(q_*(T_v) - q_a)}{2r_b} \tag{22}$$

$$E_s = L_v \rho_a \frac{\beta\left(f_h q_*\left(T_{s1}\right) - q_a\right)}{r_d} \tag{23}$$

Direct evaporation from the water storage over leaf surface is proportional to the 'wetness' of the vegetation W_v, which is the fraction of vegetation area covered by water from the intercepted precipitation or from the dew formation. Following Sellers et al. (1986),

$$W_v = \begin{cases} \min\left(1, \dfrac{M_v}{S_v}\right) & q_*\left(T_v\right) \geq q_a \\ 1 & \text{otherwise} \end{cases} \tag{24}$$

where S_v is the maximum water storage on foliage assuming a 0.1 mm water layer thickness, and M_v represents the water storage on foliage and is determined prognostically considering the water balance on canopy as in (2). The additional resistance r_c is introduced to account for the canopy transpiration. The specific humidity of air enclosed in the soil pore space at the soil top is approximated as $f_h q_*(T_{s1})$, where f_h is the measure of the relative humidity of the soil exposed to the overlying air, following Philip (1957):

$$f_h = \begin{cases} \exp\left(\dfrac{\psi_1 g}{R_v T_{s1}}\right) & q_*\left(T_{s1}\right) \geq q_a \\ 1 & \text{otherwise} \end{cases} \tag{25}$$

where ψ_1 is the soil moisture potential in the topsoil layer. The molecular diffusion factor β determines total water flux from topsoil as the fraction of potential evaporation rate considering the moisture availability (Lee and Pielke, 1992):

$$\beta = \begin{cases} \dfrac{1}{4}\left[1 - \cos\left(\dfrac{\theta_1}{\theta_{fc}}\right)\pi\right]^2 & \theta_1 < \theta_{fc} \\ 1 & \theta_1 \geq \theta_{fc} \text{ or } f_h q_*\left(T_{s1}\right) < q_a \end{cases} \tag{26}$$

where the soil volumetric moisture content at field capacity θ_{fc} is defined as the water content corresponding to 0.1 mm/d of soil hydraulic conductivity K (Lee and Pielke, 1992). The dew flux is assumed to be at the potential rate with $\beta = 1$ and $f_h = 1$. Under-canopy latent heat flux, E_s follows the formulation introduced by Sakaguchi and Zeng (2009), which applied the under-canopy stability to determine the efficiencies in the under-canopy turbulent transfer (see Section 2.2.6).

For non-vegetated surfaces, the total heat fluxes traversed between topsoil and the reference level and are given by

$$H_a = H_s = \rho_a c_p \frac{(T_{s1} - T_r)}{r_a} \tag{27}$$

$$E_a = E_s = L_v \rho_a \frac{\beta\left(f_h q_*(T_{s1}) - q_r\right)}{r_a} \tag{28}$$

Assuming no heat or moisture storage in the canopy air space, fluxes from soil and vegetation combine to give the total surface fluxes. Then, the canopy airspace temperature T_a and specific humidity q_a can be determined diagnostically at each time step by solving (17) and (20).

2.3.6 Surface momentum fluxes

Turbulent momentum fluxes between land surface and atmosphere are defined as

$$\begin{aligned} \frac{\tau_x}{\rho_a} &= C_D V_r u_r \\ \frac{\tau_y}{\rho_a} &= C_D V_r v_r \end{aligned} \tag{29}$$

where τ_x and τ_y are surface stress in x- and y-direction, u_r and v_r are the zonal and meridional wind at the reference level, and V_r is the reference level wind speed. Following Monin-Obukhov similarity theory, a drag coefficient for momentum transport C_D is defined as

$$C_D = \left[\frac{u_*}{u(z)}\right]^2 = k^2 \left[\ln \frac{(z - z_{disp})}{z_0} - \Phi_M\left(\frac{z - z_{disp}}{L}\right)\right]^{-2} \tag{30}$$

where Φ_M is the stability function for momentum, z_o is the surface roughness length for wind and k is a von Karman constant with a value of 0.4. z_{disp} is a displacement height of the surface that is defined as a fraction of vegetation height (e.g., $0.67z_c$ for a tall tree, $0.68z_c$ for vegetation shorter than 0.5m (Oleson et al., 2010), or 0 for non-vegetated surfaces). L is the Monin-Obukhov length that accounts for the atmospheric stability in terms of buoyancy. The drag coefficient is computed in each grid pixel.

2.3.7 Aerodynamic resistance

Aerodynamic resistance of heat and water vapor exchange between the surface and the reference level can be defined as

$$r_a = \frac{1}{C_H V_r} \tag{31}$$

The surface is taken to be the canopy air space (topsoil) for vegetated (non-vegetated) land. The turbulent transfer coefficient for heat and moisture C_H in surface layer is governed by Monin-Obukhov similarity theory, and is computed in each grid pixel following

$$\begin{aligned} C_H &= \frac{u_* T_*}{u(z)\left[T_p(z) - T_p(z_{0h})\right]} \\ &= \frac{k^2}{\left[\ln\frac{\left(z - z_{disp}\right)}{z_0} - \Phi_M\left(\frac{z - z_{disp}}{L}\right)\right]\left[\ln\frac{\left(z - z_{disp}\right)}{z_{0h}} - \Phi_H\left(\frac{z - z_{disp}}{L}\right)\right]} \end{aligned} \tag{32}$$

where Φ_H is the stability function for heat and z_{h0} is the roughness length for heat. We define the temperature at z_{0h} ($T_p(z_{0h})$) to be the same as the canopy air space temperature for vegetated surfaces, and topsoil temperature for non-vegetated surfaces. We assume that same C_H can be applied to the water vapor transfer. The z_{0h} is defined following Yang et al. (2008):

$$z_{oh} = \left(\frac{R_{ec}\nu}{u_*}\right)\exp\left(-7.2 u_*^{0.5} \left|T_*\right|^{0.25}\right) \tag{33}$$

where R_{ec} is critical Reynold's number and set to be 70, viscosity ν is 1.5×10^{-5} m^2s^{-1}, while the temperature scale T_* is defined as

$$T_* u_* = -\frac{H_a}{\rho_a c_p} \tag{34}$$

Bulk aerodynamic resistance at leaf boundary layer r_b is given similar to that of Dickinson et al. (1993):

$$r_b = \frac{1}{LAI C_v}\left(\frac{u_*}{d_{leaf}}\right)^{-0.5} \tag{35}$$

where C_v=0.01 $ms^{-0.5}$ and d_{leaf}= 0.04 m. Leaf boundary layer resistance is doubled for the moisture transfer as the transpiration is assumed to happen on one side of the leaf.

Under-canopy aerodynamic resistance r_d is adopted from Sakaguchi and Zeng (2009). The basic form of aerodynamic resistance is

$$r_d = \frac{1}{C_{uv} u_*} \tag{36}$$

where C_{uv} represents the unitless turbulent transfer coefficient between soil surface and canopy air space and it is a weighed sum between the turbulent coefficient when soil is covered by thick canopy allowing very litter turbulence and the one under the sparse canopy (Zeng et al., 2005; Oleson et al., 2010):

$$C_{uv} = C_{bare}\left(1-\delta_{tv}\right) + C_{dense}\delta_{tv} \tag{37}$$

where $\left(1-\delta_{tv}\right)$ is the fractional area of under-canopy that is not directly shaded by the canopy overhead. C_{bare} is obtained based on Monin-Obukhov similarity theory for surface sub-layer following

$$C_{bare} = \frac{k}{aR_e^{0.45}} \tag{38}$$

where R_e ($=u_* z_0/\nu$) is Reynolds number with surface roughness length z_0, k is von Karman's constant (=0.4), and a is a constant with a value of 0.13 (Zeng and Dickinson, 1998). Dickinson et al. (1993) suggested 0.004 for the turbulent transfer coefficient under dense canopy C_{dense}, and Sakaguchi and Zeng (2009) modified it to account for the under-canopy stability as

$$C_{dense} = \begin{cases} 0.004 & \text{unstable} \\ \dfrac{0.004}{1+\gamma \min\left(\eta, \eta_{\min}\right)} & \text{stable} \end{cases} \tag{39}$$

where γ is set to 0.5 and η is the stability parameter defined as

$$\eta = \frac{g z_c \left(T_a - T_{s1}\right)}{T_{s1} u_*^2} \tag{40}$$

where T_a is a canopy air space temperature, T_{s1} is a soil top temperature, and z_c is the canopy height. Thus, for stable under canopy space, the turbulent transfer coefficient is reduced and hence suppresses the turbulent exchange of heat, moisture and momentum. $\eta_{\min}$ is an adjustable parameter that determines the lower threshold of η and its value is set to 10 given from Sakaguchi and Zeng (2009).

2.3.8 Stomatal resistance

Stomatal resistance r_c represents the resistance imposed between the pores on foliage and the surrounding air space for the water vapor transfer. The Jarvis (1976) parameterization is selected in SLM and it is based on the idea that control factors for transpiration include air temperature, water vapor pressure deficit, solar radiation and soil moisture (Jacquemin and Noilhan, 1990):

$$r_c = \frac{r_{c\min}}{LAI\, F_1 F_2 F_3 F_4} \tag{41}$$

where $r_{c\ min}$ is the minimum stomatal resistance and its values are dependent on the vegetation type, and $F_{1\text{-}4}$ represent the environmental control factors. F_1 is the effect from solar radiation written as

$$F_1 = \frac{\frac{r_{c\min}}{r_{c\max}} + f_{F1}}{1 + f_{F1}} \tag{42}$$

where $r_{c\ max}$ is maximum stomatal resistance taken as 5000 s/m and parameter f_{F1} is defined as

$$f_{F1} = 0.55 \frac{S_{\downarrow}}{R_{gl}} \frac{2}{LAI} \tag{43}$$

In (43), $S_{\downarrow}$ is the incident solar radiation, and vegetation type dependent parameter R_{gl} is the minimum solar radiation required for transpiration. F_2 is a stress factor from vapor pressure deficit at canopy air space level and it is written as

$$F_2 = \frac{1}{1 + f_{F2}\left(q_*(T_a) - q_a\right)} \tag{44}$$

where f_{F2} is vegetation type dependent parameter. The stress factor arises from the vegetation temperature is defined as

$$F_3 = 1 - 0.0016\left(T_{opt} - T_a\right) \tag{45}$$

where T_{opt} is the optimum temperature for transpiration and set to 298K. Soil moisture availability also influences transpiration following

$$F_4 = \sum_i \frac{\left(\theta_i - \theta_{wilt}\right) d_i}{\left(\theta_{fc} - \theta_{wilt}\right) d_{root}} \tag{46}$$

It should be noted that soil moisture stress factor, F_4, is integrated over layers where root exists, and thus, d_{root} represents the total depth of soil column with root.

2.3.9 Soil heat transport

Following Fourier's law for heat conduction in a homogeneous medium, the soil heat flux G_i between adjacent layers i and $i+1$ can be defined as

$$G_i = -\lambda_{hi} \frac{T_{si} - T_{si+1}}{z_{i+1} - z_i} \tag{47}$$

where the soil-layer index i and soil depth z are increasing downward, and z_i is the center depth of the ith soil layer (see Figure 1.1 to avoid confusion). Note that G_i is positive for upward heat transport. The soil thermal conductivity at the interface λ_{hi} is computed as the layer-thickness weighted thermal conductivity of two adjacent layers. The implicit method was implemented to compute the soil temperature (3) to maintain the stability and positiveness of the diffusion equation in a finite-differential form; the detailed description can be found in Appendix A.

The Johansen (1977) method relates the soil thermal conductivity to the soil soil volumetric content at saturation, quartz content and dry density. The method calculates soil thermal conductivity λ_i of soil layer i by weighing dry soil and saturated soil thermal conductivity following

$$\lambda_i = KR_i \lambda_{sat} + (1 - KR_i) \lambda_{dry} \tag{48}$$

where the weighing factor KR_i is known as Kersten number. It is a function of soil wetness and is written as

$$KR_i = \log \frac{\theta_i}{\theta_s} + 1 \quad \text{for } \theta_i \geq 0.1\theta_s \tag{49}$$

For very dry soil with wetness (W_{si}) less than 0.1, the Kersten number becomes zero and total soil thermal conductivity is approximated to the dry soil thermal conductivity λ_{dry}. For natural dry soil, thermal conductivity is assumed to be related to its volumetric moisture content at saturation and is given as

$$\lambda_{dry} = \frac{0.135\gamma_d + 64.7}{2700 - 0.947\gamma_d} \tag{50}$$

$$\gamma_d = (1-\theta_s)2700 \tag{51}$$

where γ_d is a dry soil density that is defined empirically using the FIFE site observation data, θ_s is a soil volumetric moisture content at saturation, and the unit weight of soil solids are set to 2700 kg m^{-3}. For saturated soil, the thermal conductivity depends on the soil volumetric moisture content at saturation and is given by

$$\lambda_{sat} = \lambda_s^{1-\theta_s}\lambda_w^{\theta_s} \tag{52}$$

where $\lambda_w = 0.57$ Wm^{-1}K^{-1} is the thermal conductivity of water. The soil solids thermal conductivity λ_s is parameterized as

$$\lambda_s = \lambda_q^{qrz}\lambda_o^{1-qrz} \tag{53}$$

where *qrz* is quartz content. (53) is defined under the assumption that soil solids are largely divided into quartz and other minerals. The thermal conductivity for quartz λ_q is 7.7 Wm^{-1}K^{-1}, and the thermal conductivity of minerals λ_0 is given by the quartz content following

$$\lambda_o = \begin{cases} 2 & qrz > 0.2 \\ 3 & otherwise \end{cases} \tag{54}$$

Sand has high percentage of quartz and thus high thermal conductivity (Buckman and Brady, 1969). It was assumed that the quartz content is related with sand content of each soil type (Peters-Lidard et al., 1998); therefore, quartz content *qrz* can be approximately replaced by %SAND/100.

Soil volumetric heat capacity of any layer can be defined by the weighed sum of water heat capacity and soil solids heat capacity (de Vries, 1963):

$$c_{si} = (1-\theta_s)c_{solids} + \rho_w\theta_i c_{water} \tag{55}$$

where θ_i is volumetric water content of soil and θ_s is soil volumetric moisture content at saturation. C_{water} (=4.1796×10^6 Jm^{-3}K^{-1}) is the volumetric heat capacity for water and ρ_w is water density of 10^3 kg m^{-3}. In the original work of de Vries (1963), the heat capacity of soil solids c_{solids} is found to be related with the contents of sand and clay for various soil type and the relationship is given by

$$c_{soilds} = \frac{(2.128\%SAND + 2.385\%CLAY)}{\%SAND + \%CLAY} \tag{56}$$

Combination of (3) and (47) gives the heat conduction equation, from which the soil temperature is determined prognostically by considering the difference in the influx and outflux of a given

layer. There is no heat flux at the bottom layer, $G_N = 0$, while the top boundary condition is determined by energy balance

$$G_0 = -1 \times \left(R_{ns} - E_s - H_s \right) \tag{57}$$

2.3.10 Soil hydrology

The rate of change of moisture content in each soil layer is determined prognostically by solving the water balance as in (4). Darcy's law is used to define the water flux due to the vertical moisture gradient:

$$Q = -K \frac{\partial(\psi + z)}{\partial z} = -K \left(\frac{\partial \psi}{\partial z} + 1 \right) \tag{58}$$

where K is a hydraulic conductivity of soil, Ψ is a soil matric potential and z is a gravitational potential having the reference level at the soil surface. In finite-difference form, Eq. (58) becomes

$$Q_i = K_{hi} \left(1 - \frac{\psi_{i+1} - \psi_i}{z_{i+1} - z_i} \right) = K_{hi} \left(1 - \psi_s \theta_s^B \frac{\left(\theta_{i+1}^{-B} - \theta_i^{-B} \right)}{z_{i+1} - z_i} \right) \tag{59}$$

where ψ_i is a function of θ_i (see definition (65)). The hydraulic conductivity at the soil interface K_{hi} is given by the depth-weighed average conductivities of the adjacent layers. Note that Q_i is positive for downward transport. The soil moisture transport equation was coded using the implicit time stepping algorithm that makes the scheme unconditionally stable for any time step (see Appendix A for details).

In bottom soil layer, the drainage can occur when the moisture level exceeds it saturation value θ_s . The drainage rate Q_{dr} (=Q_N) is then given by

$$Q_{dr} = \max \left[0, \frac{d_N}{\Delta t} \left(\theta_N - \theta_S \right) \right] \tag{60}$$

The amount of soil moisture removed by the transpiration in each soil layer is controlled by the root fraction $F_{root\,i}$ of each layer following the formulation by Zeng (2001):

$$F_{root\,i} = Y(i) - Y(i-1) \tag{61}$$

$$Y(i) = 1 - \frac{1}{2} \left(e^{-L_a d_i} + e^{-L_b d_i} \right) \tag{62}$$

where Y is the cumulative root fraction, L_a and L_b are vegetation type dependent coefficients, and d_i is the thickness of soil layer i.

When rain falls onto the soil surface, it is not always completely absorbed by the soil. The limiting factor for the rate of precipitation infiltration into the soil is the hydraulic conductivity at saturation K_s (Sellers et al., 1986):

$$P_I = \begin{cases} \min(P_0, \rho_w K_s) & W_{s1} < 1 \text{ and } T_{s1} > 0°C \\ 0 & \text{otherwise} \end{cases} \tag{63}$$

Rain infiltration is allowed only when the top layer is sub-saturated and not frozen. The precipitation that cannot be absorbed by the soil simply becomes the surface runoff R_{osfc}.

$$R_{osfc} = P_0 - P_I \tag{64}$$

Then, the total runoff rate becomes the sum of the surface runoff R_{osfc} and the drainage Q_{dr}.

2.3.11 Soil hydraulic properties

Soil moisture potential at each soil layer ψ_i is computed from its saturation value ψ_s and the soil layer's wetness W_{si} is based on the empirical relationship derived by Clapp and Hornberger (1978):

$$\psi_i = \psi_s W_{si}^{-B} = \psi_s \left(\frac{\theta_i}{\theta_s} \right)^{-B} \tag{65}$$

where B is an empirical parameter that is expressed as the function of clay contents of soil:

$$B = 0.159\%CLAY + 2.91 \tag{66}$$

Soil hydraulic conductivity K_i is derived from Clapp and Hornberger (1978) method using saturated hydraulic conductivity K_s, saturated volumetric moisture content θ_s, and volumetric soil moisture content at i layer θ_i following

$$K_i = K_s \left(\frac{\theta_i}{\theta_s} \right)^{2B+3} \tag{67}$$

Cosby et al. (1984) found that there is a high correlation between soil contents, in the percentage of clay and/or sand, and the soil hydraulic and thermal properties. The relationships are given as

$$K_s = 7.0555 \times 10^{-6} \times 10^{0.0153\%SAND - 0.884} \quad (68)$$

$$\theta_s = 0.489 - 0.00126\%SAND \quad (69)$$

$$\psi_s = -0.01 \times 10^{1.88 - 0.0131\%SAND} \quad (70)$$

2.4 Evaluation of SLM

2.4.1 Test sites and forcing dataset

The performance of the SLM has been tested using five observational datasets from: 1) the ARM SGP site (ARM SGP; grasslands) in Oklahoma, 2) Bondville in Illinois (U.S.-Bo1; corn or cropland), 3) Morgan Monroe State Park in Indiana (U.S.-MMS; deciduous broadleaf forest), 4) Audubon research ranch in Arizona (U.S.-Aud; grasslands), and 5) Duke Forest Open Field in West Virginia (U.S.-Dk1; grasslands). The ecosystem of each test site is defined following the International Geosphere-Biosphere Programme (IGBP) land classification. The forcing data periods of all sites include both fair and rainy days.

Unless LAI for the site is estimated from the direct measurement at the tower site (i.e., U.S.-Dk1), it is assigned by averaging the 8-day composite 1-km resolution MOD15A2 product from Moderate Resolution Imaging Spectroradiometer (MODIS) satellite data. The surface albedo over each vegetated land is assumed to be 0.16/0.17 for the grasslands and 0.15 for the forest, which is within the range given in Garratt (1994). Surface roughness length z_o over vegetated land is defined to be dependent upon the canopy height following Oleson et al. (2010); the ratio between them is 0.12 for grassland and 0.055 for tall trees. Similarly, the displacement height z_{disp} can be derived from the canopy height; the ratio is 0.68 for all vegetated surfaces included in this study. Soil clay and sand percentage information is given from: 1) the analysis of Curtis et al. (2002) for U.S.-MMS site, 2) the measurements at 30cm depth for U.S.-Dk1 site, and 3) the estimation guided by the U.S. Department of Agriculture (USDA) soil triangle dataset (1951) for the given soil type following Cosby et al. (1984). The stomatal resistance parameters generally follow the values listed for the various types of vegetation in Kumar et al. (2011) except that the suggested value for minimum stomatal resistance $r_{c\min}$ for grasslands of 40 s/m was increased to 250 s/m for ARM SGP case, and doubled to 200 s/m for the US-MMS site. Otherwise, the simulated latent heat flux

for those sites would be rather significantly overestimated. The vegetation root parameters generally follow Zeng (2001) for the given IGBP vegetation type. The soil column of each test site is assigned with either 8 or 9 layers, which is defined to best match the observation depths. The thickness of the topsoil layer is in the range from 1 to 2 cm, and it increases with depth. In addition, the atmospheric signals sent to the land surface is supplied from the tower measurement by taking the tower height as a reference height: this forcing data set includes temperature, specific humidity, precipitation, downwelling solar and infrared radiation at the reference height. The input parameters for vegetation and soil properties as well as the site details are listed in Table 2.1.

2.4.2 Estimation of surface energy fluxes

Figure 2.3 compares the observed and modeled net radiation R_{net}, upwelling solar *SWup*, and longwave *LWup* fluxes over all test sites except for U.S.-Bo1 where no measurements of the upwelling radiative fluxes were available for the comparison. One can see that *SWup* agrees rather well with measurements, and the root-mean-square-error (RMSE) of albedo lies close to 0.01 when the observed albedo is interpreted as the ratio of upwelling to downwelling solar radiation. The modeled *LWup*, however, shows some overestimation during the day and underestimation during the night, especially over the US-MMS site (forest), which is due to errors in the vegetation temperature.

Figure 2.4 compares the surface fluxes, and the corresponding RMSE and correlation coefficient (R) are summarized in Table 2.2. Evolution of simulated surface energy fluxes compares generally well to the observations: correlation coefficients are mostly larger than 0.9. However, as shown in Figure 2.5, there are some persistent biases with an underestimation of the surface sensible heat flux and an overestimation of the surface latent heat flux at daytime. Linear fits between the observed and simulated sensible heat flux have regression slopes in the range of 0.61-0.89 for all sites confirming the largest deviation is the underestimation during daytime. The slope of the fitted lines in the latent heat flux comparisons indicates a value above 1 except for U.S.-MMS and U.S.-Dk1, where a few outliers in the observation skewed the result. Warmer surface temperature during daytime as can be deduced from higher outgoing longwave radiation (see Fig. 2.3) that seem to accelerate the evaporation rate via increased vapor pressure deficit in the canopy air space, rather than to increase the sensible heat flux for a given net radiation.

2.4.3 Prediction of soil temperature and moisture

Figure 2.6 compares the evolution of soil temperature and moisture profiles for the grassland (ARM SGP). The model seems to reproduce quite well the phase and amplitude of diurnal variation as well as the multi-day trend of soil temperature with the exception of 5-cm deep layer where the diurnal variation of temperature seems to be overestimated by about 2 °C. Soil moisture comparison shows rather considerable biases with respect to observations, especially after the rain events. The modeled period includes several rain events and the peaks are observed on day 175, 177, 179, 180 and 185, and the moisture of the upper soil levels shows strong 'jumps' following these events; however, the jumps are not nearly as prominent in the observations. Even though there is a clear sign of gradual penetration of rainwater down to about 60 cm depth over the period of one day, the rainwater does not seem to percolate fast enough into the deeper layers. The result is the oversaturation of moisture in the upper soil layers. Before the first rain event the model seems to reproduce the gradual drying of the soil layers quite well, although moisture in the upper 2 layers (5 and 15cm) tend to have larger diurnal amplitudes.

The U.S.-Aud site also offers the soil temperature observations at various depths ranging from 2cm to 128 cm deep. As shown in Figure 2.7, the temperature of the upper layer overestimates the diurnal variability, as soil near the surface warms and cools quickly in a day. As common in other cases, this discrepancy reduces with in deeper layers: 2cm deep layer has RMSE of 3 °C but 128cm deep layer has a correlation coefficient of 1. The U.S.-Aud site has the most frequent precipitation occurrence during the entire data period (20 days), and it explains the random outliers in the observed evolution of surface fluxes, which may correspond to the instrument errors under frequent and heavy rainfall.

Figure 2.8 shows the evolution of soil temperature and moisture profiles over the cornfield (US-Bo1). Note that the vertical resolution for temperature measurements is much higher than for the soil moisture observation at this site. Temperature observations were available at 2, 4, 8, 16, 32, 64 and 128 cm depth from the surface (not all of those are shown in Fig. 2.8(a)), while the soil moisture was measured only at 5, 10, 20, and 50cm depths. Similar to ARM-SGP case, the model overestimates the soil temperature with RMSE of about 2.3 °C in the upper 8 cm, but RMSE decreases with depth and becomes 0.12 °C at the depth of 128 cm. The model seems to reproduce

quite well the reduction of the diurnal temperature amplitude after the day 208 rain event, and the subsequent recovery during the following days. The simulated soil moisture in the upper 30 cm tends to quickly homogenize and reduce vertical difference of moisture content between adjacent layers that conflicts with the observations, where the soil saturation level at different depth retains the vertical gradient for 8 days until the first rain. Unlike ARM-SGP, the upper soil layer observations in US-Bo1 show considerable jumps in soil moisture level after the rain event, which is even higher than in the simulation. Such a different behavior over different sites can be explained by different soil texture. The sand content for US-Bo1 and ARM-SGP sites are quite similar, 17% and 10%, respectively; however, the ARM-SGP soil contains about three times as much clay (see Table 2.1). Although no direct observation is available, the hydraulic conductivity, evaluated using the method described in section 2.2, becomes about five times as large in the ARM-SGP case as in the US-Bo1 case, which may explain rather slow penetration of rain water in US-Bo1 soil compared to ARM-SGP soil.

2.5 Uncertainties of the empirical parameters used in land models

2.5.1 Bias in the evapotranspiration

The SLM tends to overestimate the evaporation and underestimate the sensible heat flux even when SLM computes the net absorbed radiation accurately (Figure 2.4). This partitioning bias could be attributable to the uncertainty related to the empirical parameters that define stomatal resistance. In fact, many studies (e.g., Alapaty et al., 1997; Cooter and Schwede, 2000; Alfieri et al., 2008) have blamed the uncertainty in parameterization of r_{cmin} for the large bias in the transpiration over vegetated land. Jacquemin and Noilhan (1990) showed that its derivation was based on a certain type of environment that is limited to: 1) well-irrigated soil, 2) optimum level of air temperature and saturation for transpiration, and 3) maximum solar input. Others (e.g., Schulze et al., 1994; Niyogi and Raman, 1997; Ronda et al., 2001) have found too large a sensitivity to solar input and plant types to transpire soil moisture to the surrounding air space. Overall, the modeling of hydrological cycle over land remains a big challenge due to the aforementioned uncertainties in $r_{c\min}$ together with the overly reduced and simplified

environmental stress factors for computing r_c (Niyogi and Raman, 1997; Cooter and Schwede, 2000; Alfieri et al., 2008).

Although the simulated net radiation by SLM compares well to the observation, the outgoing longwave radiation is commonly overestimated during daytime, for which a positive bias in vegetation temperature can be responsible (Fig. 2.3). Therefore, the overestimation of evapotranspiration during daytime can result from the higher vegetation temperature. The daytime overestimation in the soil temperature near surface may be another contributing factor to this bias as the variation in the topsoil temperature is closely connected with the change of vegetation temperature (not shown), and hence, indirectly influences the evapotranspiration.

In SLM, each grid cell is either completely covered with a single type of vegetation or baresoil (non-vegetated); thus, SLM can depict inhomogeneous land surface characteristics pixel-by-pixel within a domain. However, in the real world, it is hard to find an area that has land-type uniformity for 100m across or so, which is comparable to the size of LES grid cell. As most of radiation absorption and surface fluxes occur in the canopy level, higher evaporation rate is expected over the vegetated land. Therefore, sub-grid scale heterogeneity may actually decrease the net evapotranspiration rate as the high evaporation rate over the patch of vegetated land is partly offset by the reduced evaporation over the patch of baresoil. The artificial increase of $r_{c\min}$ in the test cases is assumed to incorporate this effect and, without this modification, the prediction of evaporation becomes less accurate. In the future, evaporation bias will be addressed again by improving the scheme to account for the subgrid-scale vegetation fractional cover.

2.5.2 Bias in the estimation of soil temperature and moisture

As shown in Figure 2.6 through Figure 2.8, the soil temperature profile shows the similar pattern of bias of overestimating soil temperature during day and underestimating it during night, with the locality of the bias occurring in the upper soil layers. In SLM, the reflection of the shortwave radiation by the canopy layer occurs independently from the radiation which penetrates the canopy as in Eq. (5). Due to this assumption, the penetration of solar radiation through the vegetation may be overestimated, as a result, more solar radiation reaches to the topsoil. Also, the daytime positive bias in the soil temperature may exert similar effect on the vegetation layer by emitting more thermal infrared radiation, which can lead to the overestimation of the

evapotranspiration. However, the potential impact of this bias in Equations (5) and (8) to the surface temperature and heat fluxes can be significant only in the case of sparse vegetation with LAI being much smaller than 1. As shown in Table 2.3, all our cases have LAI in the range of 1 to 5.5, so the large fraction of solar radiation tends to be intercepted at the vegetation layer leaving only small fraction to the soil absorption. As aforementioned, the case of sparse vegetation is much more complicated as it requires fractional vegetation cover, which is not included in the current version of SLM. However, a more accurate representation of surface radiative transfer equation may be considered in the future extensions of SLM.

One can also notice that the upper and deeper levels seem to be unable to communicate; therefore, the redistribution of added heat into the deeper layers during day and the warming of the surface from below at night are retarded, and these processes become less effective. The inaccuracy in the prediction of soil temperature and moisture profiles could be contributable to the highly empirical parameterization of soil thermal and hydraulic properties. In nature, soil profiles are rarely uniform, and the heat and moisture transport can occur in any direction. However, these factors are simplified in the adaptation of SLM: first, the soil is assumed to a have uniform type in a domain, and second, the dissipation of heat and moisture in soil is allowed only in vertical direction. Also, root distribution parameters and vegetation type dependent root length are assigned from the global coarse resolution dataset and may not represent the vegetation at the test sites accurately enough.

It has long been recognized that, in general, the land models have difficulty reproducing the soil hydrology (Zhang et al., 1996). For example, Sahoo et al. (2008) obtained the soil moisture estimates from the three different land schemes (the Hydrological improvement to the Simplified version of the Simple Biosphere Model (HySSiB; Mocko and Sud, 2001), Noah model (Chen and Dudhia, 2001) and Community Land Model (CLM; Oleson et al., 2010)), and compared them with observation in diurnal or hourly time scales. HySSiB and Noah show the overestimation of upper level soil moisture throughout the year. Evolution of soil moisture in CLM shows a strong fluctuation with the passage of rain. The SLM uses a similar parameterization of the soil thermal and hydraulic properties as the CLM, and shows a similar bias in the upper layers. Discrepancy in the upper level soil moisture is accentuated with fast wetting after the onset of rain and quick drying after the end of rain. Such bias is only observed near the soil surface; therefore, it is hypothesized that the penetration of rain into the deeper layers is not correctly parameterized in

SLM. Extensive observational and theoretical studies about water flow into unsaturated porous media (Lu et al., 1994; DiCarlo, 2004; Cueto-Felgueroso and Juanes, 2008, 2009) generally concluded that even with constant and uniform water flux into a homogeneous soil layer, the leading edge of downward water flow develops a finger-shaped pattern due to the multiphase infiltration flow. However, the overly simplified treatment of rain infiltration in SLM tends to produce too slow a flux; therefore, the redistribution of added moisture into soil is less efficient.

2.6 Summary

A main accomplishment of this dissertation has been to develop a simplified interactive land surface model, a Simple Land Model (SLM) coupled to SAM CRM, to study land-atmosphere interactions and physical processes over vegetated land. In the spirit of simplicity, we define a 2-way coupling between the land and atmosphere through the exchange of heat, momentum and moisture between those two systems. Land surface in SLM is composed of 1 layer of vegetation (if vegetated land is assigned) over multi-layer soils. Each individual land type is characterized by twelve optical and morphological parameters, with the soil type specified by two texture parameters, the percentage of sand and clay. The turbulent transfer of heat, moisture and momentum are computed from the resistance method, in which the aerodynamic and stomatal resistances are modeled depending on the vegetation type and soil state. Radiative transfer in the canopy is calculated using a simple extinction method with the extinction coefficient dependent on the vegetation's leaf area index, leaf angle distribution factor and solar zenith angle, combining direct and diffuse fluxes. Soil heat and moisture transport are calculated from a diffusion method where the transport is allowed only in a vertical direction. The use of SLM is limited to the snow-free and non-frozen soil with no runoff and drainage induced by the topographic slope.

The SLM performance has been tested using point observations over three different types of vegetated land in summertime: grassland (ARM-SGP, U.S.-Aud, and U.S.-Dk1), cropland (US-Bo1), and broadleaf forest (US-MMS). The SLM has been forced over period from 10 to 20 days by observed temperature, humidity, precipitation, and wind at the reference level as well as downwelling shortwave and longwave fluxes. Synoptic conditions at each site included both fair and rainy days. The simulated phase and amplitude of the diurnal cycle of net radiation, latent and sensible heat fluxes generally agree rather well with observations, although there is some tendency

for overestimation of evapotranspiration rates and corresponding underestimation of sensible heat fluxes. The transpiration bias can be caused by the uncertainty in parameters used in the quantifications of the plant's root system efficiency to uptake root zone soil moisture, and the resistances for turbulent heat and moisture exchange in the canopy and under-canopy space. The simplified treatment of the optical properties of vegetation and soil seems to be sufficient to reproduce the observed diurnal variation of net absorbed radiation. Evolution of soil temperature and moisture profiles has been directly compared to observations for the grassland and cropland cases at various depths. Overall, the model has been able to reasonably reproduce the diurnal phase and amplitude variation of temperature with depth as well as its multi-day trend. The most significant bias has been the overestimation of soil temperature range in upper layers; however, the error decreases significantly with the soil depth. One contributing factor to this daytime positive bias near surface may be related to the approximations made in Equations (5) and (8), which treat the transmission and reflection of the solar radiation at the canopy independently from each other. However, the effect of the simplified treatment of the radiative transfer through the canopy is relatively small as very little direct radiation reaches the soil surface for LAI > 1, which is the case in our study.

The Serious biases in reproducing the evolution of the soil moisture right after the precipitation events have been identified, most likely because of the underestimation in the traveling water flow between the upper and lower levels, such as the rate of penetration of rainwater into the deeper soil layers. Future development of the SLM may alleviate this problem.

The motivation for the development of the SLM is to build a simple land model that can supply the atmospheric bottom boundary condition when coupled to SAM. Despite its simplicity, the performance of SLM satisfies its purpose, and it computes energy and hydrological cycles that are comparable to observations over various land surfaces. Unlike other bulky land models that are coupled to GCMs, SLM includes only the processes that are responsible for the development of convection over land (i.e., radiative transfer, turbulent heat moisture and momentum transfers in PBL). SLM is easy to manipulate, and users need information only about the 14 external parameters that characterize the land surface. Over the years, CRM/LES has been used extensively to study the development of convection over land. But, their application is limited to idealized case studies as the surface heat fluxes that drive turbulent and convective processes in the PBL must be prescribed. Development of SLM and its use within SAM can provide a useful tool to gain

fundamental insights into the diurnal development of precipitation over land, especially its linkage to the vegetation type or soil moisture level.

Tables

Site	U.S. Bo1	SGP-ARM	U.S. - MMS	U.S. - Aud	U.S.-DK1
Location	Bondville, IL	Southern Great Plains (SGP)	Morgan Monroe State Park, IN	Audubon, AZ	Duke Forest Open Field, NC
Experiment	AmeriFlux	ARM IOP 1997	AmeriFlux	AmeriFlux	AmeriFlux
Data Period	7/23/07-8/2/07	6/19/97 – 7/9/97	8/8/09-8/18/09	7/28/06 – 8/18/06	6/9/07- 6/29/07
Data frequency (hr)	0.5	3	1	0.5	0.5
Land cover	Cornfield	Grasslands	Deciduous-Broadleaf forest	Grasslands	Grasslands
Reference level (m)	10	10	46	4	6
Temperature range (°C)	14.5-31.8	14.5 – 35.4	16.1 – 30.0	15.4 – 31.6	13.5- 33.5
Specific humidity range (g/kg)	10.0-20.1	9.7 – 19.7	9.8 – 18.5	10.6 - 19.9	7.8 – 15.9
Rainfall maximum (mm/hr)	10.8	3.4	6.6	34	20.6
LAI	4	2	5.5	1	1.7
$z_c\ (m)$	3	0.5	27	0.2	0.2
$z_0\ (m)$	0.36	0.06	1.485	0.024	0.024
$z_{disp}\ (m)$	2.04	0.34	18.36	0.136	0.136
χ_L	-0.3	-0.3	0.25	-0.3	-0.3
α_v	0.16	0.16	2	0.173	0.16
$L_{root}\ (m)$	1.5	1.5	5.99	1.5	1.5
L_a	5.558	10.74	1.955	10.74	10.74
L_b	2.614	2.608	200	2.608	2.608
$r_{cmin}\ (s/m)$	40	250	30	40	40
$R_{gl}(W/m^2)$	100	100	30	100	100
f_{F2}	36.35	39.18	54.53	36.25	36.25
Soil type	Silt loam	Silt clay loam	Clay loam		
%SAND	17	10	34	58	48
%CLAY	13	34	40	27	8.6
Total soil depth (m)	2.71	1.98	2.1	3	2.15

Table 2.1 Information for the test sites and the list of input parameters that define the soil and vegetation types.

Table 2.2 Error statistics of computed surface energy fluxes and soil temperature at various depths for the entire period listed in Table 2.1. Root-mean-squared-error, RMSE, is defined as $\sqrt{\frac{1}{n}\sum_{i=1}^{n}(x_i - y_i)^2}$, where x and y are the simulated and observed data, respectively. Cross-correlation coefficient R (in brackets) is the ratio of the covariance over observation and simulated results to the product of the two standard deviations.

	SGP ARM		U.S.-MMS	U.S.-Bo1		U.S-Aud		U.S.-Dk1
R_n (W/m^2)	13.22 [1]		23.54 [1]	8.66 [1]		46.84 [0.98]		30.5 [0.99]
H_a (W/m^2)	26.90 [0.93]		24.18 [0.9]	17.87 [0.9]		26.51 [0.83]		42.14 [0.81]
E_a (W/m^2)	45.71 [0.96]		68.69 [0.92]	48.75 [0.97]		45.88 [0.92]		71.65 [0.82]
	T_{5cm} (°C)	1.83 [0.92]		T_{2cm}	2.33 [0.96]	T_{2cm}	2.994 [0.85]	
	T_{15cm}(°C)	0.78 [0.83]		T_{8cm}	2.22 [0.93]	T_{8cm}	1.941 [0.89]	
	T_{35cm}(°C)	0.60 [0.7]		T_{32cm}	1.04 [0.95]	T_{32cm}	1.208 [0.94]	
	T_{60cm}(°C)	0.36 [0.98]		T_{64cm}	0.61 [0.96]	T_{64cm}	0.857 [0.96]	
	T_{85cm}(°C)	0.15 [1]		T_{128cm}	0.12 [0.67]	T_{128cm}	0.048 [1]	

Table 2.3 Percentage fraction of incident solar radiation that is absorbed by the soil surface [$=(1-\alpha_s)e^{-k_a LAI}$] from Eq. (8). The fraction is given as a function of LAI assuming $\alpha_s = 0.14$ and $k_a = 1$

LAI	Ratio of absorbed solar radiation by the soil to the net downwelling radiation [%]
0.1	77.8
1	31.6
2	11.6
3	4.3
4	1.6

Figures

(a)

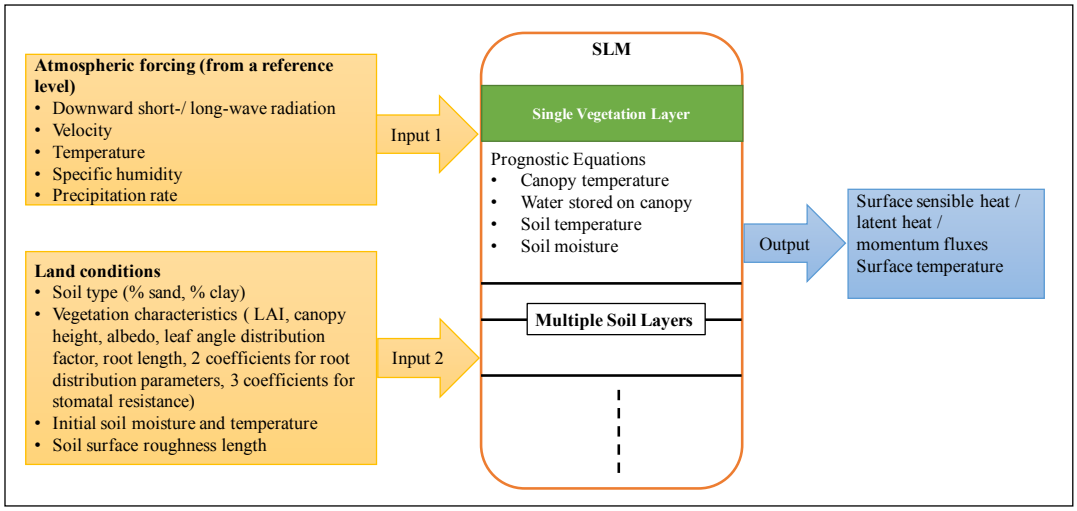
Atmospheric forcing (from a reference level)
• Downward short-/ long-wave radiation
• Velocity
• Temperature
• Specific humidity
• Precipitation rate
Input 1
Land conditions
• Soil type (% sand, % clay)
• Vegetation characteristics (LAI, canopy height, albedo, leaf angle distribution factor, root length, 2 coefficients for root distribution parameters, 3 coefficients for stomatal resistance)
• Initial soil moisture and temperature
• Soil surface roughness length
Input 2
SLM
Single Vegetation Layer
Prognostic Equations
• Canopy temperature
• Water stored on canopy
• Soil temperature
• Soil moisture
Multiple Soil Layers
Output
Surface sensible heat / latent heat / momentum fluxes
Surface temperature

(b)

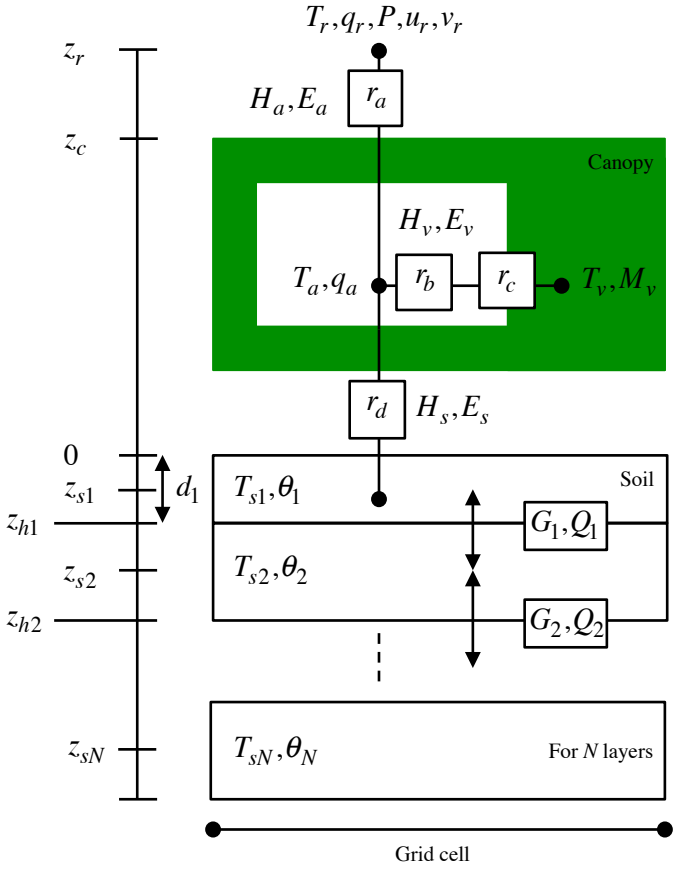
T_r, q_r, P, u_r, v_r
z_r
z_c
H_a, E_a
r_a
Canopy
H_v, E_v
T_a, q_a
r_b
r_c
T_v, M_v
r_d
H_s, E_s
0
z_{s1}
d_1
T_{s1}, θ_1
Soil
z_{h1}
G_1, Q_1
z_{s2}
T_{s2}, θ_2
z_{h2}
G_2, Q_2
z_{sN}
T_{sN}, θ_N
For N layers
Grid cell

Figure 2.1 (a) Diagram of SLM input and output data, describing what SLM is designed to do. (b) Simple schematic of SLM shows how the topsoil, canopy layer and reference level are coupled via canopy air space, and how heat and moisture conduction processes occur within the multi-level soil column. Mathematical symbols used in this figure are defined in Appendix B.

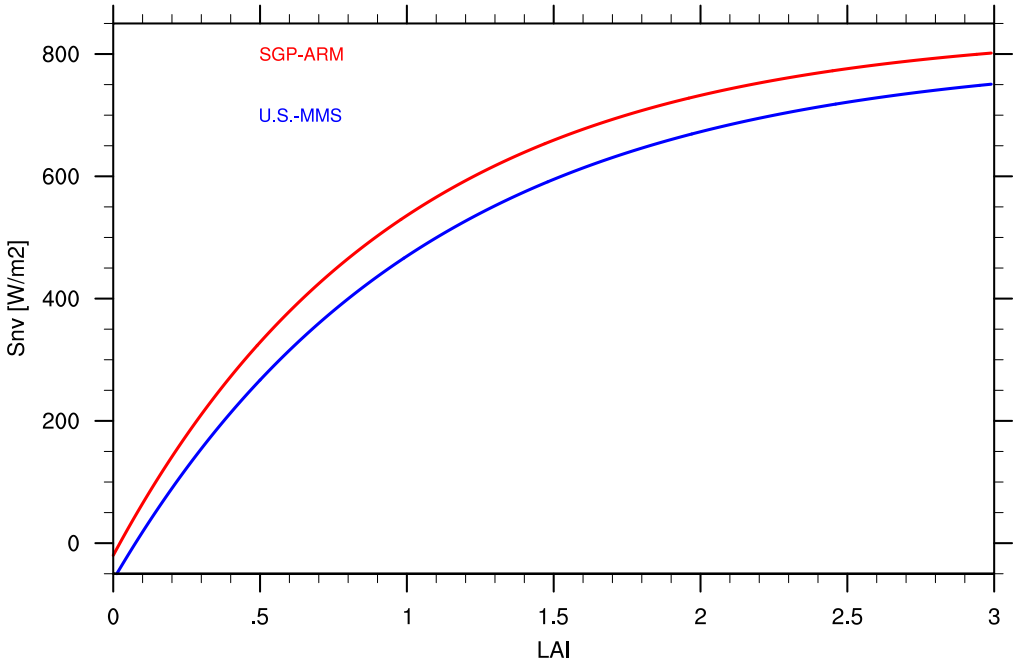

Figure 2.2 Net solar radiation of the canopy (5) over SGP-ARM and U.S.-MMS sites, and its dependency upon LAI. $S_{\downarrow}$ is set to 1000 W/m^2, k_a is approximated to 1, vegetation albedo and leaf angle distribution factor for each site are given in Table 2.1.

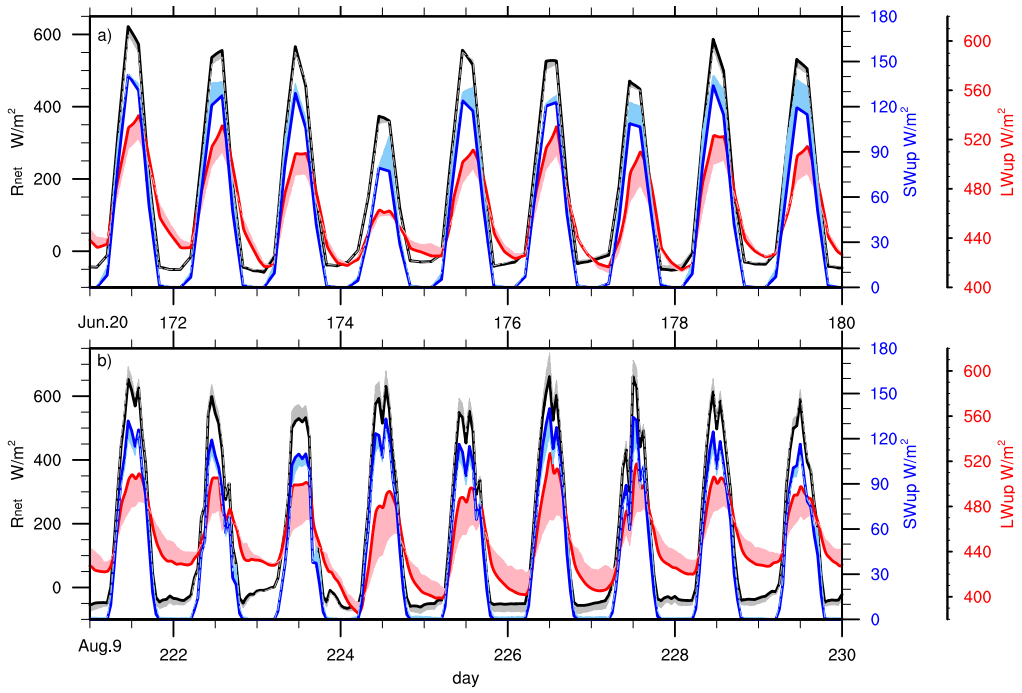

Figure 2.3 Simulated 9-day net radiation at surface R_{net} (black), upwelling solar (blue) and longwave radiation (red) over a) U.S.-ARM, b) U.S.-MMS, c) U.S.-Aud, and d) U.S.-Dk1. Simulated curves are in solid lines and the difference with the observation curves are shaded in colors. Each curve has a separate y axis.

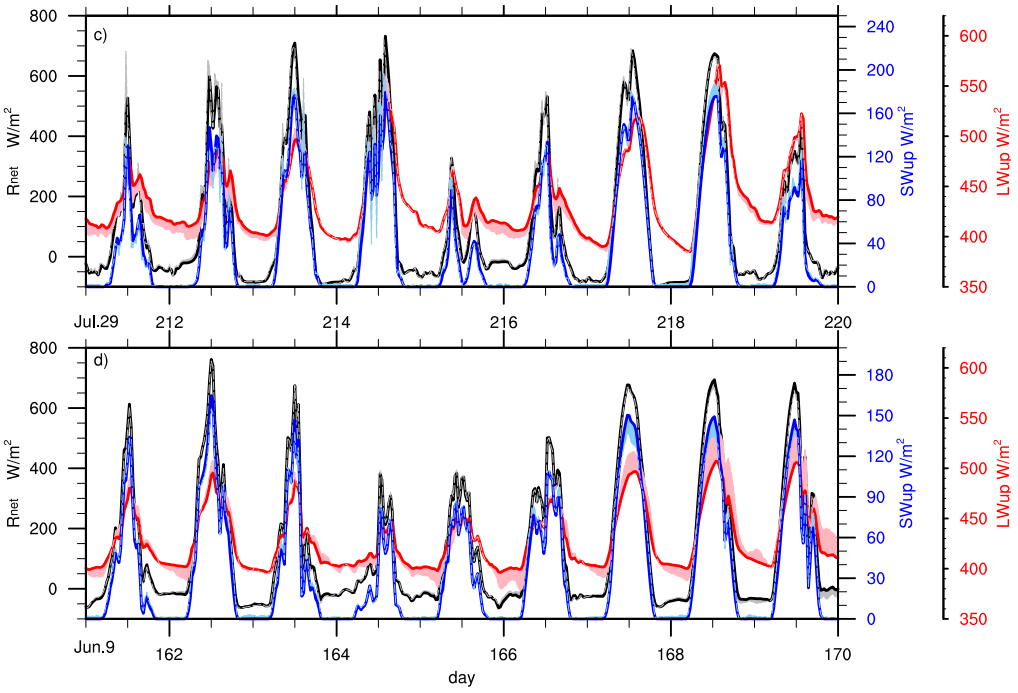

Figure 2.3 (Continued)

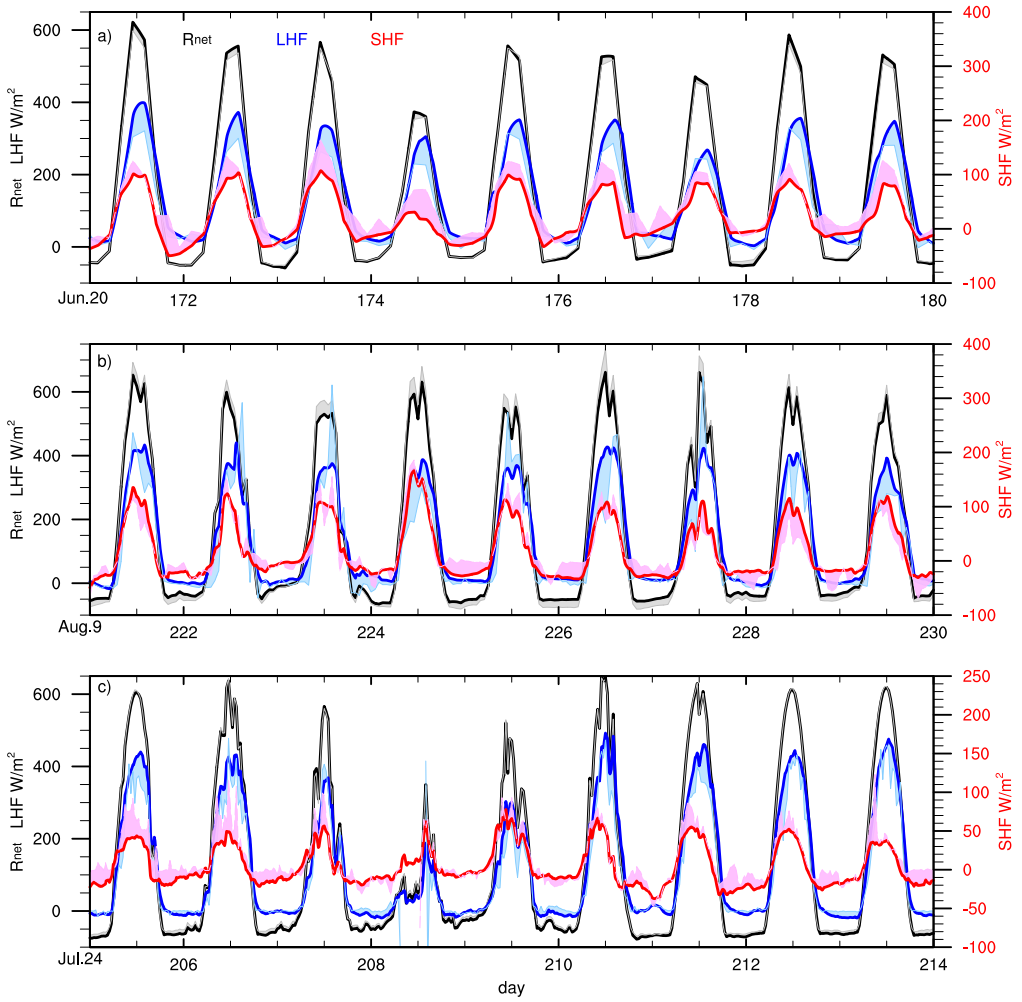

Figure 2.4 Simulated (lines) 9-day net radiation (black), latent heat flux (blue) and sensible heat flux (red) over a) U.S.-ARM, b) U.S.-MMS, c) U.S.-Bo1, d) U.S.-Aud, and e) U.S.-Dk1. Color shading shows the difference between the simulated and observed curves. Net radiation and latent heat flux share the same y axis (on the left) while the sensible heat flux is given by the y axis on the right.

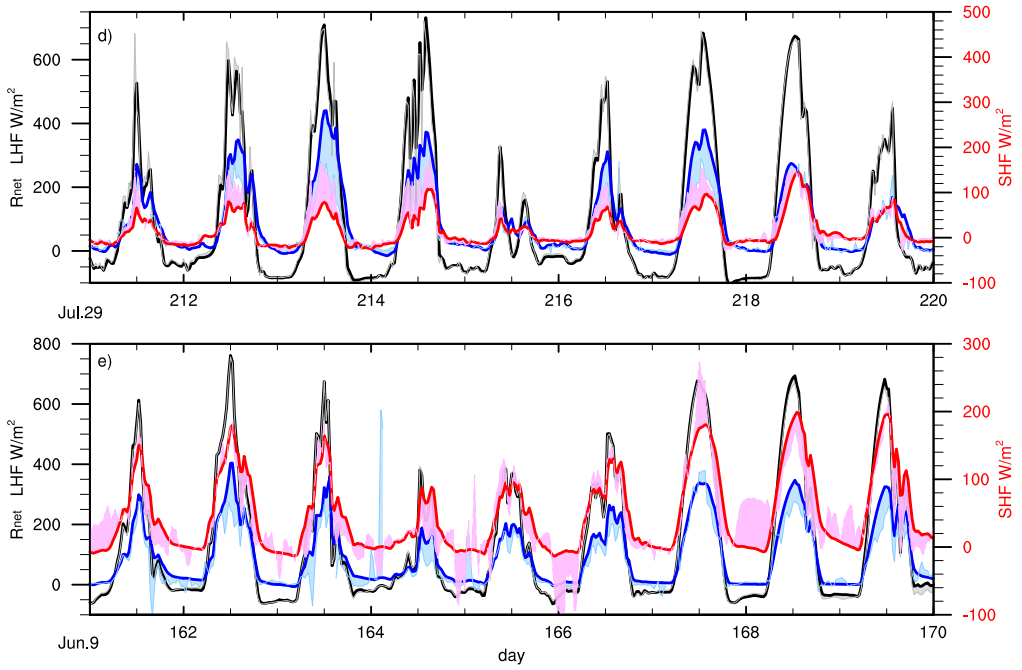

Figure 2.4 (Continued)

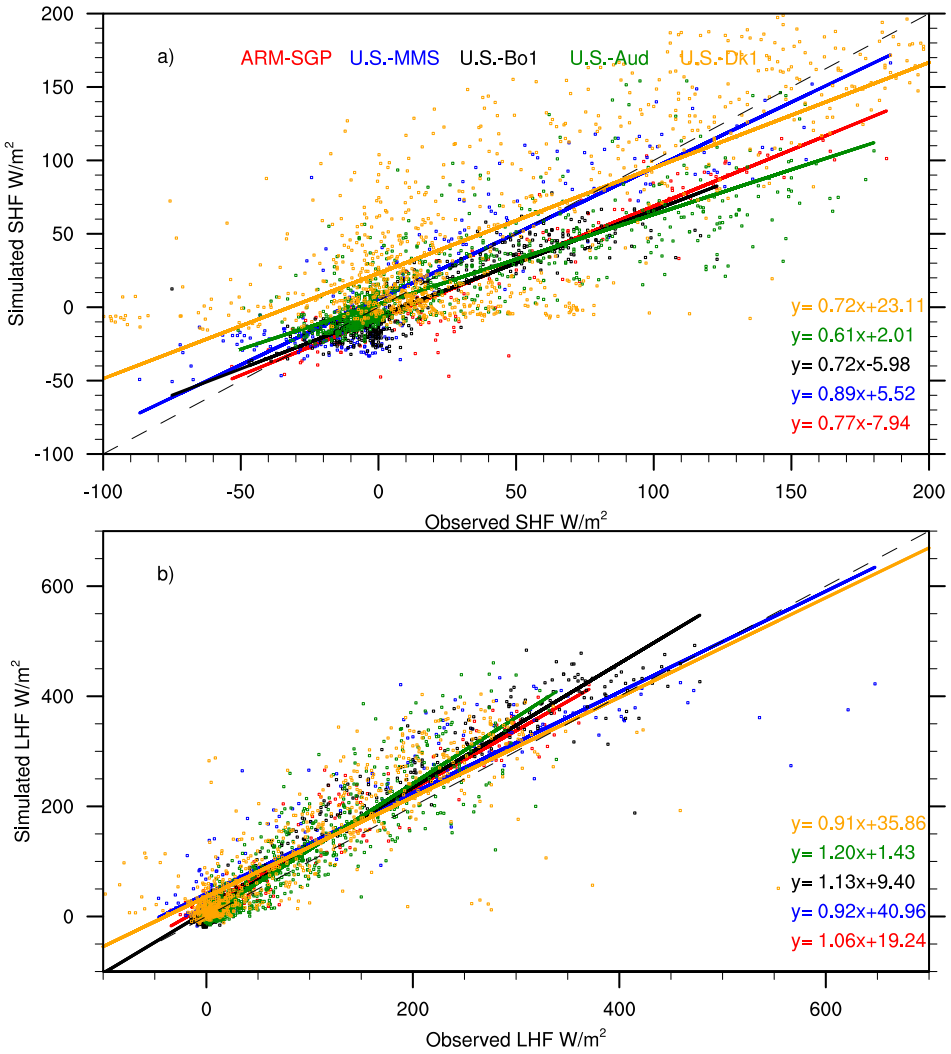

Figure 2.5 Scatter plot of modeled versus observed (a) sensible and (b) latent heat fluxes over ARM SGP (grasslands; red), U.S.-MMS (forest; blue), U.S.-Bo1 (cropland; black), U.S.-Aud (grasslands; green), and U.S.-Dk1 (grasslands; yellow). The solid line is a linear fit to the data of entire sampled period and the dashed line corresponds to 1:1 relationship between the observed and simulated values.

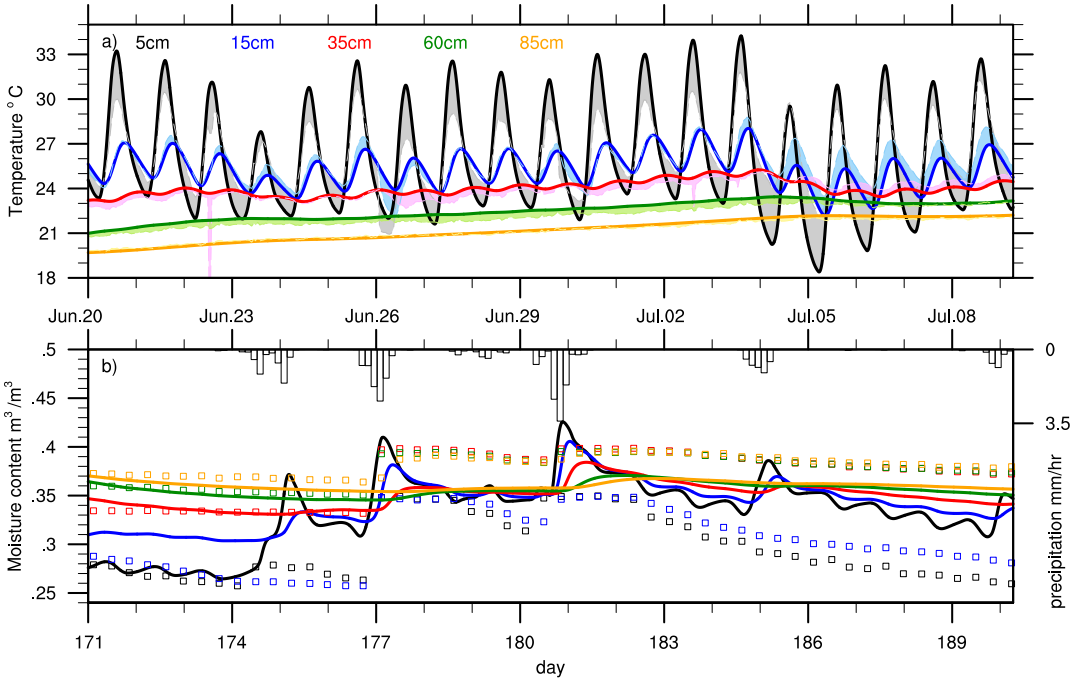

Figure 2.6 Simulated (lines) soil temperature (a) and volumetric moisture content (b) at selected depths (different colors) for ARM SGP case. Color shading represents differences between the simulated and observed soil temperature curves, and the colored open squares are the observed volumetric soil moisture content. Precipitation measurement at the observation site is also drawn as a bar chart with the soil moisture profiles.

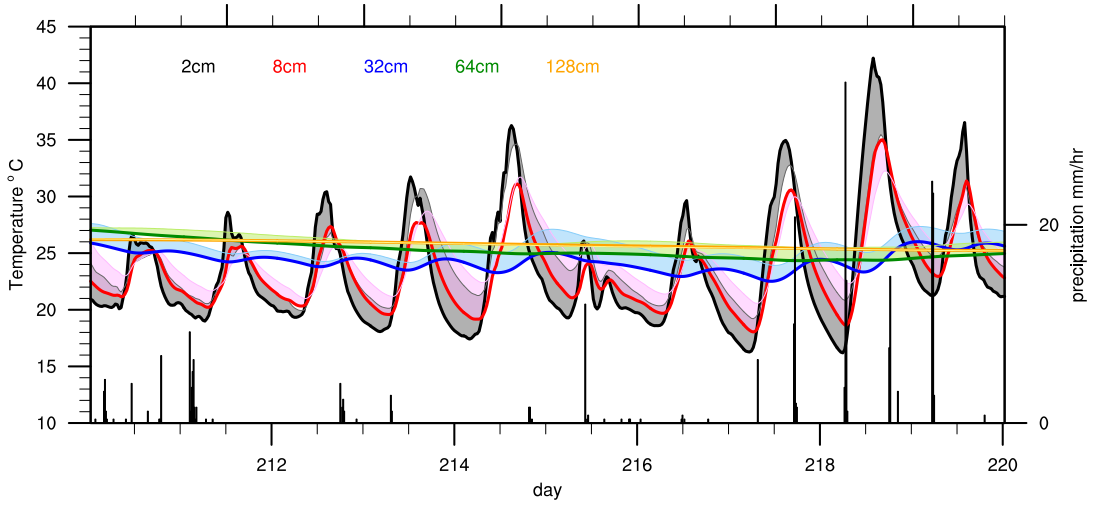

Figure 2.7 Simulated (lines) soil temperature at selected depths (different colors) for U.S.-Aud case. Color shading represents differences between the simulated and observed soil temperature curves. Precipitation measurements at the observation site are given as a bar chart with a separate y-axis.

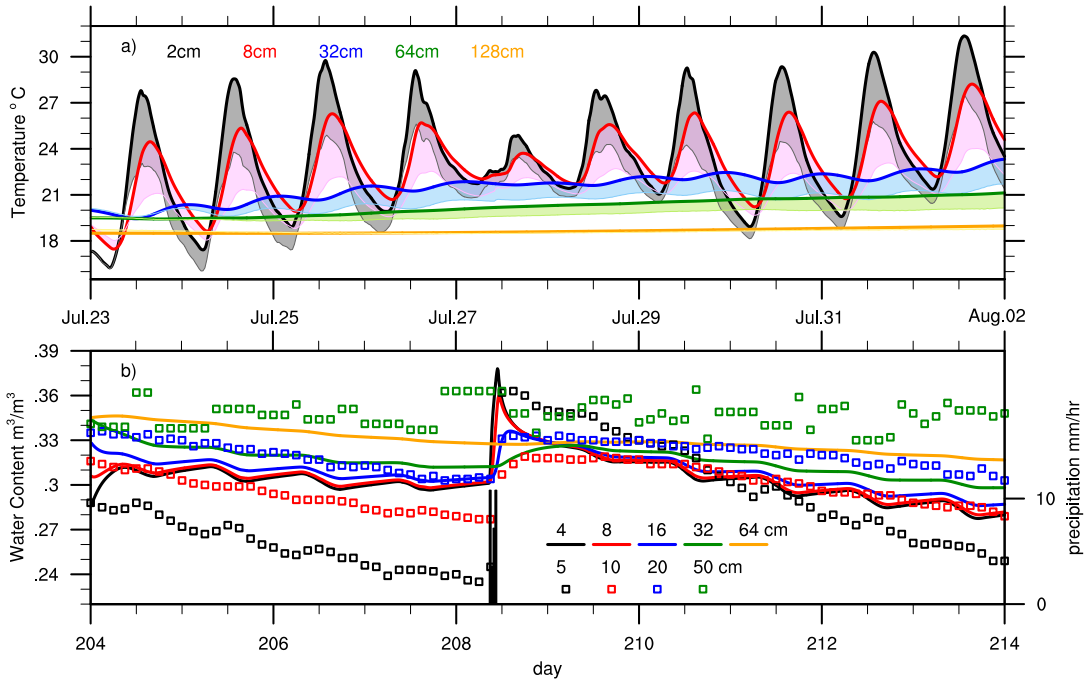

Figure 2.8 Simulated (lines) soil moisture and temperature profiles of selected depths at US-Bo1 site. The differences between the simulated and observed soil temperature curves are shaded in colors. The depths of simulated soil moisture are selected to be the closest match with the depths of measurement (markers). Also, precipitation (bar) is provided in the time series.

Appendix

Appendix A. Implementation of the implicit method in the soil heat and moisture transfer equations

a. Soil moisture transfer

Soil moisture balance is defined as

$$\frac{\partial \theta}{\partial t} = -\frac{\partial Q}{\partial z} - e \tag{A1}$$

where e is the external controls of soil moisture that include precipitation (source), drainage + evapotranspiration (sink), and the downward flow is defined to be positive.

Using the definition of soil hydraulic properties, (A1) can be rearranged to be in a flux form following:

$$\frac{\partial \theta}{\partial t} = -\frac{\partial}{\partial z} u\theta + \frac{\partial}{\partial z} \nu \frac{\partial \theta}{\partial z} - e$$
$$\begin{cases} \mathrm{u} = K_s \theta^{2B+2} \\ \nu = K_s B\left(-\psi_s\right)\theta^{B+2} \end{cases} \tag{A2}$$

where the first term on the right hand side represents the advection, and the second term accounts for the inter-layer diffusion. By definition, u and v are always positive.

The implicit method, which takes both current and subsequent time step information to diagnose the subsequent state, is applied to Finite-difference approximation of (A2).

$$\frac{\theta_k^{n+1} - \theta_k^n}{\Delta t} = -\frac{u_{k+\frac{1}{2}} \theta_k^{n+1} - u_{k-\frac{1}{2}} \theta_{k-1}^{n+1}}{d_k} + \frac{1}{d_k}\left[\nu_{k+\frac{1}{2}} \frac{\theta_{k+1}^{n+1} - \theta_k^{n+1}}{\frac{1}{2}\left(d_k + d_{k+1}\right)} - \nu_{k-\frac{1}{2}} \frac{\theta_k^{n+1} - \theta_{k-1}^{n+1}}{\frac{1}{2}\left(d_{k-1} + d_k\right)} \right] - e^n \tag{A3}$$

where index k+1/2 represents the interface between k and k+1, k-1/2 represents the interface between k-1and k, and n is a current time step. Other variables follow the definition listed in Appendix B. (A3) can be rearranged to

$$a_k W_{k-1}^{n+1} + b_k W_k^{n+1} + c_k W_{k+1}^{n+1} = d_k \quad [for \ \text{k=2, nsoil-1}]$$

$$\text{for } k=1 \begin{cases} a_1 = 0 & c_1 = -\dfrac{2\nu_{1+\frac{1}{2}}\Delta t}{d_1(d_1+d_2)} \\ b_1 = 1 + \dfrac{u_{1+\frac{1}{2}}\Delta t}{d_1} + \dfrac{2\nu_{1+\frac{1}{2}}\Delta t}{d_1(d_1+d_2)} & d_1 = W_1^n - e_1{}^n \Delta t \end{cases}$$

$$\text{for } k=2,N-1 \begin{cases} a_k = -\dfrac{u_{k-\frac{1}{2}}\Delta t}{d_k} - \dfrac{2\nu_{k-\frac{1}{2}}\Delta t}{d_k(d_{k-1}+d_k)} & c_k = -\dfrac{2\nu_{k+\frac{1}{2}}\Delta t}{d_k(d_k+d_{k+1})} \\ b_k = 1 + \dfrac{u_{k+\frac{1}{2}}\Delta t}{d_k} + \dfrac{2\nu_{k+\frac{1}{2}}\Delta t}{d_k(d_k+d_{k+1})} + \dfrac{2\nu_{k-\frac{1}{2}}\Delta t}{d_k(d_{k-1}+d_k)} & d_k = W_k^n - e_k{}^n \Delta t \end{cases}$$

$$\text{or } k=N \begin{cases} a_N = -\dfrac{u_{N-\frac{1}{2}}\Delta t}{d_N} - \dfrac{2\nu_{N-\frac{1}{2}}\Delta t}{d_N(d_{N-1}+d_N)} & c_N = 0 \\ b_N = 1 + \dfrac{2\nu_{N-\frac{1}{2}}\Delta t}{d_N(d_{N-1}+d_N)} & d_N = W_N^n - e_N{}^n \Delta t \end{cases}$$

(A4)

In a matrix representation,

$$\begin{pmatrix} b_1 & c_1 & 0 & 0 & 0 & 0 & 0 & 0 \\ a_2 & b_2 & c_2 & 0 & 0 & 0 & 0 & 0 \\ 0 & a_3 & b_3 & c_3 & 0 & 0 & 0 & 0 \\ 0 & 0 & . & . & . & 0 & 0 & 0 \\ 0 & 0 & 0 & . & . & . & 0 & 0 \\ 0 & 0 & 0 & 0 & . & . & . & 0 \\ 0 & 0 & 0 & 0 & 0 & . & . & . \\ 0 & 0 & 0 & 0 & 0 & 0 & a_{nsoil} & b_{nsoil} \end{pmatrix} \begin{pmatrix} W_1 \\ W_2 \\ W_3 \\ W_4 \\ . \\ . \\ . \\ W_{nsoil} \end{pmatrix} = \begin{pmatrix} d_1 \\ d_2 \\ d_3 \\ d_4 \\ . \\ . \\ . \\ d_{nsoil} \end{pmatrix} \quad \text{(A5)}$$

, which can be transformed into tri-diagonal matrix by dividing each row with b_k:

$$\begin{pmatrix} 1 & \alpha_1 & 0 & 0 & 0 & 0 & 0 & 0 \\ 0 & 1 & \alpha_2 & 0 & 0 & 0 & 0 & 0 \\ 0 & 0 & 1 & \alpha_3 & 0 & 0 & 0 & 0 \\ 0 & 0 & 0 & 1 & \alpha_4 & 0 & 0 & 0 \\ 0 & 0 & 0 & 0 & 1 & \alpha_5 & 0 & 0 \\ 0 & 0 & 0 & 0 & 0 & 1 & \alpha_6 & 0 \\ 0 & 0 & 0 & 0 & 0 & 0 & \ddots & \ddots \\ 0 & 0 & 0 & 0 & 0 & 0 & 0 & 1 \end{pmatrix} \begin{pmatrix} W_1 \\ W_2 \\ W_3 \\ W_4 \\ . \\ . \\ . \\ W_{nsoil} \end{pmatrix} = \begin{pmatrix} \beta_1 \\ \beta_2 \\ \beta_3 \\ \beta_4 \\ . \\ . \\ . \\ \beta_{nsoil} \end{pmatrix} \tag{A6}$$

Finally, W_k^{n+1} can be obtained by solving (A6), and the solution is defined as

$$\begin{aligned} & W_k = \beta_k - \alpha_k W_{k+1} \quad for \quad k = 1, N-1 \\ & W_N = \beta_N \\ & \begin{cases} \alpha_k = \dfrac{c_k}{b_k - a_k \alpha_{k-1}} \\ \beta_k = \dfrac{d_k - a_k \beta_{k-1}}{b_k - a_k \alpha_{k-1}} \end{cases} \end{aligned} \tag{A7}$$

b. Soil temperature transfer

The same, introduced above, is applied to soil energy budget equation to solve for T_k at t = (n+1) time step.

$$c \frac{\partial T}{\partial t} = -\frac{\partial}{\partial z}\left(-\lambda \frac{\partial T}{\partial z} \right) \tag{A8}$$

After applying finite-difference approximation, (A8) is rearranged as

$$a_k T_{k-1}^{n+1} + b_k T_k^{n+1} + c_k T_{k+1}^{n+1} = f_k$$

$$\text{for } k=1 \begin{cases} a_1 = 0 & c_1 = -\dfrac{2\lambda_{1+\frac{1}{2}}\Delta t}{c_1 d_1 (d_1 + d_2)} \\ b_1 = 1 + \dfrac{2\lambda_{1+\frac{1}{2}}\Delta t}{c_1 d_1 (d_1 + d_2)} & f_1 = T_1^n - \dfrac{G_0 \Delta t}{\Delta t} \end{cases}$$

$$\text{for } k=2,N-1 \begin{cases} a_k = -\dfrac{2\lambda_{k-\frac{1}{2}}\Delta t}{c_k d_k (d_{k-1} + d_k)} & c_k = -\dfrac{2\lambda_{k+\frac{1}{2}}\Delta t}{c_k d_k (d_k + d_{k+1})} \\ b_k = 1 + \dfrac{2\lambda_{k+\frac{1}{2}}\Delta t}{c_k d_k (d_k + d_{k+1})} + \dfrac{2\lambda_{k-\frac{1}{2}}\Delta t}{c_k d_k (d_{k-1} + d_k)} & f_k = T_k^n \end{cases}$$

$$\text{for } k=N \begin{cases} a_N = -\dfrac{2\lambda_{k-\frac{1}{2}}\Delta t}{c_k d_k (d_{k-1} + d_k)} & c_N = 0 \\ b_N = 1 + \dfrac{2\lambda_{N-\frac{1}{2}}\Delta t}{c_N d_N (d_{N-1} + d_N)} & f_N = T_N^n \end{cases} \tag{A9}$$

Boundary layer condition for top and bottom of the soil is applied above. The top boundary condition states the incident heat flux is G_0 (=R_n-H_a-E_a), and there is no heat leaving or entering through the bottom of the soil column. Thus, the solution of soil temperature at each layer follows

$$T_k = \beta_k - \alpha_k T_{k+1} \quad for \quad k = 1, N-1$$

$$T_N = \beta_N$$

$$\begin{cases} \alpha_k = \dfrac{c_k}{b_k - a_k \alpha_{k-1}} \\ \beta_k = \dfrac{d_k - a_k \beta_{k-1}}{b_k - a_k \alpha_{k-1}} \end{cases} \tag{A10}$$

Appendix B. List of symbols

Symbol	Name	Value or formulation	Unit
a	Constant used in C_{bare}	0.13	
B	Empirical soil parameter		
C_{bare} / C_{dense}	Turbulent transfer coefficient under no canopy/ dense canopy		
C_D / C_H	Turbulent transfer coefficient for momentum and heat transfer		
c_p	Specific heat of air	1004	$JKg^{-1}K^{-1}$
$c_{p\ vege}$	Specific heat of vegetation		$Jm^{-2}K^{-1}$
c_{si} / c_{solids}	Heat capacity of soil layer i / soil soilds		$JKg^{-1}K^{-1}$
c_{water}	Volumetric heat capacity of water	4.1796×10^{6}	$Jm^{-3}K^{-1}$
C_{uv}	Turbulent transfer coefficient under canopy		
C_v	Turbulent transfer coefficient on foliage	0.01	$m/s^{0.5}$
d_i	Soil layer thickness		m
d_{leaf}	Leaf length scale	0.04	m
d_{root}	Sum of the depth of soil layers with root		m
D_v	Water drainage rate from canopy		kg/m^2s
E_{tr} / E_{wv}	Transpiration / direct evaporation from water on canopy		W/m^2
E_v / E_s / E_a	Vegetation/ soil / total latent heat flux		W/m^2
f_{F1}	Parameter used in F_1		
f_{F2}	Parameter used in F_2		
f_h	Relative humidity of soil pore space exposed to overlying air		

$F_{root\ i}$	Fraction of root that exists in a layer i		
$F_{1\text{-}4}$	Environmental factors of stomatal resistance		
g	Gravitational acceleration	9.8	m/s^2
$G(\mu)$	Solar radiation's mean projected area over canopy in the direction of sun's inclination		
G_i	Soil heat flux at interface i		W/m^2
H_v / H_s / H_a	Vegetation / soil (undercanopy) / total sensible heat flux		W/m^2
k	von Karman's constant	0.4	
k_a	Extinction coefficient		
KR_i	Kersten number of soil layer i		
K_i/ K_{hi} / K_s	Hydraulic conductivity at soil layer i / interface i / at saturation		m/s
L	Monin-Obukhov stability parameter		
LAI	Leaf Area Index		
L_{root}	Vegetation root depth		m
L_{ns} / L_{nv}	Net longwave radiation absorbed by soil / vegetation		W/m^2
L_a / L_b	Parameters related to the root structure		
L_v	Latent heat of condensation	2.5104×10^6	J/kg
$L_{\downarrow}$	Downwelling longwave radiation from reference level		W/m^2
M_v	Water amount held on vegetation		kg/m^2
N	Total number of soil layers		
P / P_v / P_0	Precipitation rate from the reference level / intercepted by canopy / reaching to topsoil		kg/m^2s
P_f	Direct fall through rate from canopy		kg/m^2s
P_I	Precipitation infiltration rate		kg/m^2s
q_a/ q_r / q_*	Specific humidity of canopy air space / reference level/ at saturation		kg/kg

Q_i	Water transport rate at soil interface *i*		m/s
Q_{dr}	Soil bottom layer drainage rate		m/s
qrz	Quartz content		
r_a, r_b, r_d	Aerodynamic resistances		s/m
r_c	Stomatal resistance		s/m
r_{cmax}	Maximum stomatal resistance	5000	s/m
r_{cmin}	Minimum stomatal resistance		s/m
R_e / R_{ec}	Reynold's number / Critical Reynold's number	$\frac{u_* z_o}{\nu}$ / 70	
R_{gl}	Minimum solar radiation required for transpiration		W/m^2
R_{nv} / R_{ns}	Net radiation on vegetation / on topsoil		W/m^2
Ro_{sfc}	Surface runoff rate		kg/m2s
R_v	Gas constant for water vapor	461	$Jkg^{-1}K^{-1}$
S_{ns} / S_{nv}	Shortwave radiation absorbed by soil / by vegetation		W/m^2
S_v	Maximum water amount held on vegetation		kg/m^2
$S_{\downarrow}$	Downwelling shortwave radiation from reference level		W/m^2
T_a / T_r / T_v / T_{si}	Temperature of canopy air space / reference level / vegetation / soil layer *i*		K
T_p	Potential temperature		K
T_{opt}	Optimum temperature for transpiration	298	K
T_*	Temperature scale		K
u	velocity		m/s
u_*	Friction velocity		m/s
u_r / v_r	Zonal / meridional wind at reference height z_r		m/s
V_r	Wind speed at reference level	$\sqrt{u_r^2 + v_r^2}$	m/s

$W_{s\,i}$ / W_v	Wetness of soil layer *i* / of vegetation		
z_c	Canopy height		m
z_{disp}	Displacement height		m
z_i	Center depth of soil layer *i*		m
z_o / z_{oh}	Surface roughness length for wind / heat		m
α_{s1} / α_{s2}/ α_{s3}	Soil albedo parameters	0.31/ 0.34/ 0.14	
α_s / α_v	Soil surface / vegetation albedo		
β	Molecular diffusion factor for soil evaporation		
γ	Constant in C_{dense}	0.5	
γ_d	Dry soil density		kg/m^3
Δt	time step		s
δ_{tv}	Fractional area of under canopy shade	$1-e^{-LAI}$	
ε_v	Vegetation emissivity for infrared radiation		
η / η_{min}	Undercanopy stability parameter / Lower threshold of η	/ 10	
θ_i / θ_s / θ_{fc} / θ_{wilt}	Volumetric soil moisture content at layer *i* / saturation/ field capacity / wilting point		
θ_z	Solar zenith angle		
λ_i / λ_{hi} / λ_{sat} / λ_{dry} / λ_s / λ_w / λ_q / λ_o	Thermal conductivity of soil layer *i* / soil interface *i* / saturated soil / natural dry soil /soil solids / water /quartz / minerals	λ_w=0.57 λ_q=7.7	W/mK
μ		$\cos\theta_z$	
v	Viscosity	1.5×10^{-5}	m^2/s
ρ_a / ρ_w	Density of air / water	/ 10^3	kg/m^3
σ	Stefan-Boltzmann constant	5.67×10^{-8}	$Js^{-1}m^{-2}K^{-4}$
τ_x , τ_y	Surface stress in x-, y-direction		$kgm^{-1}s^{-2}$
χ_L	Leaf angle distribution factor		

ψ_i / ψ_s	Soil moisture potential at soil layer *i* / at saturation	m
Φ_M / Φ_H	Stability function for momentum/ heat	
ϕ_1 , ϕ_2	Parameters used in extinction coefficient k_a	
%SAND/ %CLAY	Percentage fraction of sand / clay	%

Chapter 3: Diurnal cycle of PBL over various land surfaces

3.1 Introduction

Turbulent transfer of heat, momentum and energy are the keys to the physical interactions between land and atmosphere. Although large-eddy simulation (LES) models are capable of resolving various sizes of turbulent eddies in the PBL, their use to simulate interactions between land and atmosphere has been quite limited. In fact, in most previous LES studies of the diurnal convection over land, the surface heat fluxes at the bottom boundary condition have been usually prescribed, as most LES models lacked a comprehensive land model coupled to them (e.g., Khairoutdinov and Randall, 2006; Petch et al., 2002; Bechtold et al., 2004; Chaboureau et al., 2004; Guichard et al., 2004; Wu et al., 2009 etc.). Development of a land model for use in SAM as an LES model has been one of the main motivations that started the work on this thesis.

In this chapter, we show the result of applying the new modeling framework, SAM-SLM, to the LES of the diurnal cycle of cloudy PBL over land. The Chapter is organized as follows. Section 3.2 introduces a new modeling framework, SAM-SLM, as well as describes the simulation set-up. In section 3.3, the performance of SAM-SLM is tested on a case of shallow cumulus cloud development during daytime over land. Influence of soil moisture and vegetation types on the surface energy budget, and the implication on the thermodynamics in PBL is discussed in section 3.4.

3.2 Numerical experiment design

3.2.1 The model

The model for this study is based on SAM 6.10. The dynamical core of SAM solves non-hydrostatic equations of motion using anelastic approximation. Thermodynamic prognostic

variables include liquid water/ice static energy, total precipitating water (rain + snow + graupel), and total non-precipitating water (water vapor + cloud water + cloud ice). Liquid water/ice static energy is conserved except for the fallout of hydrometeors. A single-moment microphysics scheme is employed. Mixing ratios of various hydrometeors are defined diagnostically by applying appropriate partitioning functions, which depend only on the temperature, on prognostic thermodynamic variables. In this study, SAM employs the radiation scheme used in National Center for Atmospheric Research (NCAR) Community Atmosphere Model (CAM3; Collins et al. 2006). A "sponge" layer in the upper third of the domain prevents the reflection of gravity waves by damping the prognostic velocity components. The lateral boundaries are doubly periodic. Surface fluxes to force the bottom boundary of atmosphere are computed from the SLM given the atmospheric temperature, specific humidity, horizontal winds, precipitation and radiation budget at a reference level, which is taken to be the lowest vertical level of SAM. The land surface temperature computed from SLM is used to determine the surface emission of longwave radiation.

3.2.2 Description of test cases

The numerical experiments reported here are based on an LES model intercomparison study as described by Brown et al. (2002). The study is an idealized case of daytime development of shallow cumulus convection over land based on observations at the Southern Great Plains (SGP) ARM site made on June 21, 1997. The evolution of shallow non-precipitating clouds in this case is characterized by the gradual increase of cloud top heights that reach maximum in the late afternoon. The case LAND-OFF (SLM is disabled) closely follows a specification of the original LES study referenced above using prescribed surface fluxes and radiative cooling rates. The case LAND-ON uses the SLM to compute the surface heat fluxes. The land surface parameters are similar to those used for the ARM-SGP evaluation case described in Chapter 2 (see Table 2.1). The initial soil temperature and moisture profiles are specified from the averaged Soil Water and Temperature System (SWATS; Schneider et al., 2003) data collected at the SGP site on June 21, 1997. The soil wetness in the LAND-ON case ranged from 0.6 to 0.68 throughout the depth of the soil. In order to see how soil moisture affects the evolution of the shallow clouds over land, simulation DRY has also been conducted, which is similar to the LAND-ON, but with the initial soil moisture profile significantly reduced to be in the range from 0.1 to 0.3. Finally, to see how

different land types affect the PBL evolution, LAND-ON simulation is repeated, but for three other land-surface types that include cornfield, forest, and baresoil. The parameters that are used to characterize the land surface vegetated with crops and forest are similar to those of U.S.-Bo1 and U.S.-MMS listed in Table 2.1. A baresoil case is represented in SLM by setting leaf area index (LAI) to zero.

3.2.3 Numerical set-up

In all simulations, the horizontal domain was 6403.2×6403.2 m^2, with the grid spacing of 66.7 m. For the LAND-OFF case, the grid in the vertical had 128 levels with 40 m grid spacing, extending up to 5,120 m. For the interactive land cases, the vertical grid was extended to 21 km with the grid gradually coarsening to 250m in the upper part of the domain. A stretched vertical domain was needed to compute longwave radiative fluxes that depend on the thermodynamic profiles in the troposphere well above the PBL. The simulations were initialized at 5:30 am and ran to 7:30 pm (19:30) of local time using a 2 s time step. The initial profile of potential temperature above 3 km differed between the coupled and uncoupled runs. For LAND-OFF, we closely followed the set up described by Brown et al. (2002), where the temperature profiles contained added stability above 3 km to prevent the cloud top from reaching the domain boundary. However, in the interactive cases with the extended vertical top, the initial profile of potential temperature above 3 km was kept close to the Central-Facility (CF) sonde observations. Separate tests were conducted to see the impact of this modified sounding above 3km. The sounding with very stable free troposphere, which was linearly interpolated from the LAND-OFF sounding, produced an evolution of the cloud top that was similar to LAND-ON case (not shown). The original case study by Brown et al. (2002) also mentioned that the artificially increased stability near the domain top did not seem to affect the cloud top height in this test case, which was defined well below the domain top.

In all cases, following Brown et al. (2002), SAM was forced by the advective tendency of cooling that gradually scaled up to -0.16 K/hr for the last 6 hours of simulated period in PBL. Also, the advective tendency for moisture in the PBL was specified to be 0.08 g kg^{-1} hr^{-1} in the beginning of the run and -0.3 g kg^{-1} hr^{-1} at the end of simulation, with the intermediate values found by linear

interpolation. An initial wind of 10 m/s was imposed in all vertical levels and the random small temperature noise below 200m height was applied to initialize turbulence.

3.3 Development of shallow cumulus convection over land

The ability of the new model, SAM-SLM, to simulate the diurnal evolution of PBL over land has been evaluated by comparing the LAND-OFF and LAND-ON cases. Figure 3.1 shows that the simulated surface heat fluxes are generally within the range estimated from the two different methods applied to the micrometeorological measurements. The main difference between the modeled and prescribed fluxes occurs during the morning and evening transition period, highlighted by the underestimation (overestimation) of evaporation (sensible heat flux) in the morning and the overestimation (underestimation) in the evening. As shown in Fig. 3.2, both cases reproduce the deepening of the mixed-layer during daytime time as expected. However, the difference in the surface heat fluxes during the initial stage of the simulations influences the thermodynamics of the mixed layer for the duration of the simulation. The LAND-ON case produces a well-mixed layer characterized by warmer temperature (less than 1 °C) and higher humidity (less than 1 g/kg) near the surface in response to the slightly enhanced surface heating and reduced evaporation in the morning. After 6 pm, a shallow stable layer near the surface develops early in LAND-ON because of the enhanced surface cooling by the lower sensible heat flux. Lower specific humidity throughout the day in LAND-ON is due to the enhanced mixing with the dry air above the deeper mixed layer compensating the increase from the higher evaporation rate during the morning and evening transition. Also, the change of specific humidity in LAND-ON is slower as the latent heat flux in that case is about 50 W/m^2 lower at the time when radiation is at its peak. Overall, the computed surface sensible and latent heat fluxes agree quite well with the fluxes obtained from in-situ observations, it is not surprising that the evolution of temperature and specific humidity profiles in LAND-ON and LAND-OFF are similar. The simulation results also broadly agree with the LES results reported by Brown et al. (2002).

3.4 Sensitivity tests

3.4.1 Sensitivity to soil moisture

Figure 3.3 compares the time series of the surface energy budget from LAND-ON and DRY cases, which differs only by the initial soil moisture content. The net radiation in LAND-ON is substantially larger than in DRY by as much as ~ 100 W/m2 because of the relationship between soil moisture and albedo. Wetted soil becomes darker and reduces the albedo; therefore, more incoming solar radiation was absorbed in LAND-ON. Also, water has a higher heat capacity than air; therefore, in comparison to the dry soil, the wet soil has higher heat capacity. In LAND-ON, temperature evolves at a slower pace due to higher capacity for heat gain/loss; therefore, the radiation effect is smaller.

Another significant impact that the soil moisture has on simulation is the 'flipping' between the latent and sensible heat fluxes, that is the sensible heat flux in DRY became dominant over the latent heat flux, while the opposite is true in LAND-ON. Consequently, a deeper, warmer and drier mixed-layer develops in DRY as shown in Fig. 3.4. The lifting condensation level is also considerably higher in DRY as indicated by much higher cloud base as shown in Fig. 3.5.

3.4.2 Sensitivity to vegetation types

The evolution of surface energy fluxes over four different land types (grassland, cropland, forest and baresoil) is presented in Fig. 3.6. The net radiation absorption at the surface is barely sensitive to the land type, which is mostly due to similar values of surface albedos in the range of 0.14-0.16 (Table 2.1) and the soil of given moisture level (see (9)); however, the partitioning into the latent and sensible heat fluxes is dependent on the type of land surface. Both forest and cropland have higher LAI, which is expected to enhance the evaporation potential mostly by increased moisture storage on leaves, and also by increased transpiration from stomata. In contrast, evaporation over the baresoil is reduced considerably owing to significant drying near upper soil levels as can be seen in Fig. 3.7. Forest shows the least moisture loss mostly due to uptake of soil moisture by transpiration of big trees approximately concentrated in mid drier soil layers, and due to shading of the under-canopy which reduces the evaporation from the soil surface. Although there is a rather extensive drying of the topsoil layer in the case of grassland, the modeled grass is able to recharge the moisture from deep soil layers; therefore, the reduction of evaporation from the drier soil is largely compensated by the transpiration.

Figure 3.8 shows the evolution of boundary layer over various land surface types. Until mid afternoon, grassland and forest develops a deeper and warmer mixed layer in response to the enhanced heating from the surface. In contrast, partitioning of the absorbed radiation over cornfield is dominated by evaporation, which leaves only little energy to spare for the turbulent heat exchange; therefore, the mixed-layer is moistened by an additional 2 g/kg of mixing ratio due to increased surface evaporation in the shallower and also cooler by more than 1 K boundary layer. Also, as the turbulence is mostly driven by the buoyancy flux, which in turn mostly depends on the sensible heat flux, the PBL does not deepen during daytime as much as in other cases. The boundary layer is the driest over baresoil.

Figure 3.9 shows the diurnal cycle of cloud formation and the resolved buoyancy flux extracted for mid-day and late afternoon over different land types. The cornfield has substantially lower cloud base, which is consistent with the shallower mixed-layer of high humidity. Virtually no sensitivity of the cloud top height to the land types is found because the buoyancy reduction due to cooler temperature is partly offset by the increased buoyancy from the water vapor supplied from the increased surface evaporation. However, the dissipation of the clouds occurs almost 1 hour earlier over the cornfield and forest, because the buoyancy reduction is no longer compensated by the supply of moisture after the evaporation ceases.

3.5 Summary

This chapter presented a novel way to explore the various cases of summertime shallow cumulus convection over land using a new SAM-SLM model, which is the LES/CRM coupled with interactive land model, SLM. The performance of the coupled model has been evaluated using an idealized case of diurnal evolution of shallow convection over land based on the observations over the ARM SGP site in summer 1997. The simulated surface heat fluxes in LAND-ON match rather closely the observations, where the latent heat flux was as large as 500 W/m2 and sensible heat flux was as high as 150 W/m2. The simulated evolution of the mixed-layer in LAND-ON follows the observed daytime deepening of mixed-layer over that the site.

Sensitivity tests have been conducted to examine the role of soil moisture on the development of PBL over land. The results produced by the coupled SAM-SLM model have been consistent with the expected increase of the sensible heat flux and corresponding decrease of

surface evaporation under dry soil conditions. Consequently, the drier soil environment reproduced the dryer, deeper and warmer PBL with the higher cloud base.

In addition, the evolution of the PBL in response to the changes in vegetation type were examined using the parameters characteristic of grassland, cropland (corn), forest and baresoil. The net surface radiation did not show a great sensitivity to the land types, which was mostly due to the similar surface albedo (0.14 - 0.16); however, the transpiration rate showed a significant dependency on the land type. For example, in late afternoon, the difference in latent heat flux between cornfield and baresoil was found to differ by as much as 200 W/m^2. The differences in surface fluxes translated to relatively large differences in PBL characteristics. For instance, the PBL temperature and humidity differed by as much as 2 K and 3 g/kg, respectively, with the variation of PBL height being as large as several hundred meters.

Overall, the daytime shallow convection over land simulated by SAM-SLM is qualitatively consistent with our general physical understanding of the processes in the convective PBL over land, in which the land surface and lower atmosphere interacted on subdiurnal time scales.

Figures

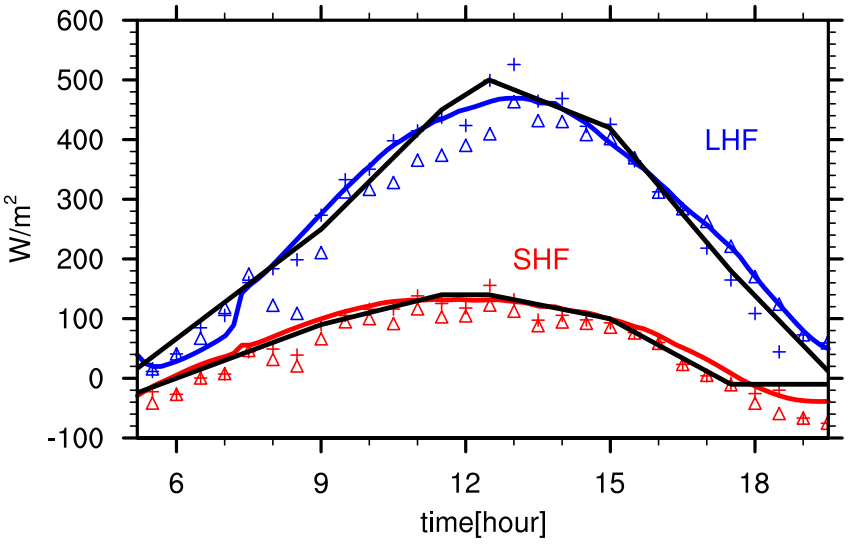

Figure 3.1. Observed (markers), prescribed (fitted to the observation; black lines) and modeled (colored lines) surface sensible and latent heat fluxes over ARM SGP on 21 June, 1997. Central-facility (CF) Tower measurements of surface net radiation, soil heat flux and the vertical gradient of temperature and humidity are used to estimate the surface fluxes (crosses) by considering the energy balance and Bowen ratio. Another estimation of surface fluxes (triangles) is based on the bulk aerodynamic method using the meteorological data collected at the CF observation tower.

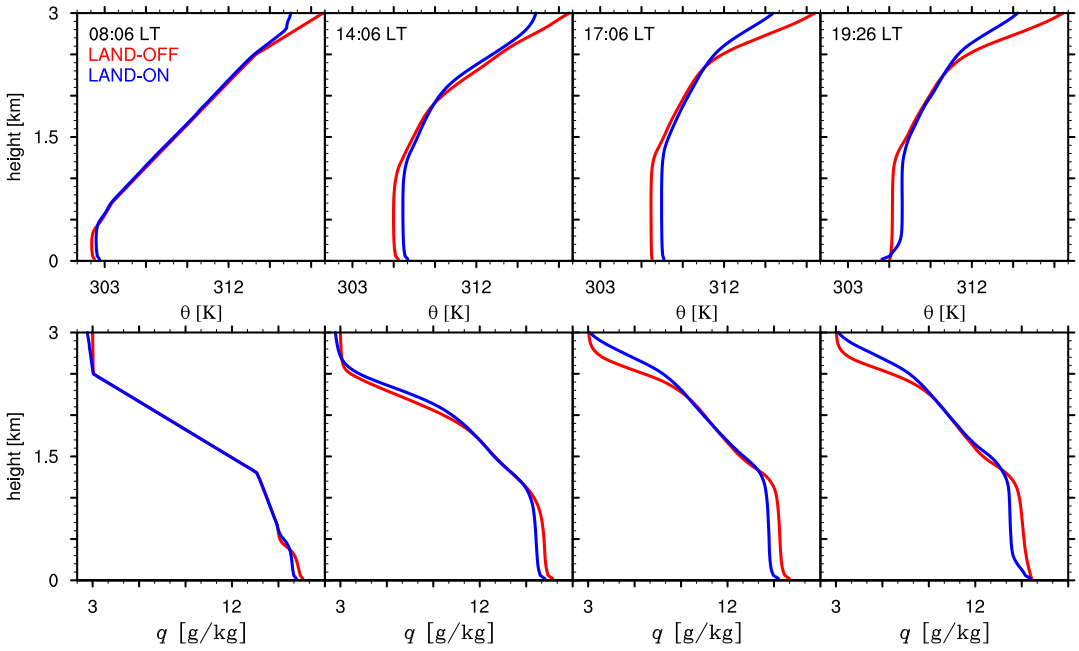

Figure 3.2 Comparisons of potential temperature (top) and specific humidity (bottom) profiles for LAND-ON and LAND-OFF cases at various time of a day. Times are in local hour.

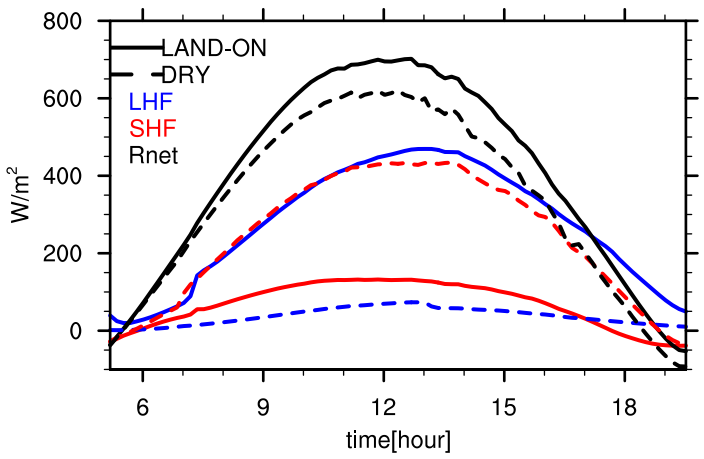

Figure 3.3. Surface fluxes for the wet LAND-ON (solid lines) and DRY (dashed lines) cases.

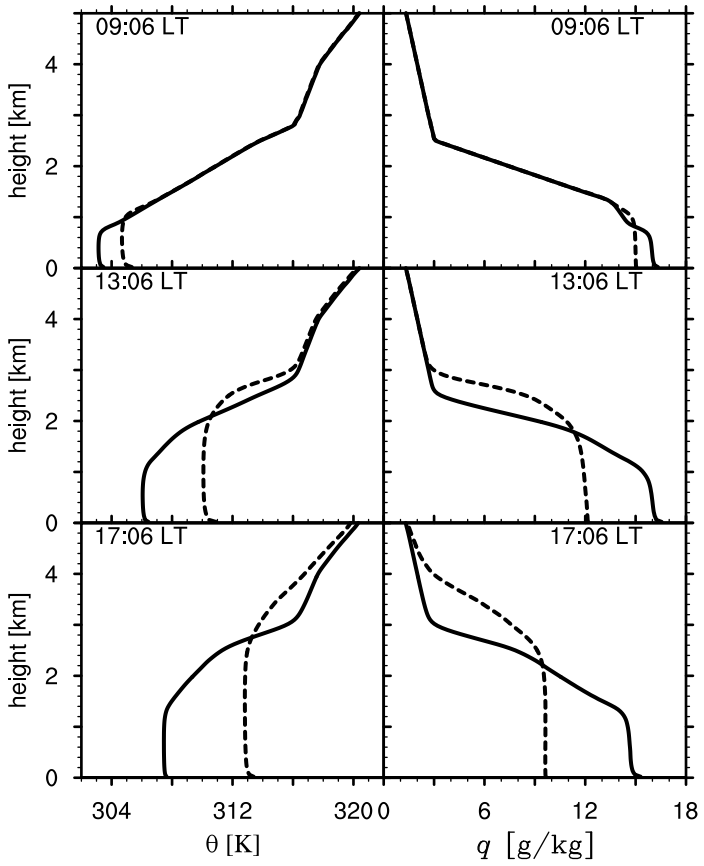

Figure 3.4 Comparisons of potential temperature (left), specific humidity (right) profiles for the wet LAND-ON (solid) and DRY (dashed) cases at various time of a day. Times are in local hour.

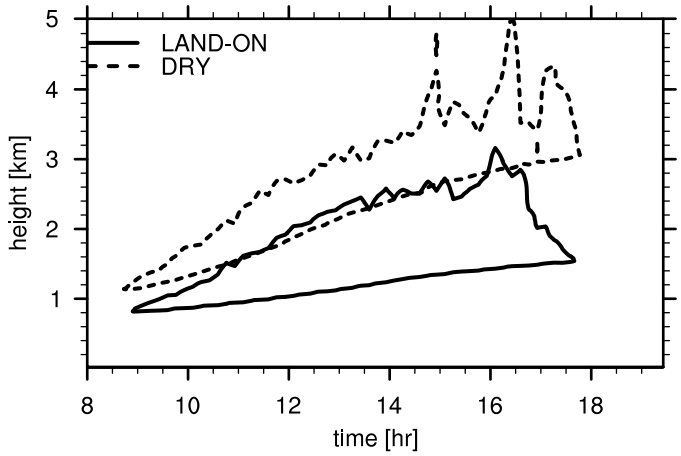

Figure 3.5 Evolution of cloud base and maximum cloud top height in LAND-ON and DRY case. Time is in local hour.

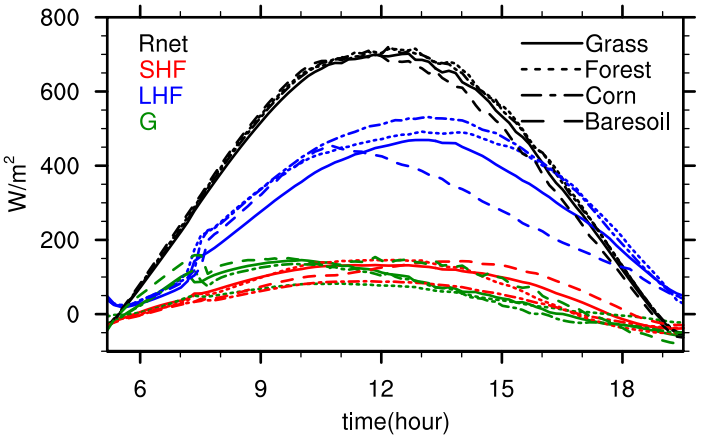

Figure 3.6. Surface fluxes for different land surface types as simulated by SAM-SLM.

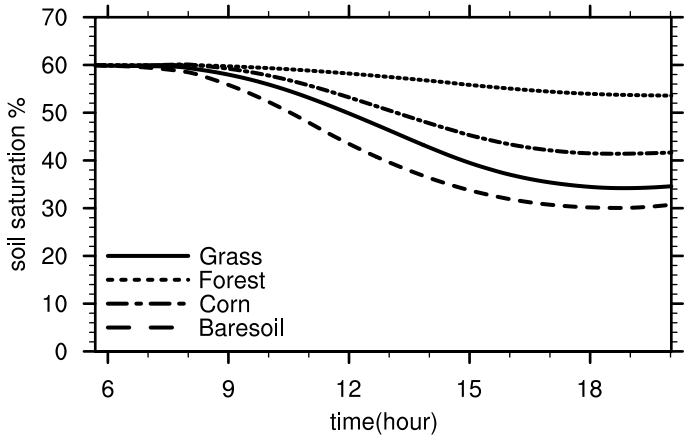

Figure 3.7 Change in the topsoil layer saturation over different land types.

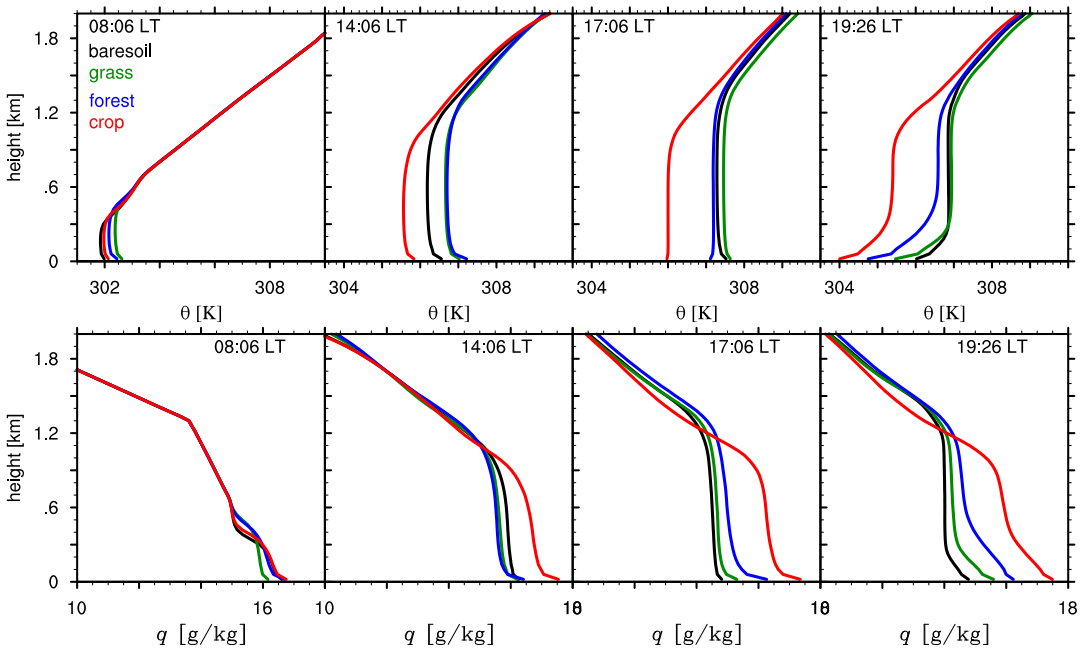

Figure 3.8 Comparisons of potential temperature (top) and specific humidity (bottom) profiles in lower atmosphere over different land types at various time of a day.

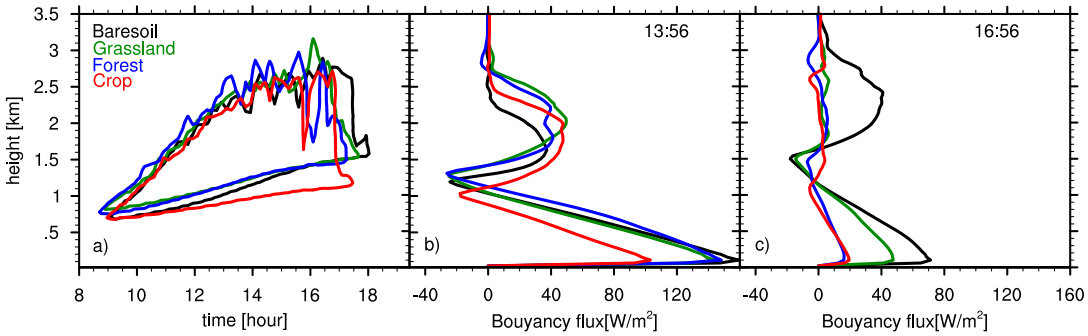

Figure 3.9 a) Evolution of cloud base and maximum cloud top height, b) buoyancy flux profiles at 1:56pm and c) at 4:56pm over various land types. Times are in local hour.

Chapter 4: Diurnal cycle of precipitation over 2D islands

4.1 Introduction

Fine resolution CRM and LES studies have provided important insights into the details of the diurnal development of convection over land, and also helped to bring improvement to convective parameterization schemes used by GCMs. However, certain issues remain unsolved. For example, why do most of inland regions have peak rainfall in the late afternoon – early evening? The question is not that trivial as most GCMs tend to simulate it around local noon when the CAPE and surface fluxes are maximum (e.g., Dai 2006). The current study aims to gain better understanding of the physical mechanisms that control the pronounced time lag between the net radiation maximum and the rainfall peak observed in nature. We explore various aspects of land convection at sub daily timescales using idealized simulations performed by the new SAM-SLM model, which explicitly resolves convective and turbulent processes as well as the interactions between the land surface and overlying PBL.

Our idealized framework consists of an island of variable size, from relatively small to almost continental scale, surrounded by an idealized ocean with prescribed SST. As the first approximation to the problem, only two-dimensional domains are considered as the fully three dimensional framework would be very expensive for prolonged cloud-resolving simulations over the domains of hundreds of kilometers across used in this study. In the future research, three-dimensional simulations will also be performed.

Convection over a sufficiently large island can be a good proxy for a continental convection. While coastal regions are largely influenced from the land-sea thermal contrast, the flat inland regions feature distinct continental convective regimes (Carbone et al., 2000), which will be the main focus of this study. Our approach will be the radiative-convective equilibrium (RCE) technique, in which the balance between the net radiative cooling and surface heat fluxes determines the atmospheric temperature profile. When using large domains, the RCE dictates the

large scale circulations that interact with the local PBL, land surface and most convective processes. In RCE, we are not forced to choose initial and lateral boundary conditions, or so-called large-scale forcing, which in fact can dictate the bulk of the solution itself. Instead, the land-atmosphere system freely evolves to find its quasi-equilibrium as the result of interactions among clouds, radiation, PBL and land surface.

In general, the RCE technique has been used quite intensively in the past to study maritime tropical atmosphere using both parameterized convection (e.g., Renno et al., 1994), and cloud-resolving models (e.g., Held et al., 1993; Tompkins and Craig, 1998; Grabowski 2006; Khairoutdinov and Emanuel, 2013). However, until recently, the RCE has not been generally applied to the convection over land. In, perhaps, one of the first studies of this kind, Cronin et al. (2014; hereafter CR14) applied RCE over an idealized island and have shown that the rainfall peaks around 6 pm with notable land-sea convective intensity contrasts. However, due to the island size limitations (less than 120 km radius), the rainfall development was characteristic of a coastal convection, and the diurnal rainfall over inland regions beyond the sea breeze penetration zone remained unexplored. Also, no actual land model was used in CR14; instead, a simple slab ocean model with a reduced heat capacity compared to the surrounding ocean was used, so no effect of vegetation and soil moisture on the diurnal cycle of precipitation could be explored.

The RCE has been considered to be a good idealization for the tropical ocean convection with the fixed SST and fixed mean insolation; the tropospheric destabilization by the large scale forcing (radiative cooling at TOA and the surface enthalpy fluxes) is offset by the stabilizing effect of the deep convection, producing relatively weak CAPE. However, the RCE method is limited in its application to interactive surface temperatures. As discussed by Pierrehumbert et al. (1995), the threshold net solar radiation at the surface to reach the RCE in the tropics is approximately 300 W/m^2. Otherwise, the runaway greenhouse effect occurs, as the increased temperature is not balanced by the OLR (outgoing longwave radiation). In the real Tropics, there is a net export of the excess energy away from tropics by the atmosphere and the ocean. In RCE over land, replacing the surrounding ocean with land and making the surface thermally interactive would result in a runaway greenhouse effect as the net absorption of solar radiation over the vegetated land is roughly 400 W/m^2, exceeding the threshold, which was confirmed by one of the initial simulations of this study (not shown here). The RCE computed over the fully interactive surface, indeed, fails to reach the unique equilibrium as was also shown by Rochetin et al. (2014). One way to resolve

this issue, which worked in our study, is to add the surrounding ocean with fixed SST, while simulating an island with the interactive surface. Another way was used by CR14 who achieved the RCE using fully interactive surface everywhere in the domain (with land approximated as a water slab with reduced depth), but with significantly adjusted insolation equivalent to 45 ˚N at the equinox (~ 310 W/m^2) which is about 160 W/m^2 lower than the values used in our study. Despite these differences, the findings of CR14 is generally similar to to our F-Sd-T25-TP case more characteristic of a coastal convection, both having the rainfall maximum at around 6 pm.

Another relevant diurnal rainfall study over thermally interactive land in midlatitudes is by Schlemmer et al. (2011). In that study, the run-away greenhouse effect is prevented by using relaxation of the domain-mean atmospheric profiles to the initial profiles above the boundary layer, as an implicit large-scale synoptic forcing. The soil profiles were also nudged toward the initial profile. Although the model-simulated diurnal convection over land in Schlemmer et al. (2011) agrees rather well with the typically observed summertime convection over Europe, the results may be sensitive to the relaxation procedure.

In this study, the following fundamental questions are addressed:

1) How does the diurnal cycle of the land rainfall respond to the SST warming, which can be viewed as a proxy for the climate warming?
2) How does the diurnal cycle of the land convection respond to added planetary rotation as a proxy for fundamental difference between tropics and midlatitudes?
3) How does the diurnal cycle of the land moist convection respond to changes in vegetation type?

This chapter is organized as follows. Section 4.2 gives details about the simulation design. Section 4.3 discusses the diurnal rainfall developments over tropical and midlatitude land, and their different responses to the climate change as represented by the SST change. Also, the coastal convection and continental convection are contrasted by comparing the small and big island simulations. Additional sensitivity of the vegetation types are also presented. Section 4.4 concludes this chapter with the summary of the findings.

4.2 Numerical set up and experiment design

Two-dimensional (2-D) SAM-SLM is used to simulate development of moist convection over islands of different sizes in the coupled land-atmosphere-ocean system using the RCE framework. The SAM-SLM model has been introduced in Chapter 3 and will not be revisited here except for details that are specific for the 2D island cases. The SAM-SLM model has been also documented in detail by Lee and Khairoutdinov (2015).

An island is placed in the center of a 2D domain with an ocean, modeled as a prescribed constant-SST surface, surrounding it. An island occupies one third of the domain. The grid spacing in all simulations was 500 m, which is rather high for cloud-resolving model simulations. Two domain sizes are used: 960 km and 5760 km, which correspond to the island sizes of 320 and 1920 km, respectively. The vertical grid has 64 vertical levels with variable resolution, gradually increasing from 50m grid spacing near the surface to 500m above 5km altitude, and the domain top being at 27 km. The time step is 10 seconds. Periodic lateral boundary conditions are used. A Newtonian damping layer is applied in the upper 30% of the domain to prevent the reflection of the gravity waves. Over the island, the SLM is used to compute the surface fluxes, while SAM's standard bulk aerodynamic formulation is used to determine the surface fluxes over the ocean. In each simulation, the SST is fixed at one of the following three values: 22, 25 and 28 ˚C, to explore the impacts of surrounding ocean's temperature on convection over land. The initial profiles of temperature and specific humidity, shown in Fig. 4.1, are obtained from the multiyear JJA season of ECMWF ERA-INTERIM reanalysis over the S.E. U.S. In practice, there is actually little dependence on specified initial profiles as each simulation has been run long enough to reach a quasi-equilibrium state. To initiate turbulence, small noise in the temperature field is introduced in a few lowest layers at the beginning of each simulation. It is well known that prolonged 2D simulations are prone to developing strong horizontal jets (Held et al 1993), which are generally considered to be an artifact of using a 2D framework. To avoid such a behavior, it is common to relax the domain mean horizontal wind at all levels to zero with 1-day relaxation time-scale.

Three types of the land surface have been used: forest, grassland, and baresoil. The external SLM parameters for each of the surface type are listed in Table 2.1. For non-vegetated land, setting LAI = 0 automatically reduces the land surface to the baresoil case. Soil is assigned to be the silt loam with 17 % sand and 13 % clay. Soil active depth is 1.5 m with 8 layers. The thickness of the top layer is 1 cm with the lower layers' thicknesses increasing exponentially with the depth. Initial soil moisture is specified to have 60 % saturation at the top and linearly increase to 100 % at the

bottom. The initial soil temperature is specified to be 18 °C for the top layer and linearly decrease to be 9 °C at 12 m depth. The bottom soil layer's temperature and moisture were relaxed to its initial value over 1 day.

A large set of simulations have been performed exploring the impact of the SST, vegetation type, landmass size and the planetary rotation on the diurnal development of continental moist convection. To distinguish the simulations, the following naming convention is used as listed in Table 4.1. For instance, Sd-F-T25-ML case stands for a simulation with a 320-km wide island (Sd) covered with a forest (F), and surrounded by the ocean with SST of 25 °C (T25) with the planetary rotation on, or for midlatitudes (ML).

Lightning frequency observations over actual islands of various sizes (Williams et al., 2004) have shown that the islands with a size smaller than about 72 km (~ 100 km^2 area) display maritime convection with suppressed lightning, while the islands larger than about 600-km size (~ 1000 km^2 area) correspond to the continental convection characterized by increased lightning activity. Therefore, the choices of the island widths (320 km and 1920 km) are expected to model different convective regimes, from coastal to inland or continental. The increase of an island width accompanies the change of the entire domain size.

The cases with and without planetary rotation represent the idealization for tropics (TP) and midlatitudes (ML). The Coriolis parameter is constant across the domain for the rotating cases and corresponds to the latitude of 32 ˚N, which approximately represents the Southeastern United States. The fundamental differences between the TP and ML cases can be demonstrated by the scaling analysis of the horizontal momentum equation as listed in Table 4.2. It is shown that the horizontal pressure gradient is approximately balanced by the Coriolis force in midlatitudes, and by the momentum advection in tropics. The pressure perturbations in midlatitudes is about 10 times larger than in the tropics, in a good agreement with the simulated results (not shown). In the midlatitudes, the Rossby radius of deformation (L_R) determines the typical scale of weather systems. The stable stratification of atmosphere tends to homogenize the pressure/density gradient induced from the small-scale disturbances ($<< L_R$), while the gradient induced by the large-scale perturbation ($>> L_R$) is a subject to the Coriolis turning. In a continuously stratified rotating fluid (ocean or atmosphere), L_R is defined by

$$L_R = \frac{NH}{f} \tag{4.1}$$

where f is the Coriolis parameter, N ($=\sqrt{\frac{g}{\theta_0}\frac{d\theta}{dz}}$) is Brunt-Väisälä frequency, which is the measure of stratification, and H is the scale height. Using the representative synoptic scale values for midlatitudes (e.g., $f \sim 10^{-4}$ s^{-1}, $N \sim 0.01$ s^{-1}, H $\sim 10^4$ m), the typical length scale L_R is approximately 1000 km. The dependence of L_R on latitude suggests that the geostrophic approximation is not valid in the equatorial regions ($f \sim 0$). For 2-D island cases, the horizontal scale of an induced heating disturbance is approximately equivalent to the length scale of the island due to the land-ocean temperature contrast. Therefore, landmass sizes in mid-latitudes that are larger than the typical Rossby radius are expected to show the pronounced atmospheric pressure gradient across the coastlines.

It takes almost a year for each simulation to reach a quasi-equilibrium, mostly because of the slow adjustment of the soil. Figure 4.2 shows the evolution of the domain-mean precipitable water and domain-mean temperature for three surface types. The composite diurnal cycles were derived by averaging the diurnal cycles of the last 100 days of each simulation.

4.3 Results

4.3.1 Large scale circulation over island

All simulations coherently exhibit the domain-wide large-scale circulation with ascent over the island and descent over cooler ocean. Clouds generally populate the ascent regions; consequently, most rainfall is over the island with the mean rate by about an order of magnitude exceeding the mean rate of the ocean (see Table 4.3). The large-scale overturning circulation greatly modifies the tropospheric moisture, with the detrainment from the convection moistening the troposphere above the island, while the subsidence greatly drying and slightly warming the troposphere over ocean (Fig. 4.3). It is interesting that the descending branch of the circulation is strong enough to form a trade inversion in the lower troposphere, where the humid and shallow maritime boundary layer seems to interface to the dry troposphere aloft. The temperature contrast between the land and ocean goes through diurnal variations, but only the PBL seems to be mostly affected by it and the troposphere above the PBL undergoes the relatively smaller change.

During daytime, the large solar radiation heating contrast between land and ocean induces general upward motion over land. On the other hand, the domain-wide, large-scale circulation is maintained and intensifies at nighttime due to positive feedback among the radiation, large-scale dynamics, water vapor and clouds as discussed by Nilsson and Emanuel (1999) and Raymond and Zeng (2000). They hypothesized that the water vapor is maintained by the detrainment from convection within ascending branch of the large-scale circulation, and in turn, the gradient of the radiative cooling, which is associated with the humidity of air and cloudiness, drives the circulation with the moist convection embedded in the ascending branch. Previous numerical studies have also found similar circulation patterns and self-aggregation of tropical deep convection over the warm regions such as the tropical Warm Pool (e.g., Grabowski et al., 2000; Grabowski and Moncrieff, 2002; Liu and Moncrieff, 2008; Bretherton et al., 2006).

Over the tropics, due to the smallness of the Coriolis parameter, any heating disturbances imposed on the atmosphere is effectively removed by convectively generated inertial-gravity waves (e.g., Bretherton and Smolarkiewicz, 1989; Mapes 1993; Grabowski et al., 2000). Conversely, in midlatitudes, this would imply that the subsidence-induced warming would be confined near the source region (the warm spots) if the horizontal scale of the perturbation is much smaller than the Rossby radius, which is typically an order of 1000 km in midlatitudes (Bretherton 1987; Liu and Moncrieff, 2004). Scaling analysis of the horizontal temperature perturbation is instructive to demonstrate the temperature gradient is much weaker in the tropics (non-rotating atmosphere) following

$$\frac{\Delta\theta}{\theta} = \frac{U^2}{gH}(tropics), \quad \frac{\Delta\theta}{\theta} = \frac{fUL}{gH}\left(midlatitudes\right) \tag{4.2}$$

Using the typical values found in Table 4.2, the temperature gradient would be on the order of 10^{-3} in the tropics, which is about 10 times smaller than in midlatitudes. Liu and Moncireff (2004) have shown that over the warm spot of ocean, the increase of Coriolis parameter to the typical midlatitudes value leads to the doubling of mid tropospheric warming, induced by subsidence near the heating perturbation, and the reduction by half in the far field in their dry atmosphere simulations. Indeed, our simulations with planetary rotation are also marked with enhanced heating and moistening within the ascent region over the island.

One can see from Fig. 4.4, that the contrast in TOA cooling, as represented by the OLR, between land and ocean is somewhat different in tropics than in midlatitudes. Overall, cooling is

the strongest over the central ocean regions in ML cases, but there is less IR cooling far away from the island where there is development of deep precipitating clouds as also indicated by the positive mean vertical velocity. The planetary rotation seems to separate the circulation into two regions: one is associated with the island, and the other being independent of the island forming a separate RCE state over the ocean. Liu and Moncrieff (2004) have also suggested that the rotational effect reduces the horizontal extent of the compensating subsidence region coupled to the deep convection over the heated area, thus promoting additional convection in far field, but inhibiting cloud development around the heating source region in midlatitudes. Similarly, in our ML cases as shown in Figure 4.4, the dry zone generated by the subsidence around the island is narrower and is drawn closer to the island. As a result, the troposphere far from the island is less influenced from the subsidence drying. Also, the outflow from the subsiding branch of the island-associated circulation tends to converge at lateral boundaries and provide the positive vertical velocity. These features seem to support a formation of deep precipitating convection over the central ocean.

Differences in circulation between the TP and ML case also have a qualitative effect on the diurnal cycle of precipitation over the island. This is illustrated by Fig. 4.5, which shows Hovmöller plots for a composite diurnal cycle of precipitation over forested small island (Sd) with and without planetary rotation, or TP vs ML. While in the TP case, the precipitation tends to start developing at the coastal regions at about 2 pm and then slowly propagates inland well into the midnight, the occurrence of rainfall in ML case tends to be centered inland from the beginning and shows the rainfall maximum at 4-6 pm, which is similar to what is observed over the East Coast of the United States. This is mostly because of dry coastal regions in the ML case, which is consistent with higher degree of localization of deep convection (see Fig. 4.4) due to tight control of the Coriolis force on the circulation's horizontal extent, and its association with the tropospheric temperature and moisture distribution.

It is also apparent in Figure 4.4 that the coastal areas in the warmer climate (higher SST) tend to become drier as the consequence of the ascending branch of the circulation becoming narrower. This is consistent with the study by Bretherton et al. (2006), who have found in their idealized CRM simulations that following SST warming, the ascending region becomes narrow with stronger convection within the large-scale circulation. This shifts the rain further away from the coastal regions inland, which tends to dry the soil and, hence, shift the balance of the surface fluxes from latent heat to sensible heat flux, which results in substantially higher maximum surface

temperature in coastal regions relative to the surrounding ocean than inland as illustrated by Fig. 4.6.

The daytime surface heating creates large temperature gradients between land and ocean in the boundary layer as shown by the buoyancy field in Fig. 4.7 at early afternoon (1:30 pm) soon after the precipitation starts. Buoyancy is defined as

$$b = \frac{\theta_v(t,x,z) - \overline{\theta_v(z)}}{\overline{\theta_v(z)}} \tag{4.3}$$

where the virtual potential temperature $\theta_v = \theta(1 + 0.608q_v - q_n - q_p)$ with the moisture content of specific humidity, cloud condensates, and precipitation water (corresponding to q_v, q_n, q_p, respectively). Overbar denotes the average taken over the x-space and time axis.

One can see a well-developed sea-breeze, drawing cooler and moist maritime air on to warm and dry island. Thus, the coastal region, in concert with the sea breeze blowing onshore, becomes a favorable location for the early development of deep precipitating clouds. In time, the sea breeze front with accompanying convection tends to move inland as shown in Fig. 4.8. This behavior is consistent with observations. For example, using TRMM data, Kikuchi and Wang (2008) found an emergence of precipitation anomaly right near the coastlines, which, subsequently, amplifies and moves inland to finally dissipate by midnight. In their analysis, a maximum rainfall at 6 pm local time, similar to our results (Fig.4.5a), is found for Central America, North Western part of America, Western Africa and Madagascar.

Interestingly, there seems to be a secondary maximum of precipitation in the center of the island after the midnight (Fig. 4.5a). This is consistent with the study by Gray and Jacobson (1977) who found the secondary early morning precipitation maximum over relatively large islands in the tropics from the station observations, and they hypothesized that the large scale circulation induced from radiative cooling gradient between the cloudy and clear-sky regions was the cause of the predawn rainfall maxima. However, Dudhia (1989) and Liu and Moncrieff (1998) found the direct radiation-cloud feedback (IR cooling at cloud top and warming near cloud base) as being relatively more conducive to the nocturnal-early morning rainfall maximum. Observations over the Amazon basin have also shown that some stratiform clouds redevelop overnight producing secondary nighttime rainfall peak due to the strong radiative cooling at cloud top and warming below, destabilizing the cloud layer (Lin et al., 2000). Figure 4.9 compares the vertical profiles of water vapor, cloud water, radiative heating anomaly and wind flow at midnight. One can see that over

the island, the IR cooling is pronounced over the stratiform cloud tops where the absorption dominates at the cloud base and near surface from the high concentration of water vapor. This seems to be indeed destabilizing the troposphere over the island and prepare it for a late night-early morning convection. Also, the aforementioned positive feedback among convection, radiation and large-scale circulation is well illustrated in Figure 4.9.

So far, the characteristics of convection over a small island have been discussed. The tropical big island cases (Bd-F-TP) shows that the convection, after its initiation over the warm spot, mostly develops into organized mesoscale convective systems that can persist longer than 24 hours and actually can cross the whole island from one coast to another as shown in Fig. 4.10, similar to the study of Liu and Moncrieff (2008). As those systems are responsible for most of the precipitation in this case and the diurnal signal of precipitation is not as well defined as over the smaller island, we mostly concentrate on the smaller island cases for discussion of the diurnal cycle of precipitation.

4.3.2 Sensitivity to SST

Under the weak-temperature-gradient conditions over the tropics, moisture becomes the key factor that governs the development of convection. Convection can be suppressed by the enhanced entrainment of the dry environmental air in free troposphere; therefore, the drier the environment, the less buoyant the rising air parcel becomes, which is detrimental to development of convection (e.g., Derbyshire et al., 2004; Wu et al., 2009). Our simulations also support this mid-tropospheric moisture - convection feedback as demonstrated by Fig. 4.11, which shows the correlation between the mid-tropospheric humidity and vertical velocity at 500 mb. As shown in Figure 4.12, the descending branch of T22 (zone of troposphere with very dry air) is located further off the island, and the humidity field stays favorable for the deep convection near the coastlines. As the result, the T22 case has earlier initiation of rainfall with a relatively relaxed distribution in comparison to warmer SST cases. Over warmer ocean, the influx of dry subsiding air into the upper and middle troposphere over island amplifies. As a result, entrainment of dry free tropospheric air into the rising plume leads to the loss of buoyancy preventing the subsequent development of deep convection over the warmest spots near the coastlines.

Figure 4.13 shows the diurnal cycle of rainfall spatially averaged over 40-km wide blocks starting from the coast toward the islands' center. The diurnal cycle is averaged separately for each block. One can see that (compare to Fig. 4.5) the rain is clearly propagating inland in TP cases as the precipitation peak is shifting to the later time, which is not seen in the ML cases where the diurnal characteristic seems to be more local with the peak at about the same time. One important feature is that the time of precipitation maximum in ML cases seems to clearly be shifting to earlier time as the SST increases, especially deep inland. The shift of the diurnal phase of the rainfall in response to SST change is not as clear in the TP cases.

The rainfall rate is generally higher in T28 cases (especially in the block well away from the dry coastal zone), which is consistent with the study by Bretherton et al. (2006) of idealized Walker circulation. A theoretical explanation has been suggested based on energy and moisture budget. The radiative cooling and surface fluxes both increase following the increase of SST, but the former increases more due to the strong greenhouse effect of water vapor, hence the troposphere becomes unstable potentially producing stronger convection. Their conclusion is drawn from the time-mean perspectives and it holds quite well for the diurnal 2D island experiments herein. In the warmer climate following the increase of SST, the horizontal radiative cooling difference becomes sharper between ocean and land, and the land surface heat fluxes and gustiness locally increase in the convective regions; therefore, at equilibrium, the stronger large-scale circulation is maintained, which favors stronger convection. As was shown in Fig. 4.7 and figure 4.8, the T28 case seems to produce stronger low-level onshore flow, which increases precipitation.

The time-and-space-averaged changes of the vertical tropospheric structure in response to the SST change generally compare well to some of the other studies of the climate warming feedback. For instance, Figure 4.14 shows an overall upward shift of temperature, clouds and vertical velocity profiles following SST warming, which are broadly consistent with other modeling studies (e.g., Singh and O'Gorman, 2012, Khairoutdinov and Emanuel, 2013). Some cloud-resolving simulations of the tropical atmosphere at RCE have also shown that atmospheric warming induces more vigorous precipitation extremes (Mueller et al., 2011; Romps et al., 2011).

As mentioned above, the phase of the diurnal cycle of rainfall over the island seems to be sensitive to ocean warming, especially in the ML cases. As the SST warms, the atmospheric temperature and moisture contents also increase, which acts to increase convective available

potential energy (CAPE) under weak large scale forcing (Zhang, 2002). This is consistent with our results shown in Fig. 4.15 for different cases. However, it is the surface fluxes that erode shallow stable nocturnal boundary layer, hence reducing CIN before the onset of convection (Raymond, 1995). As shown in Figure 4.15, increased moistening of the PBL by the enhanced morning surface evaporation at warmer climate makes CIN to reach minimum earlier in ML, which, most likely, is responsible for the earlier onset of deep convection and the earlier precipitation peak in warmer SST cases. So, despite the lack of inland propagation in the ML case, the timing of the 'local' peak of precipitation seems to be determined by the temperature of the ocean several hundred kilometers away. Also, note that despite substantial shift of the timing of maximum precipitation, there is relatively little change in the diurnal cycle of the surface fluxes (Fig. 4.16).

It is interesting to note that clouds (see Figure 4.17) seem to regenerate at night in the low troposphere following the development of the nocturnal PBL. This tends to reduce the net radiation and overall surface heat fluxes in the following morning as the solar radiation is largely blocked by the clouds, which is consistent with the results by Schlemmer et al., (2011). Conversely, the enhanced evaporation and faster reduction of CIN in the morning in warmer SST cases can be accounted for by the smallest amount of these nocturnal clouds. Anber et al. (2015) also highlighted the importance of the morning fog layer in delaying the precipitation maximum in the Amazon wet season via cloud-radiation feedback. Consistent with their finding, the simulated morning fog over the small midlatitude islands subsides as the SST increases due to the reduced near surface humidity and radiative cooling (Figure 4.17). As a result, more shortwave radiation reaches the land surface in the morning, and enhanced surface evaporation tends to moisten the PBL contributing to the quick transition from shallow to deep convection.

The onset of shallow convection in the morning over a flat surface follows the mechanism by which the subsequent deep convective regime develops (e.g., Tompkins 2001; Kuang and Bretherton 2006; Khairoutdinov and Randall 2006). According to this mechanism, clouds that are growing directly from PBL eddies generated by the surface heating are generally too small to produce deep clouds as the entrainment in lower troposphere quickly dilutes them. However, the precipitation showers and associated spreading cold pools can create localized regions of high moist-static energy and surface convergence that can be conducive to producing larger thermal that can give rise to taller clouds. These clouds in turn produce even stronger cold pools and bigger clouds. This positive feedback mechanism can eventually give rise to deep convection. The

existence of this mechanism in the island simulations and the effect of warmer SST is illustrated in Fig. 4.18 and Fig. 4.19. One can see that the earlier onset of convection in the morning in the warmer climate speeds up the transition process, so by 10:00 there are already showers at warmer SST, which eventually lead to faster development of deep clouds in late afternoon. This earlier shallow-to-deep convective regime transition is consistent with the shift of the precipitation peak to the earlier time. Also, higher moisture level in lower troposphere in warmer case can also be favorable to developing deeper clouds earlier. After peak precipitation is reached, the deep convection cannot be sustained as the convective downdrafts and associated evaporative cooling consumes sub-cloud moist instability available for convection (e.g., Sherwood, 2004; Done et al., 2006), which is represented by the reduction of CAPE and increase of CIN in the afternoon as illustrated in Fig. 4.15. In addition, the shading under the spreading anvils reduces incoming solar radiation, which can reduce the equivalent potential temperature (Findell and Eltahr, 2003).

4.3.2 Sensitivity to vegetation type

The effect of different land cover types, such as forest, grassland and baresoil on the diurnal cycle of the idealized islands has also been tested. Overall, the effect is not that large, despite several interesting and subtle differences. The biggest distinction is associated with using the forest as the surface type, which has a relatively large effect on partitioning the surface heat fluxes into latent and sensible as shown by Fig. 4.20. The forested land clearly has a higher evaporation rate than other surface types, while not affecting much the total precipitation in the case of smaller island. This can be explained by the fact that the forest has the higher potential to evaporate moisture into the overlying atmosphere from the water stored on the foliage.

The sensitivity of diurnal development of rainfall on the vegetation types is most significant over the bigger island (Fig 4.20, right panels). Apparently, only the forest has a well-defined diurnal cycle of the rainfall with the maximum around 4-5 pm. Grass-covered or non-vegetated land seems to lose the diurnal characteristics of moist convection development, even with the strong diurnal surface forcing. This is because the precipitation over the island in those cases are mostly dominated by the mesoscale convective systems with life-span much longer than 24 hours. The Hovmöller plots in Fig. 4.21 show the precipitation evolution for the forest and grasslands. Over the forest, there is still a strong diurnal cycle of the rainfall, with convective systems

originating closer to the coast, and then propagating deeper inland. However, over grasslands, the rainfall frequency does not follow the diurnal cycle, as the convective systems can survive longer than 24 hours once formed. Some insight into the reasons for such a qualitative difference between these cases can be related to the different tropospheric moisture. Figure 4.22 compares the diurnal variation of the relative humidity profiles for different vegetation types over the interior region of the big island. One can see that below 2.5 km, the troposphere tends to be significantly dryer over grassland and baresoil compared to the forest, while the opposite is true for the troposphere above 2.5 km. The main reason for a moister PBL over the deciduous broadleaf forest is higher evaporation rates. The dryness of the PBL over grassland and baresoil makes it very difficult for the deep convection to develop in response to diurnal variation of the surface fluxes as it takes some time to build the instability by accumulation of moisture. However, after the deep convection is started over grassland or baresoil, the more humid environment of the middle troposphere and dryer PBL actually favors the propagation of the organized convection. As shown in Matsui et al. (2010), the timing of precipitation peak over land has a geographical distribution, which is also linked to the ecosystem variation. A clear diurnal cycle presents mostly over the forested area (Eastern U.S.), and is lacking over the grassland/semi-desert area (the western Rocky regions). A similar geographical pattern in the afternoon precipitation with respect to the local evapotranspiration is presented by Findell et al. (2011). Their analysis showed that the higher evapotranspiration leads to the higher probability for the afternoon precipitation particularly in the eastern U.S. and Mexico. Consistent with these independent studies, the simulated grassland and baresoil islands show a weak diurnal rainfall amplitude with a notably dry low troposphere, while the forested island shows a well-defined diurnal cycle of rainfall due to the sufficient PBL moistening by the evapotranspiration. This qualitatively different behavior of diurnal cycle of precipitation over inland regions that we see in our idealized simulations can also be an illustration of the impact that deforestation of large regions can have on local climate.

4.4 Conclusions

This chapter presents the results of idealized cloud resolving RCE simulations of the summertime convection over an island of different sizes with an emphasis on the continental convective regime. The new SAM-SLM model was applied to a 2D case of an island of two sizes,

320 and 1920 km, surrounded by an ocean using 500 m horizontal grid spacing and land surface of three different types, baresoil, grassland, and forest. To study the effect of 'climate warming' on diurnal cycle over land, different SST for the surrounding ocean, 22, 25 and 28˚C, has been used. The RCE framework has been used to exclude the effect of prescribing forcing and lateral boundary conditions on the results. The ocean with fixed SST allows one to keep the RCE over land from developing a runaway greenhouse effect. The effect of SST on inland diurnal cycle can also be explored. Turning on and off the planetary rotation by setting the latitude to 0 ˚N or 32 ˚N allowed us to study to the first order the differences of diurnal cycle in tropics and midlatitudes. The Rossby radius of deformation defines the horizontal scales over which the heating perturbations are trapped instead of spreading away by the gravity waves. The simulations have been run for hundreds of days to reach the quasi equilibrium on time scales longer than a day, so that a similar cycle of moist convection is repeated daily following the same diurnal insolation cycle. The computational expense of such runs can explain why only a 2D framework has been used so far.

The main goal of this idealized study was to evaluate the impacts of SST, planetary rotation, and vegetation types on the diurnal cycle of precipitation over land with a focus on the timing of rainfall maximum. Relatively large islands have been chosen to look at the diurnal cycle in landlocked regions, that is fairly far from the coastal regions where the see-breeze influence can be large. All simulations develop convectively coupled large-scale circulation with an ascending branch over the island and the compensating subsidence over the surrounding ocean, which is driven by the radiative cooling difference between the cloudy (less cooling) troposphere over the island and clear (more cooling) skies over the ocean. Thus, the thermally induced large-scale circulation is characterized by mean ascent driven by precipitating convection over the island. At mesoscales, the differential heating between land and ocean generates sea-breeze circulations near the coastlines, with the boundary layer depth limiting its vertical extent; however, the see-breeze becomes the primary factor for triggering the convection and subsequent propagation in some of the cases, in particular, in the tropical (no rotation) cases.

One persistent difference between the idealized tropics and midlatitude simulations is that the horizontal extent of the rising branch of the large-scale circulation is narrower in midlatitudes because the planetary rotation limits the spreading of perturbation. As the result, the subsiding branch of the circulation tend to dry out the the coastal regions and the formation of deep

convection is generally localized in the central island regions in midlatitude cases. Overall, the model has been able to reproduce the observed time of the precipitation maximum at about 5 pm. The delayed response of the precipitation to the local surface fluxes, which tends to maximize around local noon, has been explained by the gradual shallow-to-cumulus transition over uniform land. The clouds growing directly from the PBL eddies are too small to survive the entrainment of dry mid-tropospheric air so an aggregation mechanism based on the cold-pool dynamics is necessary to produce large precipitating clouds. In the tropics cases, due to wider ascending branch of circulation, the coastal regions tend not to dry out much, so the initiation of convection occurs over the see-breeze region with the subsequent propagation inland and precipitation peak at about 6 pm. This behavior is consistent with tropical island observations (initiation over sea breeze front, penetration inland, possible merger with the rainfall amplification, dissipation in the evening).

One of rather unexpected and original findings of this study is that the change of SST of the surrounding ocean can shift the timing of the precipitation maximum over regions well removed from the sea-breeze zone. In particular, the precipitation tends to peak earlier in the case of warmer SST. This was explained by earlier onset of the shallow clouds due to warmer and more humid conditions in the morning in warmer SST cases. The earlier triggering of convection, and earlier build up of CAPE, allow the shallow-to-deep convection to be progressing earlier in the warmer climate, which manifests itself in earlier precipitation peak.

The diurnal convection over a big island in midlatitudes was found to be quite sensitive to the vegetation type in terms of evaporation-precipitation feedback. While the net radiation at the surface is rather insensitive to land type, the forest tends to produce higher evapotranspiration flux than the baresoil and grasslands. While this hardly affects the diurnal cycle of precipitation over the small island, there is considerable effect on the convection over the large island. In particular, the clear diurnal cycle of precipitation manifests itself only over forest land, while the convection tends to organize into long-lived systems over the baresoil and grassland. We found that higher evapotranspiration over forest land leads to a considerably more humid PBL and troposphere immediately above it, but dries out the mid and upper troposphere because of more frequent deep convection over the forest. Drier PBL (stronger cold pools) and more humid mid troposphere over the baresoil and grassland create conditions for long-lived convective systems that propagate across the big island with a cycle longer than 24 hours. This result from a highly idealized

simulation can support a notion that deforestation of continents can considerably affect the precipitation patterns and ultimately the local climates.

Tropical convection is often a part of large–scale circulation observed in nature; for example, the ascending branch over the Western Pacific Warm Pool (Grabowski et al., 2000; Liu and Moncrieff, 2004). Thermally induced mesoscale circulations have been known and studied extensively to affect the development of moist convection over land (e.g., Chen and Avissar, 1994; Avissar and Schmidt, 1998; Pielke, 2001; Patton et al., 2005; Courault et al., 2007; Taylor et al., 2007, 2013; Huang and Margulis, 2009, 2013; Huang et al., 2011; Kang et al., 2012; Rieck et al., 2014; Wu et al., 2015). For instance, topography contrasts such as mountain-valley regions, soil moisture gradients, sharp changes in vegetation type, location of urban area have known to trigger the sea-breeze like circulations from the daytime differential heating and subsequent gradients in the sensible and latent heating of PBL from the land surfaces. Thus, the investigation of diurnal rainfall development over landmasses with idealized frameworks like the one used in this study can potentially provide insights into the continental convection regime in a real world.

Tables

Table 4.3. Notation of experiment numerical setup descriptions.

Definition	Notation (Value)		
Horizontal domain width (km)	Sd (960)	Bd (5760)	
Vegetation types	F (forest)	G (grasslands)	B (non-vegetated)
Sea surface temperature (SST; °C)	T22 (22)	T25 (25)	T28 (28)
Latitude (°N)	ML (32)	TP (0)	

Table 4.4. Scale analysis of the equation of motion for the midlatitudes and near the Equator.

Equation of Motion	$\frac{\partial \vec{u}}{\partial t} + (\vec{u} \cdot \nabla)\vec{u} + \vec{w}\frac{\partial \vec{u}}{\partial z} = -\frac{1}{\rho}\nabla \vec{p} - f\vec{k} \times \vec{u}$
Basic Scales	$\frac{U^2}{L}$ $U \cdot \frac{U}{L}$ $W \cdot \frac{U}{H}$ $\frac{\Delta p}{\rho L}$ fU
Midlatitudes	10^{-4} 10^{-4} 10^{-5} $\frac{\Delta p}{\rho L}$ 10^{-3}
Near Equator	10^{-4} 10^{-4} 10^{-5} $\frac{\Delta p}{\rho L}$

Basic scales	Horizontal velocity, U [m/s]	Vertical velocity, W [m/s]	Length, L [m]	Height, H [m]	Coriolis parameter, f (1/s)
Midlatitudes	10	10^{-2}	10^6	10^4	10^{-4}
Near equator					~ 0

Table 4.3. Time-mean properties of atmospheric moisture, clouds and radiation fields, averaged over land and ocean separately for Sd-F-TP cases. Radiation flux divergence is defined to be the top of atmosphere (TOA) – surface radiation, where the negative represents cooling.

Variables \ SST		22	25	28
Vertically integrated water vapor (mm)	Land	31.85	46.48	61.59
	Ocean	13.05	17.12	20.92
	Domain mean	19.31	26.89	34.45
Precipitation (mm/d)	Land	8.44	9.8	10.8
	Ocean	0.16	0.11	0.06
	Domain mean	2.92	3.3	3.6
Cloud frequency (%)	Land	68.6	62.9	61.1
	Ocean	29.9	26.3	13.4
	Domain mean	42.8	38.5	29.3
Shortwave radiation flux divergence (W/m2)	Land	110.4	113.8	118.4
	Ocean	83.5	87.7	89.7
	Domain mean	92.4	96.4	99.3
Longwave radiation flux divergence (W/m2)	Land	-188.2	-196.1	-211.3
	Ocean	-203.4	-218.1	-219.0
	Domain mean	-198.3	-210.8	-216.5
Total surface heat flux [W/m2]	Land	122.6	145.4	146.3
	Ocean	101.6	102.9	105.9
	Domain mean	108.6	117.1	119.3

Figures

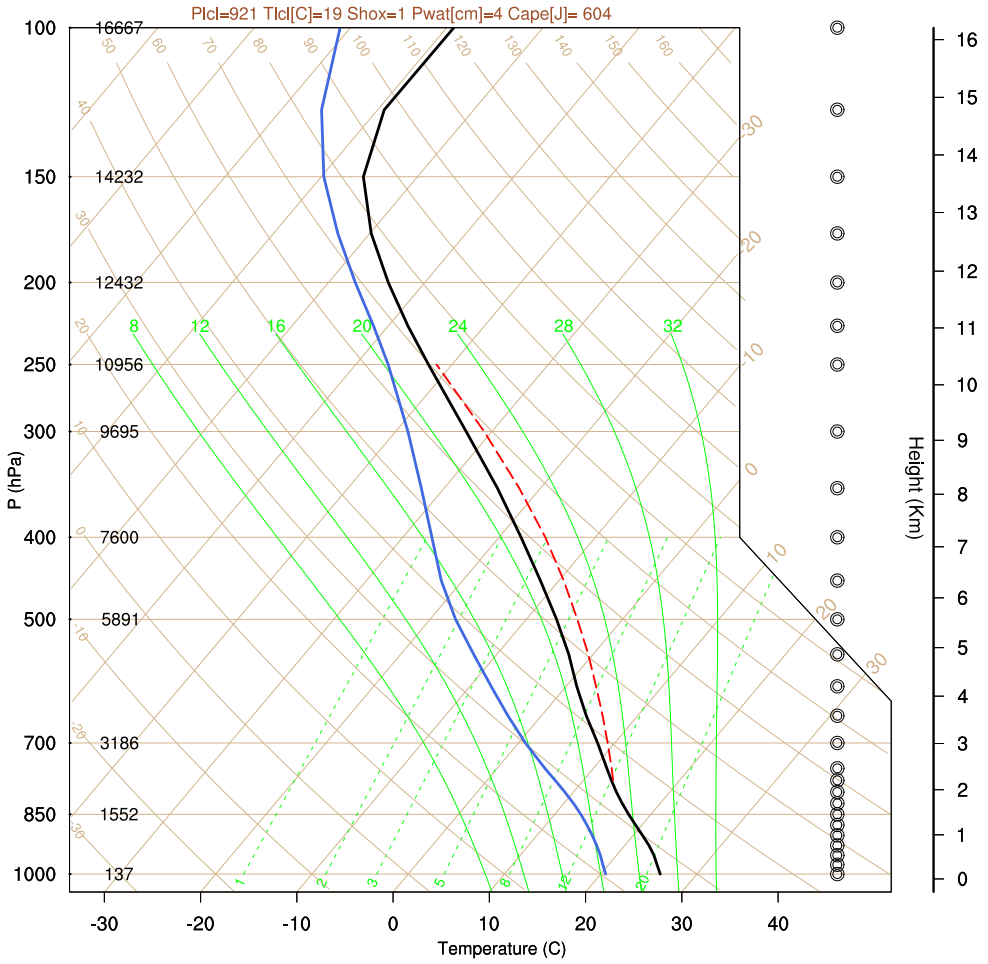

Figure 4.1 Initial sounding averaged over the South East U.S. (30-35N, 80-85W) for July of 2000-2010 of ECMWF ERA-INTERIM reanalysis data. Black line is the sounding, blue line is dew point temperature, and red represents the CAPE when the surface air parcel is lifted to saturation.

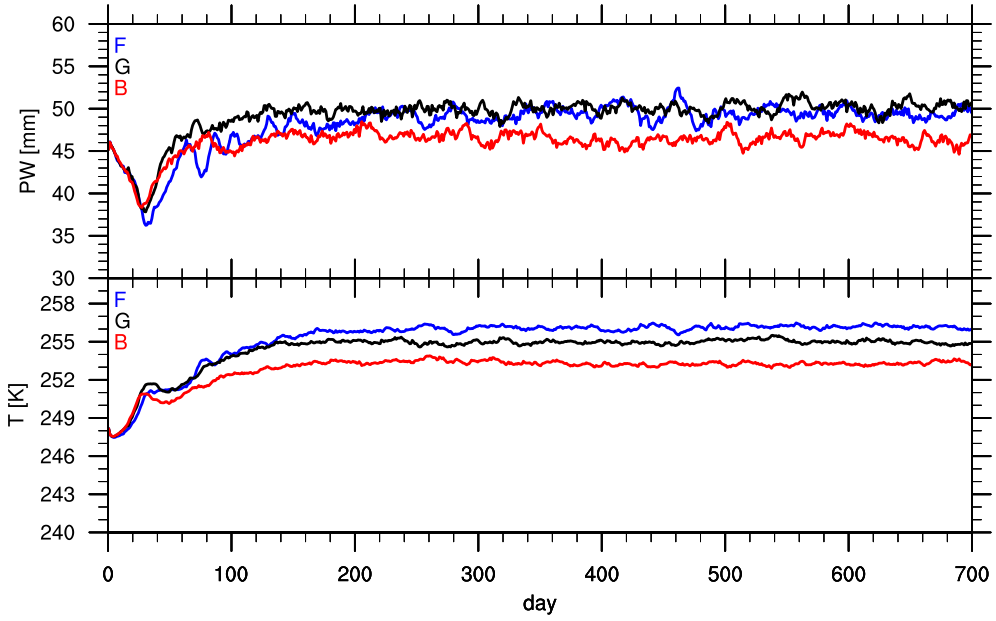

Figure 4.2 (Top) Mean precipitable water (vertically integrated water vapor) and (bottom) domain mean hourly temperature from Bd-T25-ML cases with varying vegetation types: (blue) forest, (black) grassland, (red) baresoil.

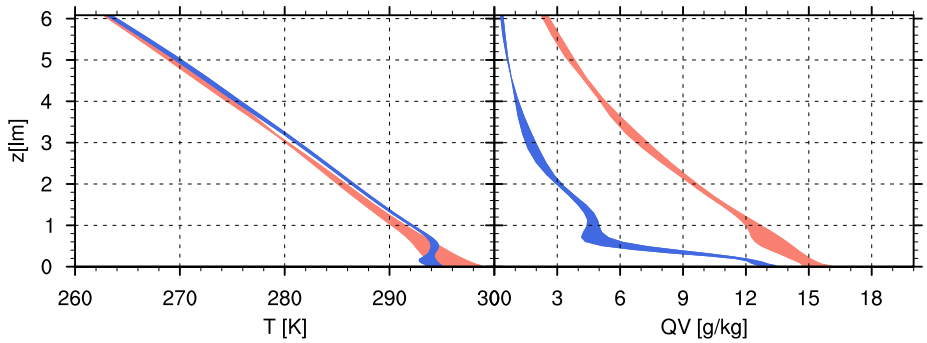

Figure 4.3 Diurnal variation of temperature and specific humidity averaged over island (red shading) and ocean (blue shading), for Sd-F-T25-TP case.

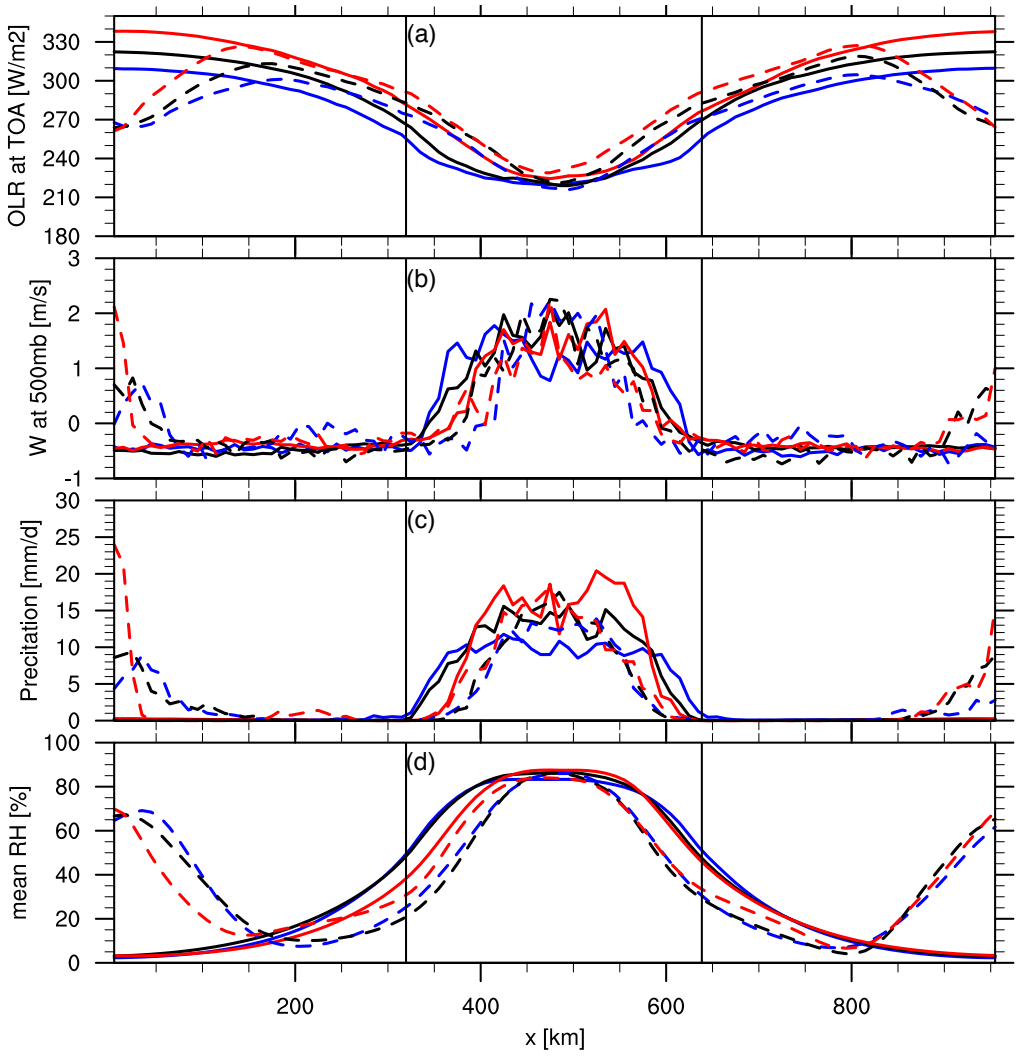

Figure 4.4 Time mean spatial variation of (a) Outgoing longwave radiation (OLR) at top of atmosphere (TOA), (b) vertical velocity at 500mb, (c) surface precipitation rate and (d) mid level relative humidity averaged between 750 – 500 mb. Colors represent prescribed sea surface temperature (SST) at 22 (blue), 25(black) and 28 ˚C (red). The solid lines are for tropics, and dashed lines are for midlatitude simulations. Black vertical lines represent the island boundaries.

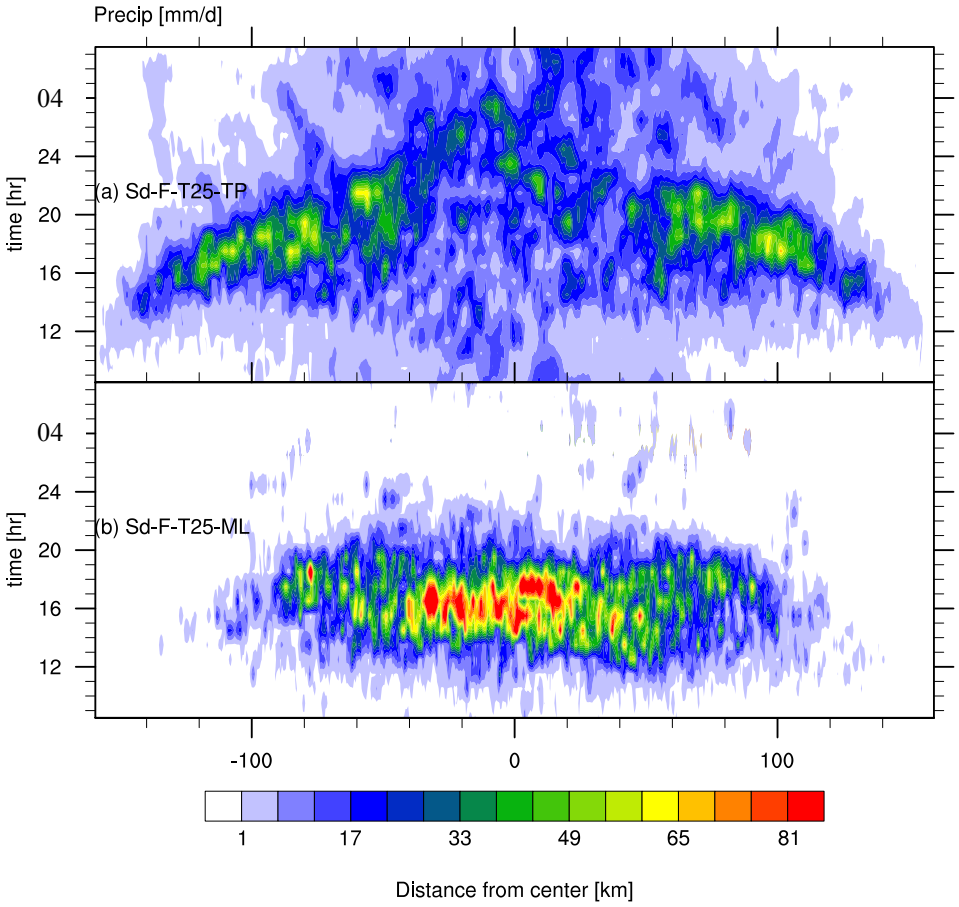

Figure 4.5 Hovmöller diagrams of diurnal rainfall over the island domain, for (a) Sd-F-T25-TP and (b) Sd-F-T25-ML cases. The time axis starts in the morning and progresses into the following morning.

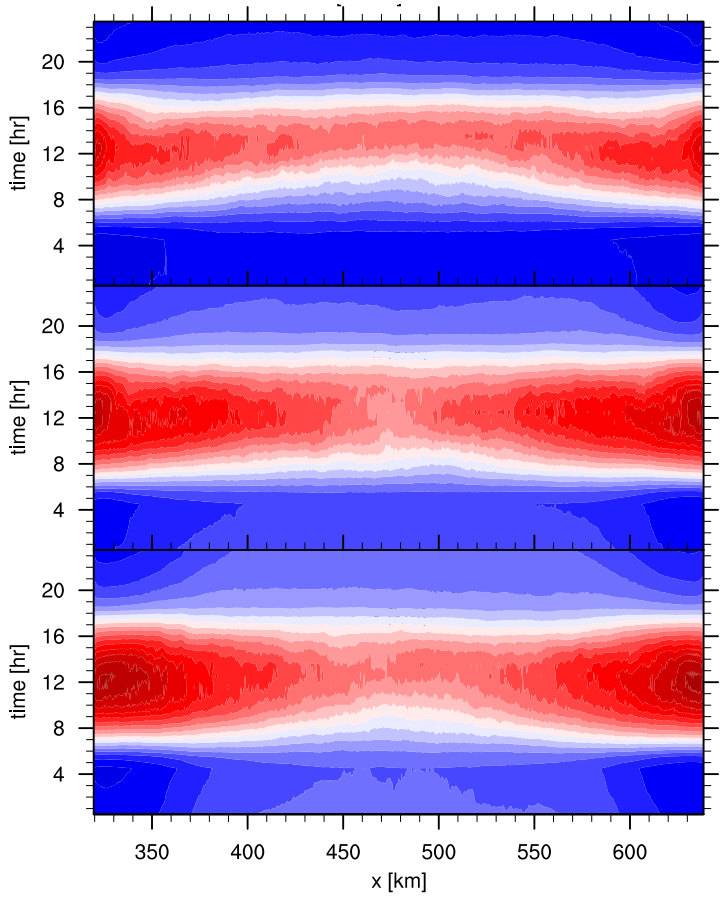

Figure 4.6 Hovmöller diagram of surface temperature contrast between islands and ocean. Only the island domain is plotted with blue regions represent the colder land surface at night, and red for the warmer surface during daytime. From top to bottom, Sd-F-T22-TP, Sd-F-T25-TP and Sd-F-T28-TP are presented.

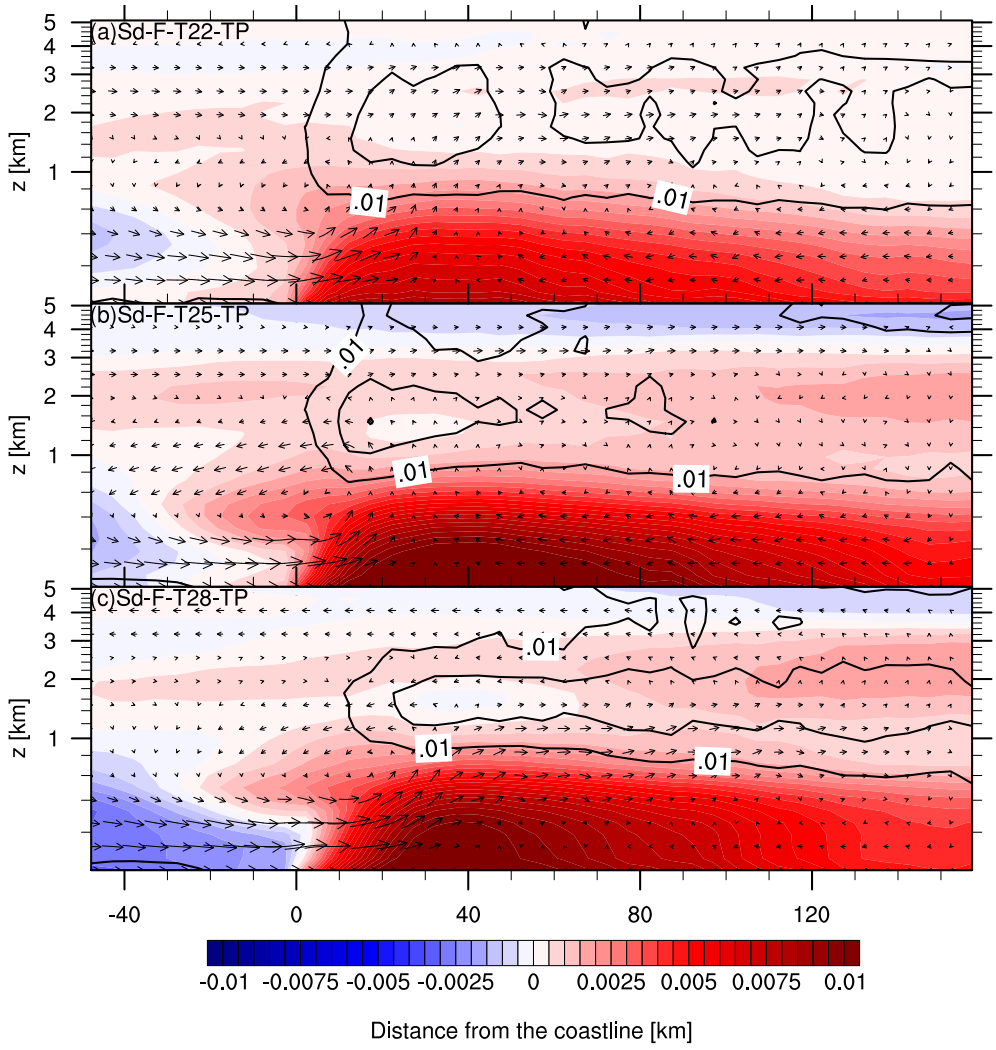

Figure 4.7 Vertical cross-section of buoyancy field (color shading), winds (vector) and line contour of cloud condensates for 0.01 and 0.05 g/kg taken at 13:30pm.

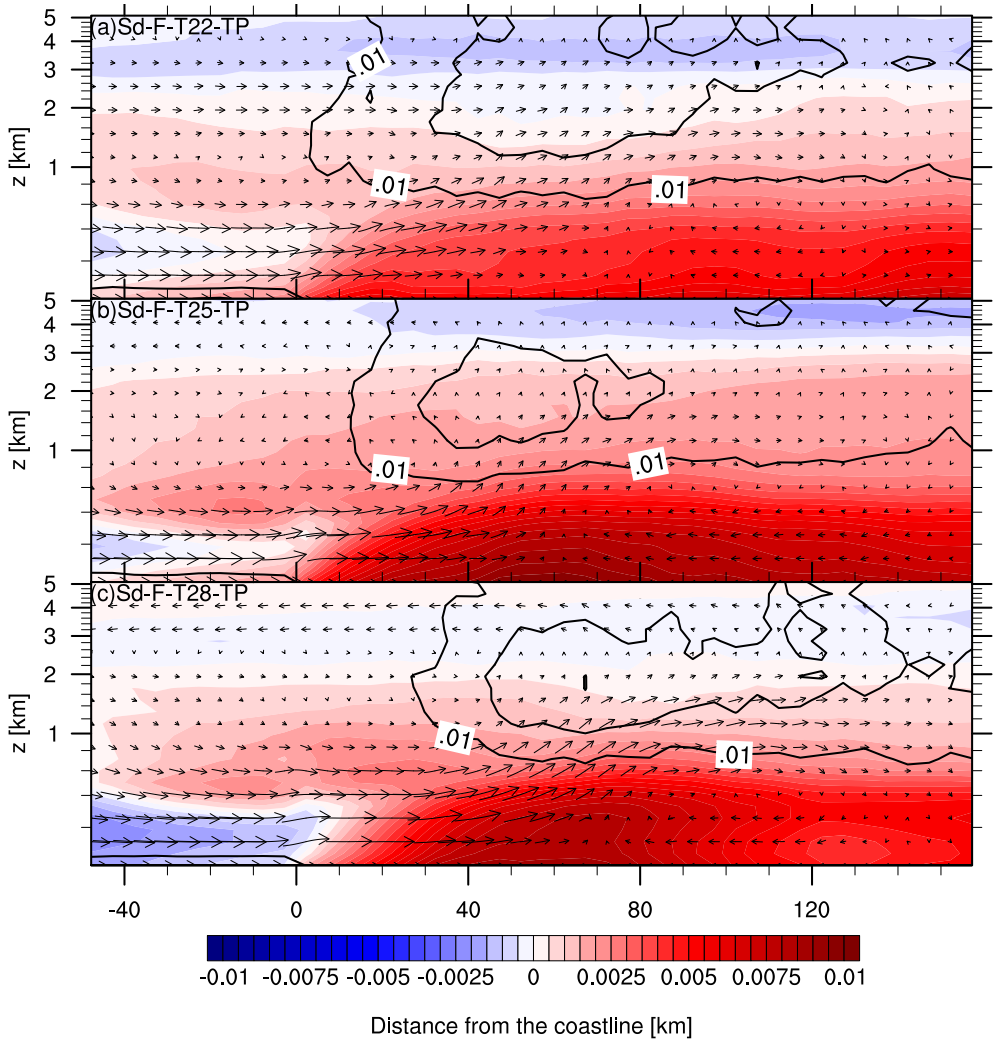

Figure 4.8 Same as Figure 4.7, but at 16:30.

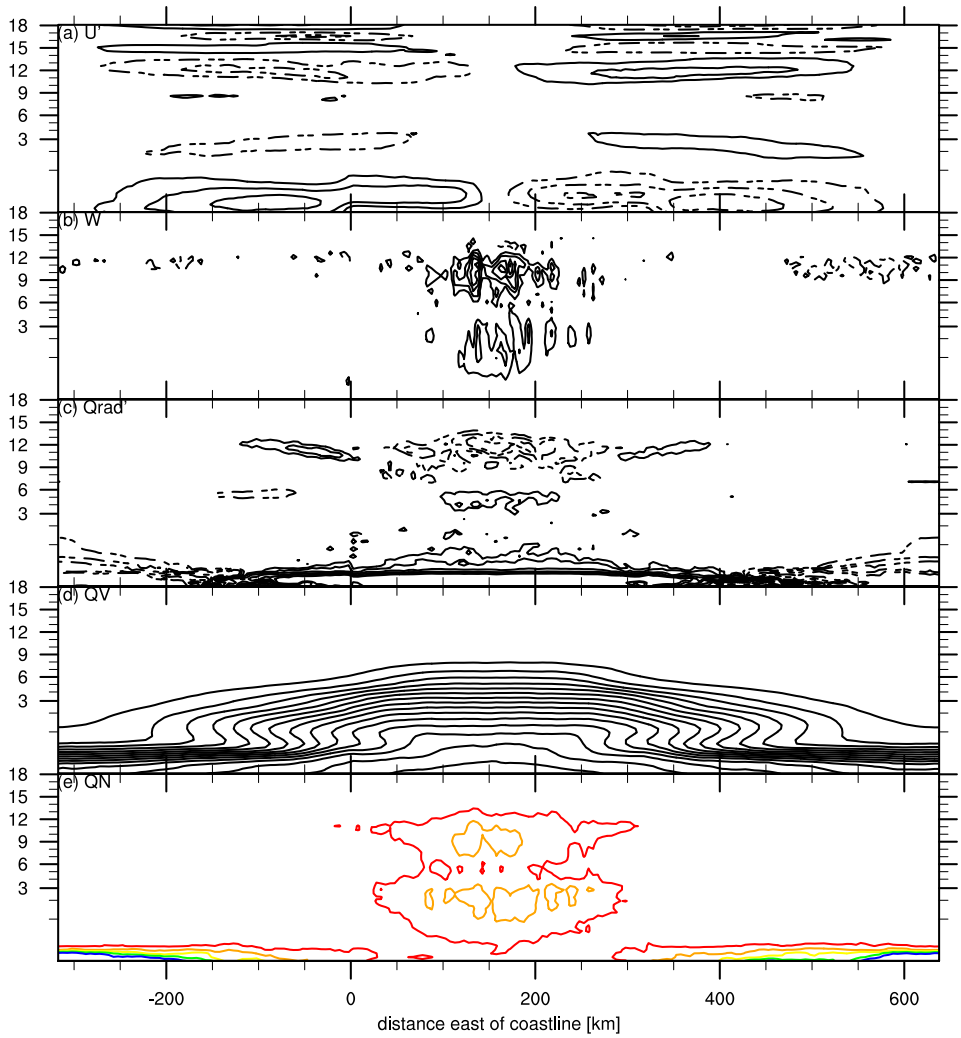

Figure 4.9 Vertical cross-section of (a) zonal wind anomaly, U' (m/s), (b) vertical velocity, W (cm/s), (c) radiative heating anomaly, Qrad' (K/d), (d) water vapor, QV (g/kg) and (e) cloud condensate, QN (g/kg) for Sd-F-T25-TP case at midnight. Anomalies are from the diurnal mean composite statistics. Negative anomaly is contoured in a dashed line. Contour level in QV figure is 1g/kg, and QN is contoured at 0.01 (red), 0.05 (orange), 0.1 (yellow), 0.15 (green), 0.2 (blue), 0.4 (navy) g/kg.

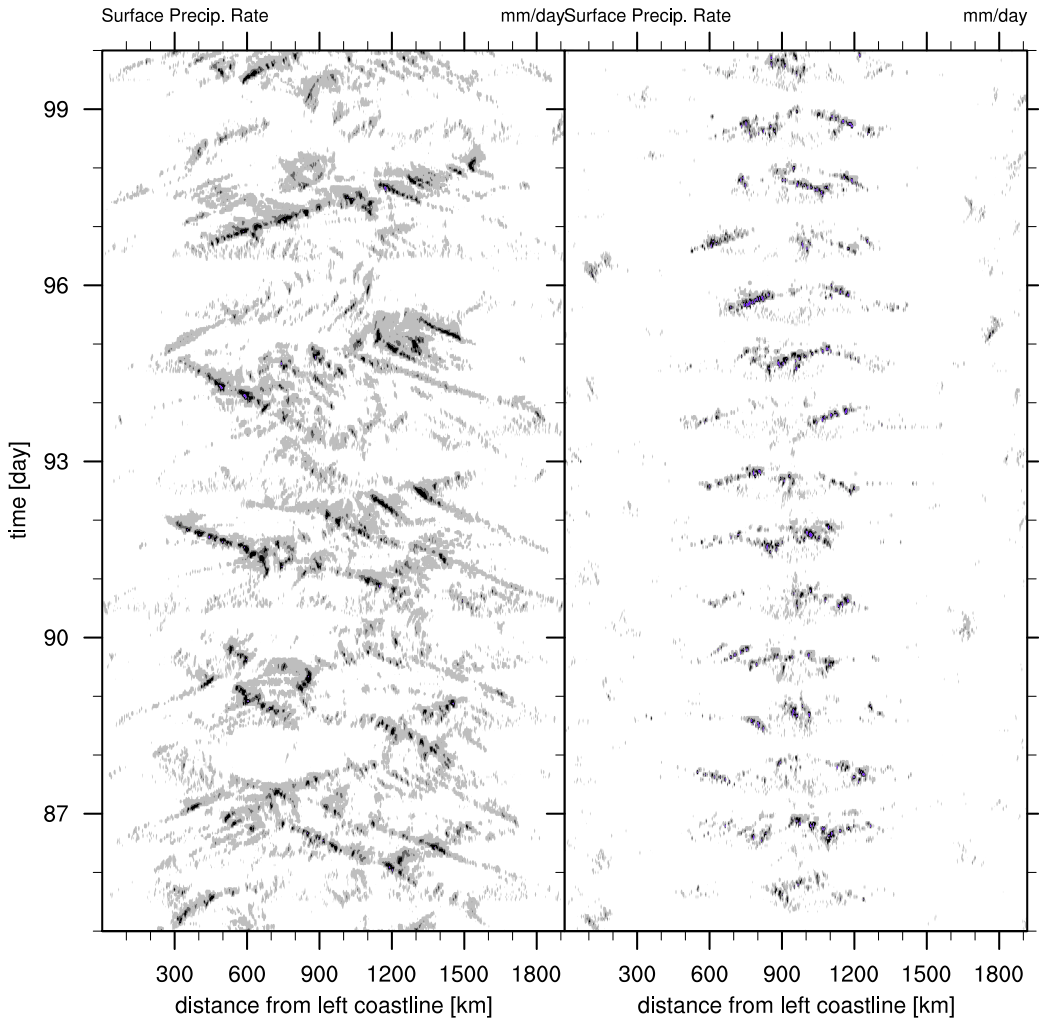

Figure 4.10 Hovmöller diagrams of surface precipitation from (left) Bd-F-T25-TP and (right) Bd-F-T25-ML.

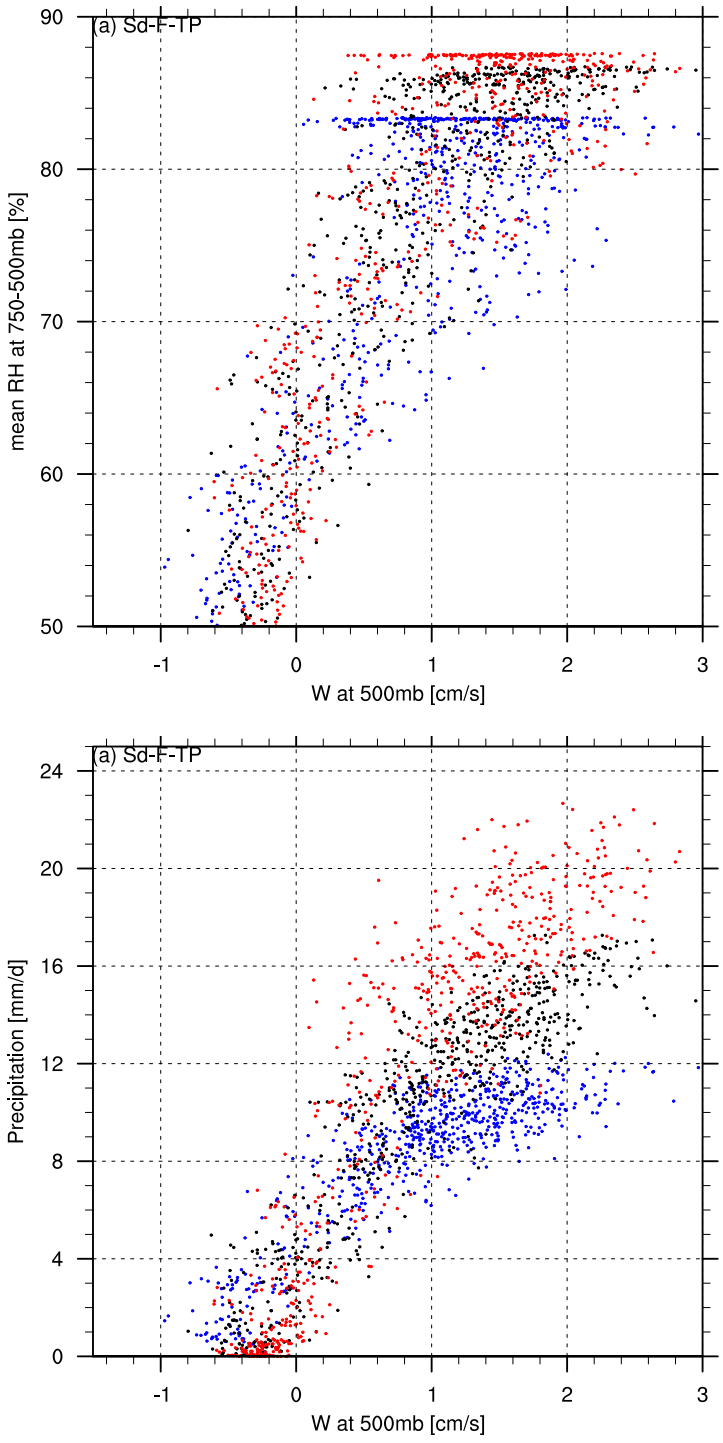

Figure 4.11. Scatter plot of (top) vertical velocity at 500mb and relative humidity averaged between 750-500mb, and (bottom) vertical velocity at 500mb and surface precipitation, for Sd-F-TP cases. Color represents prescribed SST: 22 (blue), 25 (black) and 28 ˚C (red).

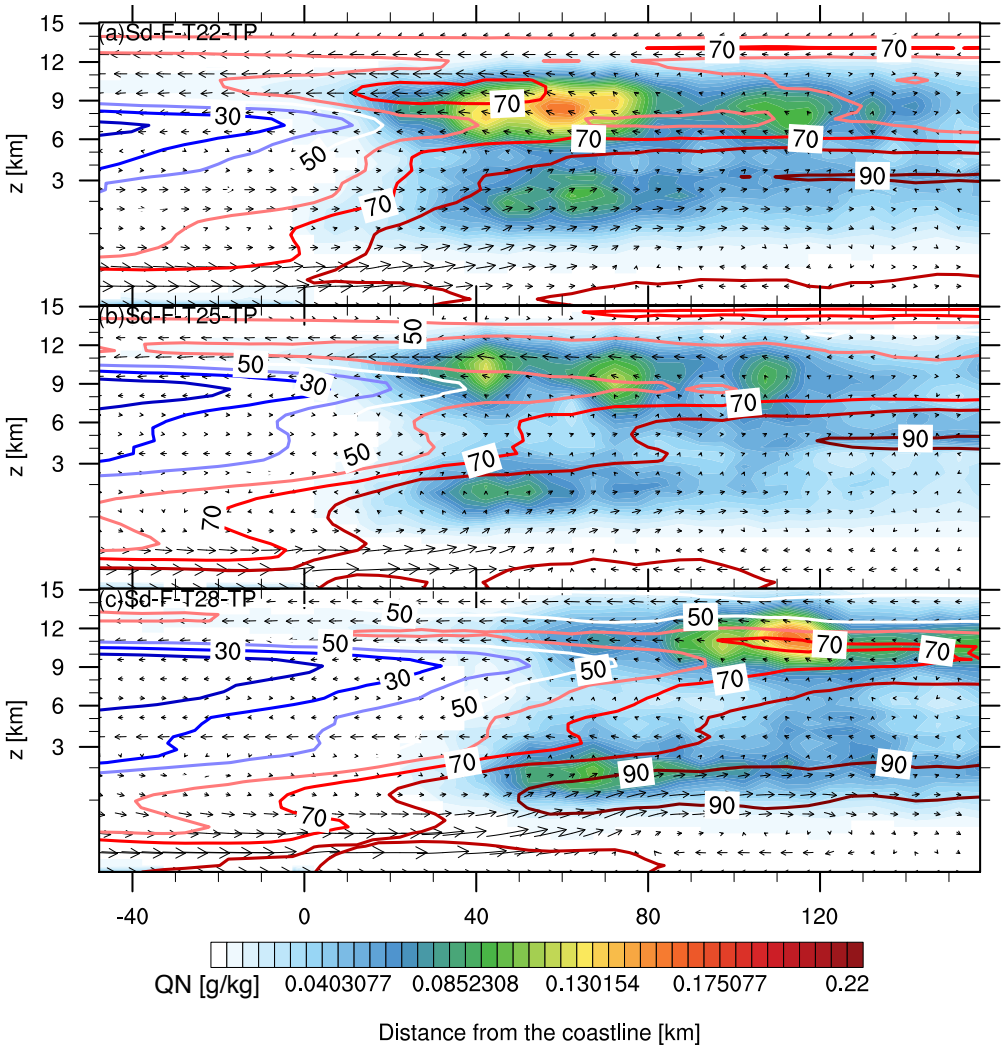

Figure 4.12 Vertical profiles of cloud condensate (color shaded), winds (vector) and relative humidity (color contoured) at 16:30 for Sd-F-TP cases with SST, 22(top), 25(middle) and 28(bottom) ˚C.

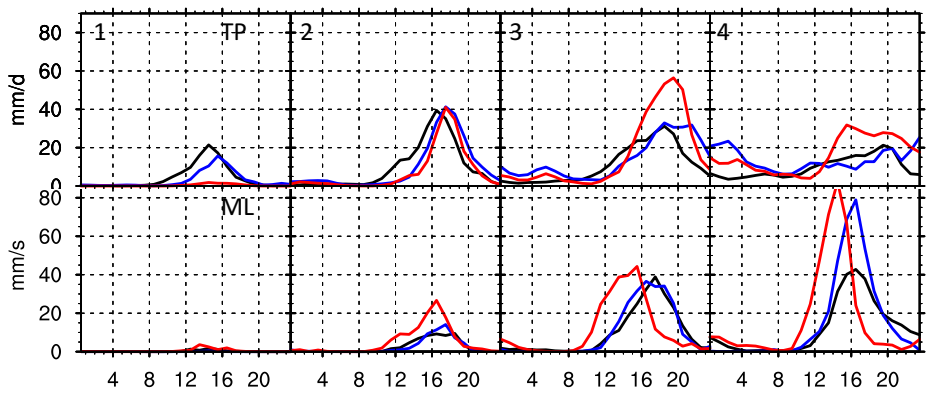

Figure 4.13. Composite diurnal cycles of surface rainfall averaged over the 40km wide blocks, the left most represents the block 1 (bounded by the left coastline) and 4 for the right most block bounded by the island center. The top and bottom rows are for TP and ML cases, respectively. Different colors are for different SSTs of 22 (blue), 25 (black), and 28 (red) ˚C.

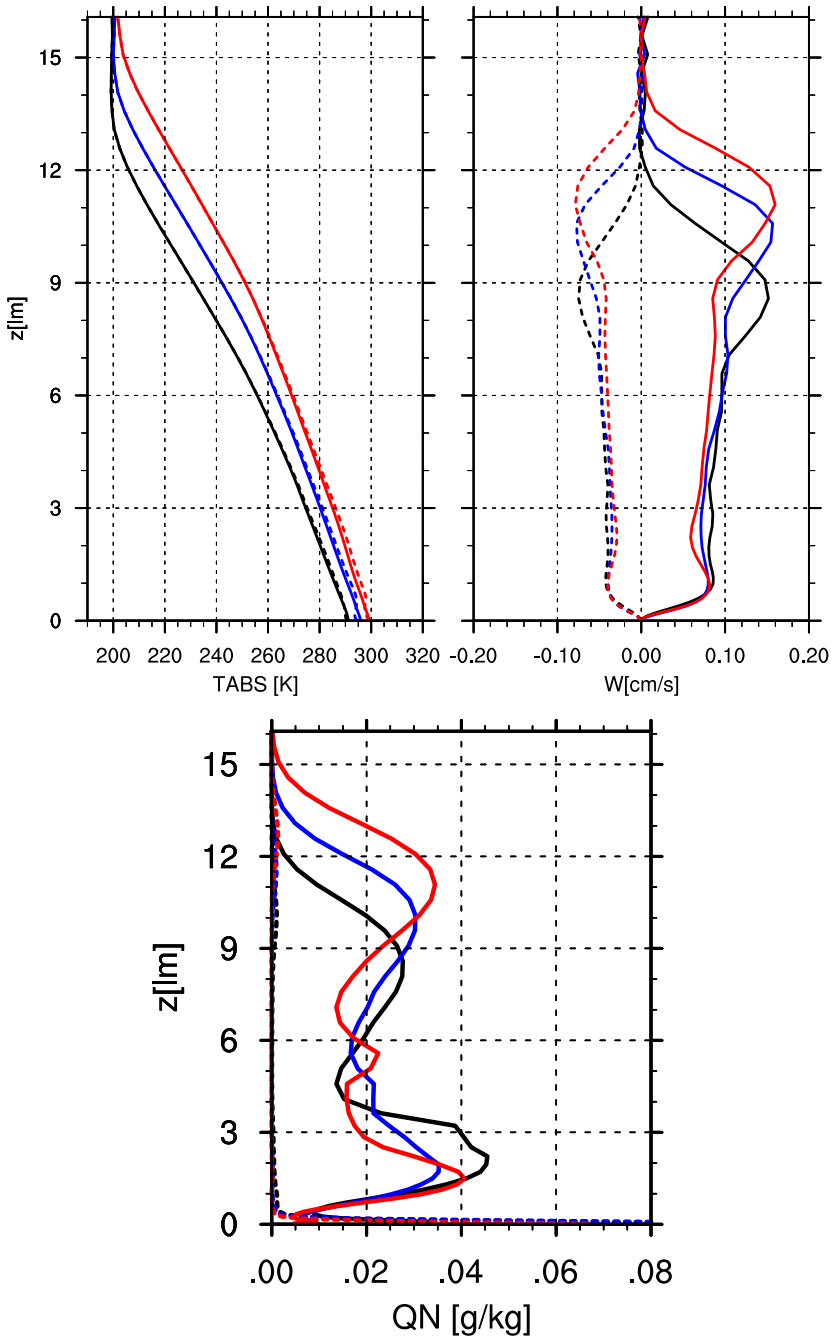

Figure 4.14. Mean profiles of (left) atmospheric temperatures, (right) vertical velocity, and cloud condensates (bottom), each are averaged over islands (solid) and ocean (dashed) grids separately. Color represents the prescribed SST from 22 (blue), 25 (black) to 28 (red) ˚C.

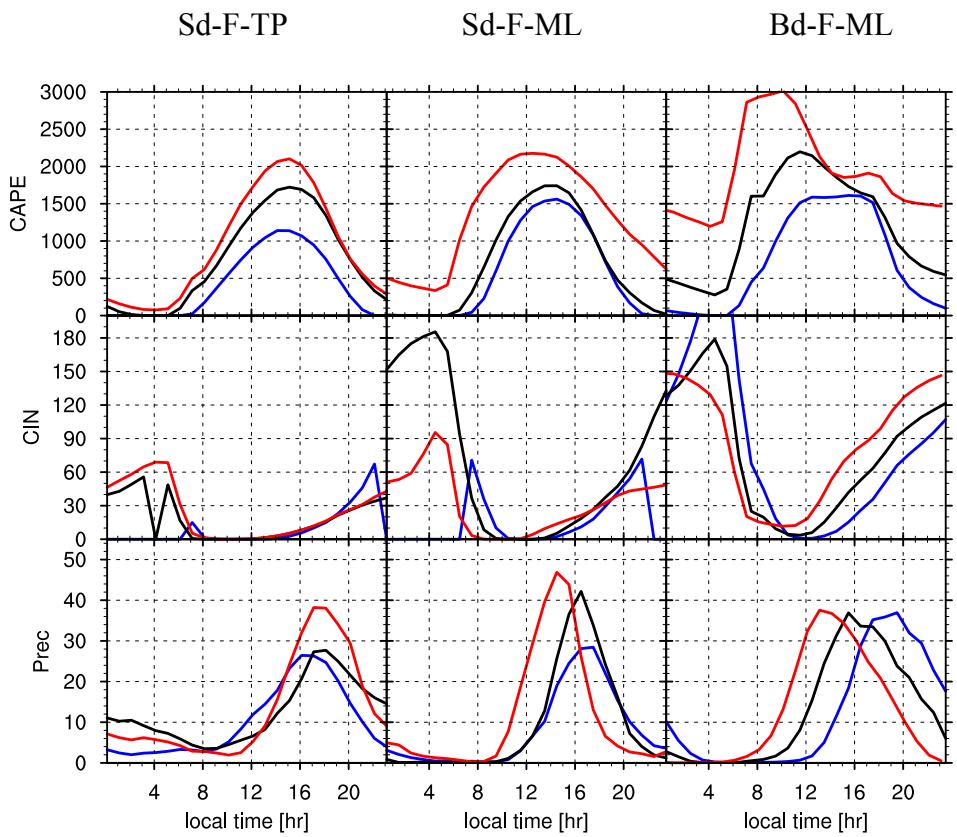

Figure 4.15 Composite diurnal cycles of CAPE (J/kg; top), CIN (J/kg; middle) and precipitation (mm/d; bottom) for Sd-F-TP (left), Sd-F-ML (middle) and Bd-F-ML (right column) cases with varying SSTs (T22; blue, T25; black and T28; red). Spatial averages are for central island region approximately 240km wide for Sd and 800km wide for Bd).

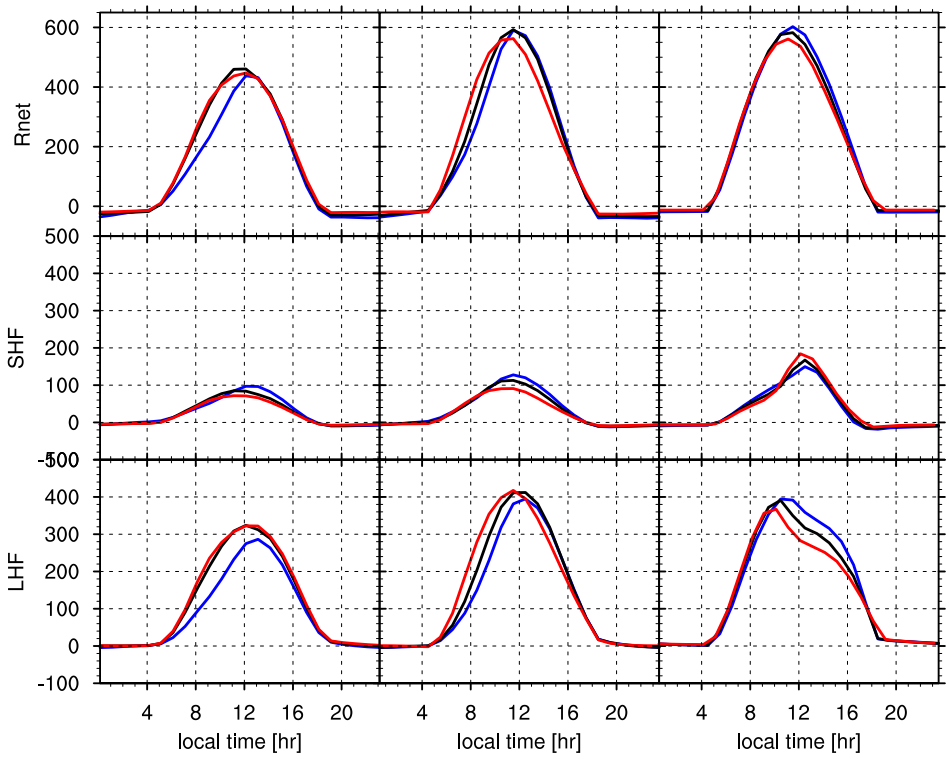

Figure 4.16 Same as 4.15, but for surface energy fluxes: (top row) net radiation at surface, (middle) sensible heat flux, (bottom) latent heat flux.

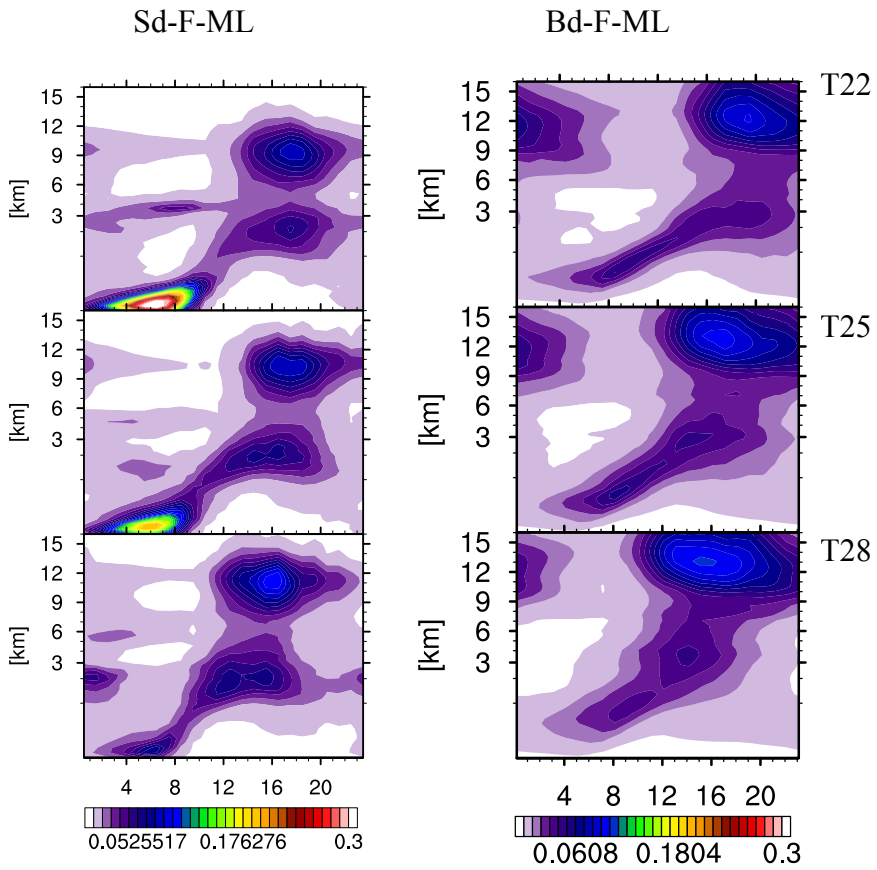

Figure 4.17. Diurnal cycle of cloud condensates (cloud liquid + ice) for (left columns) Sd-F-ML cases and (right columns) Bd-F-ML with varying SSTs (top:22 ˚C, middle:25 ˚C, bottom:28 ˚C).

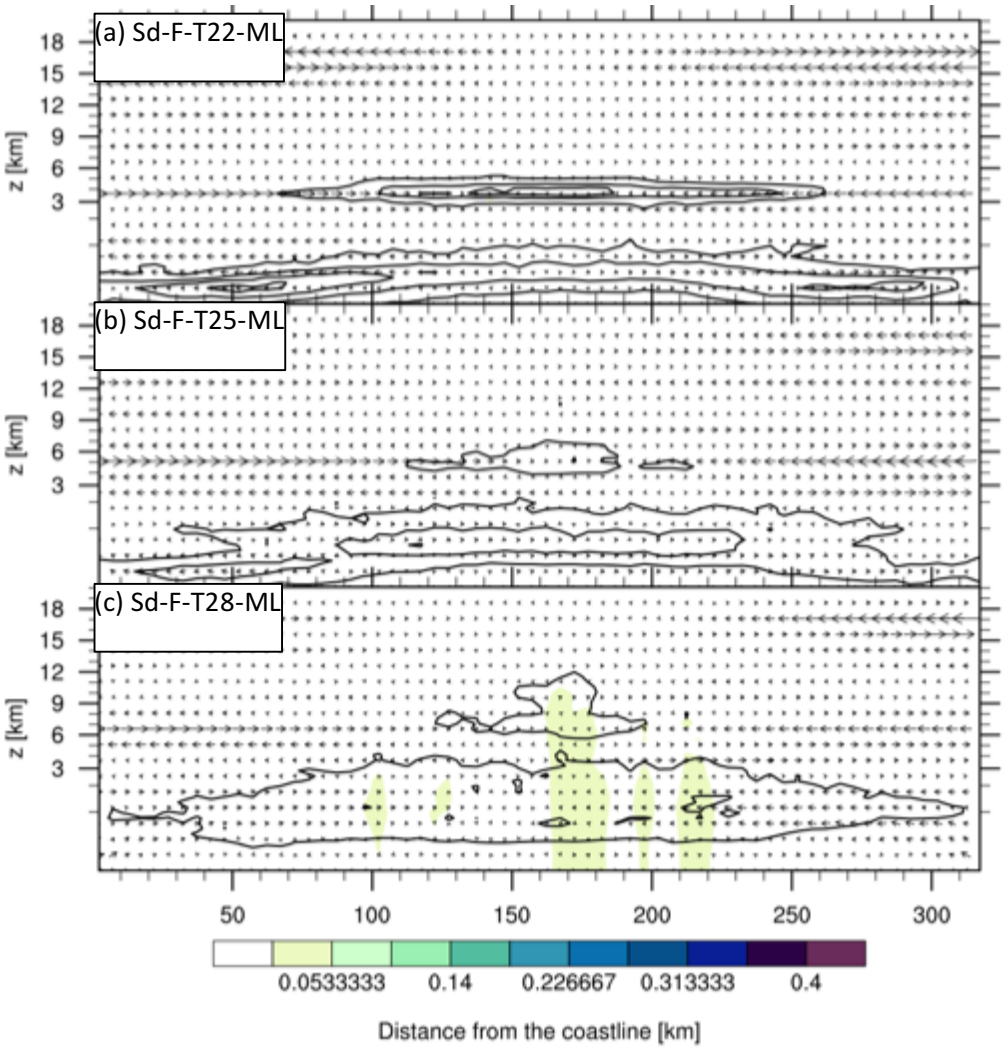

Figure 4.18 Snapshots of cloud water (black lines), precipitation (color shading) and wind vectors at 10:00 from Sd-F-ML cases with SST (a) 22, (b) 25, and (c) 28 ˚C. Cloud water is contoured at 0.01, 0.05, 0.1, 0.15, 0.2, 0.4 g/kg.

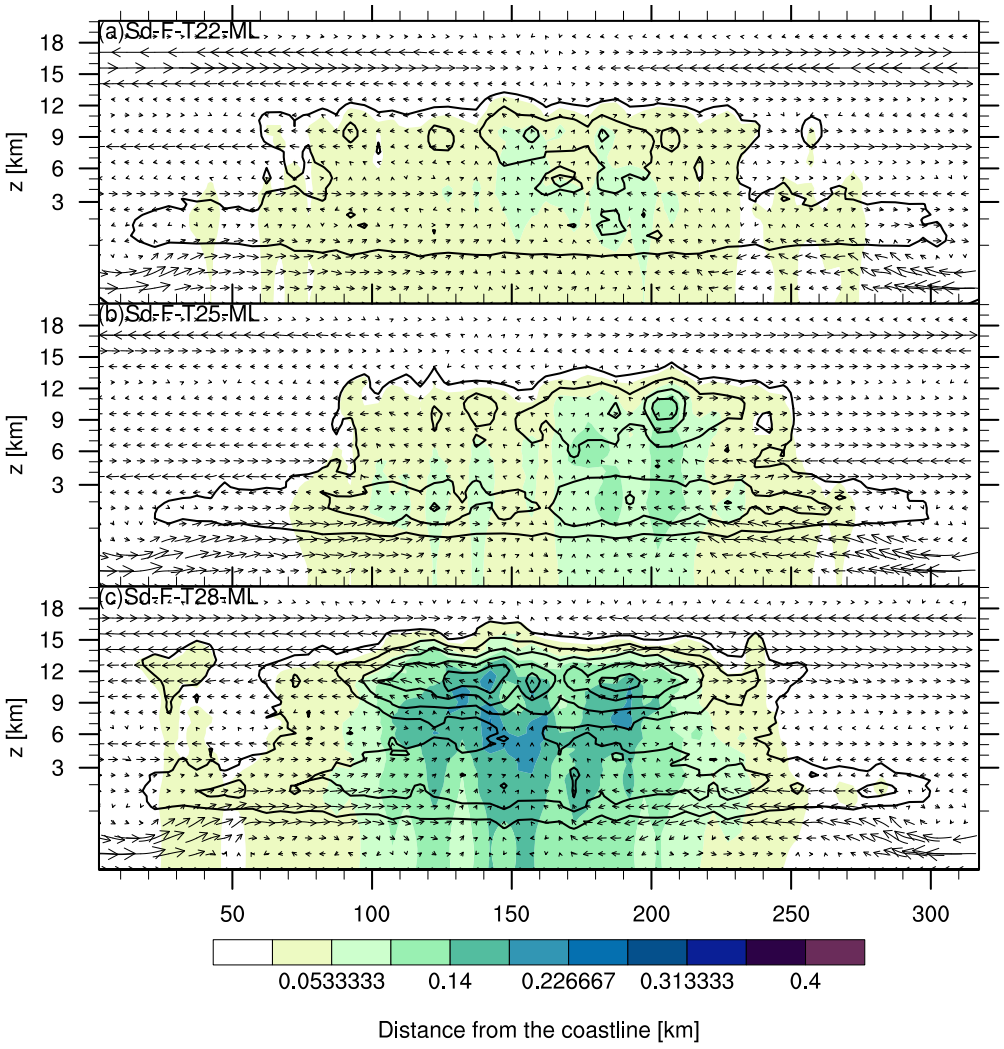

Figure 4.19 Same as Fig. 4.18, but at 14:00 (2 PM).

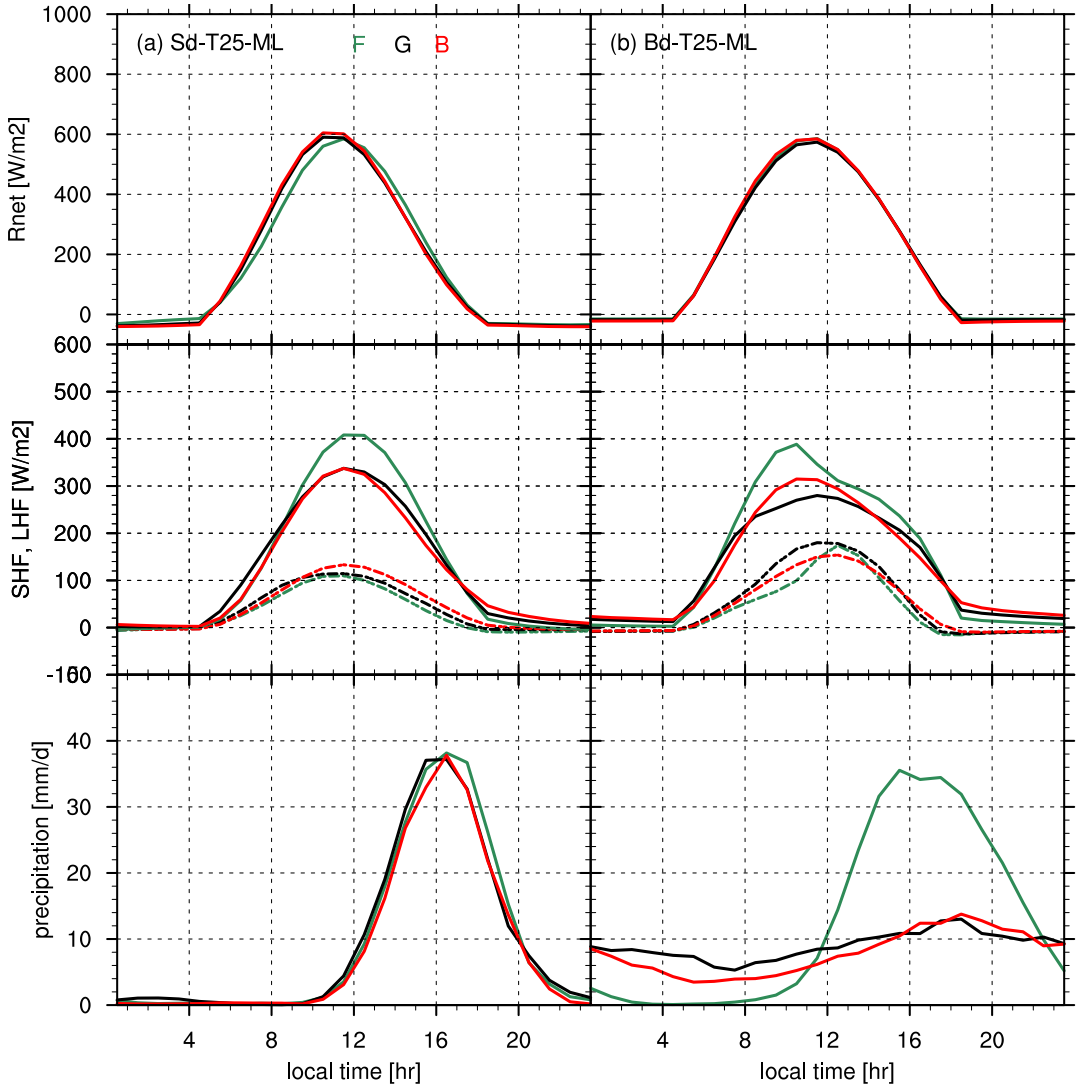

Figure 4.20 A composite diurnal cycle of (top) net radiation (middle) sensible (dashed) and latent (solid) heat fluxes, and (bottom) rainfall rate averaged over central island region with frequent precipitation.

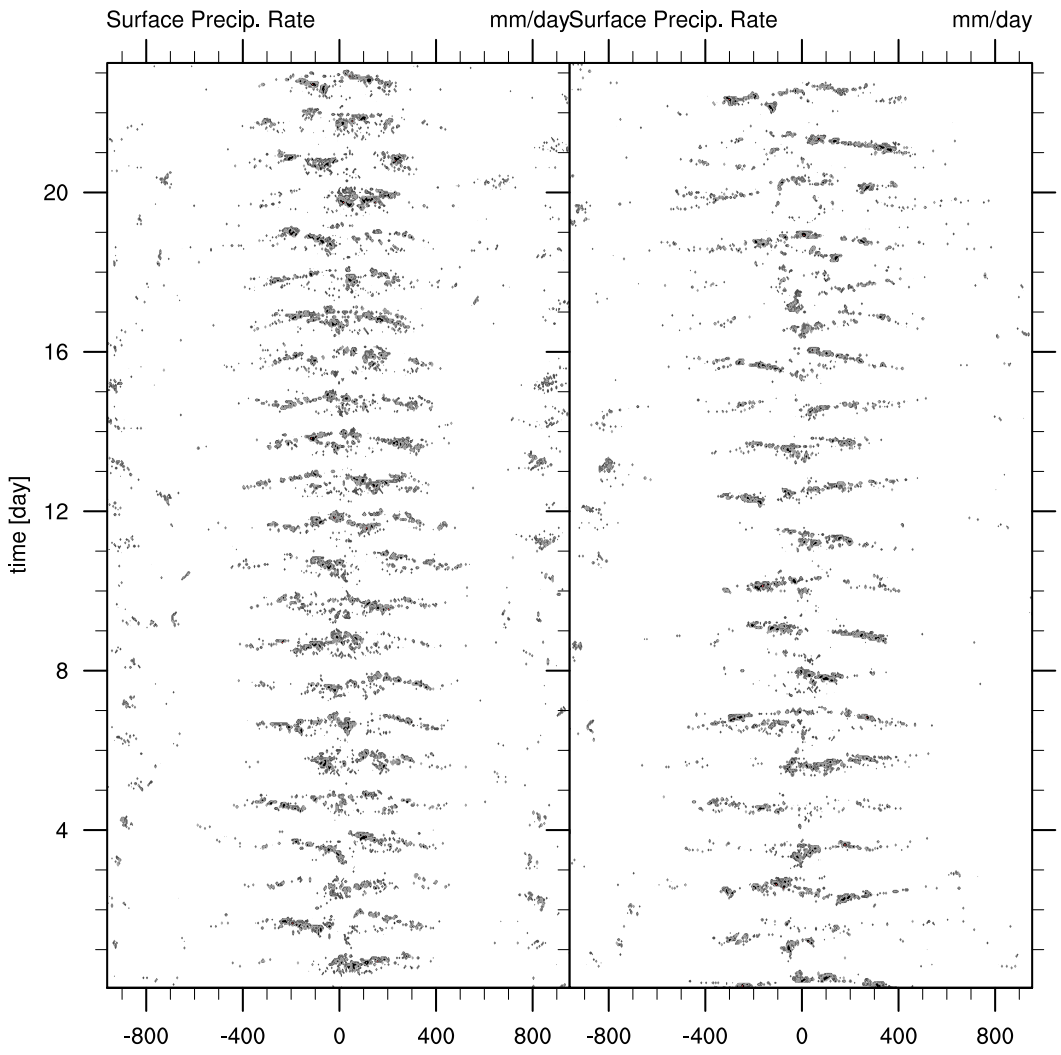

Figure 4.21. Time series of hourly surface precipitation over (left)Bd-F-T25-ML(same as Figure 4.12) island and (right)Bd-G-T25-ML. Last 23 days from the equilibrated states are shown.

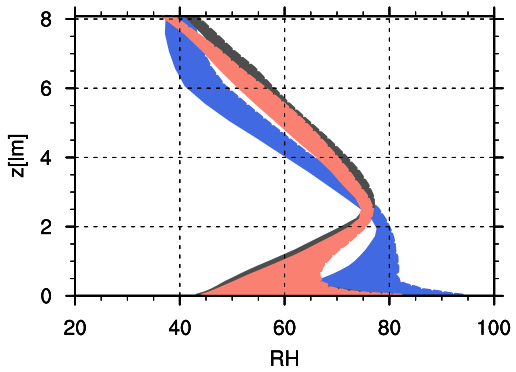

Figure 4.22 Mean diurnal variation of relative humidity from Bd-T25-ML cases with varying vegetation types (blue: forest, grey: grass, red: baresoil). Spatial average is taken over the central 500 km wide block of the larger island.

Chapter 5: Conclusion and Future Work

5.1 Summary and concluding remarks

The main accomplishment of this dissertation work is the development of a new land-surface scheme, called a Simplified Land Model (SLM), for use in the System for Atmospheric Modeling (SAM), which is a cloud-resolving model currently used by dozens of researchers in the United States and abroad. The main design philosophy that I followed in development of SLM has been to make it simple enough for the users of SAM-SLM to easily manipulate and improve when used in their own research.

The SLM is designed to have 1 layer of vegetation (if vegetated land is assigned) over multi-layered soil. Only 14 parameters need to be prescribed for each land type to specify the land vegetation and soil texture properties (example lists of variables are given in Table 2.1). The basic structure of SLM closely follows the first generation of the land surface schemes to keep it simple. However, some components are updated with the newer parameterizations to encompass more realistic land-atmosphere interaction. Based on energy and moisture balance considerations, SLM solves the prognostic equations for vegetation temperature, vegetation moisture storage, soil temperature and moisture content. The turbulent transfer of heat, moisture and momentum are computed using the bulk aerodynamic resistance method, which depends on the vegetation and soil properties. Transpiration is computed considering stomata resistance and its dependence on environmental conditions. The under canopy turbulence takes into account the atmospheric stability in the trunk space, and the roughness length for the turbulent transfer of moisture and heat is treated different from the transfer of momentum. A simple extinction method is used for the radiative transfer within the vegetation with extinction coefficient dependent on the vegetation's leaf area index, leaf angle distribution factor and solar zenith angle, combining direct and diffuse fluxes. Soil heat and moisture transport is calculated from a diffusion method where the transport is allowed only in a vertical direction. The implicit numerical scheme used in the implementation

of the soil model of SLM guaranties stability of the numerical algorithm and prevents numerical noise for any choice of the time step. Currently, snow/ice, biogeochemical cycle from the vegetation, topography induced drainage, etc., are not included, but may be included in the future.

The performance of the SLM has been tested offline using several observational datasets collected over different types of vegetated land in summertime. Overall, the model has been able to reproduce quite well the diurnal phase and amplitude variation of surface radiative and heat fluxes as well as the change of soil temperature with depth over multi-day periods. The scheme was found to overestimate (underestimate) somewhat the latent (sensible) heat flux. As was noted in Section 2, the equations describing radiative transfer over vegetated land are only valid for the case of dense vegetation with LAI being greater than 1, and generally are not applicable to the case of the sparse vegetation. In the dissertation research, this has been done for simplicity as the radiative transfer processes over the sparse vegetation is more complicated as it would require an introduction of the fractional area coverage within each grid cell. In the current version of SLM, the fractional coverage and, therefore, the sparse vegetation were not included in the spirit of simplicity. However, in the future extension of the SLM, the radiative transfer part of SLM will be improved by adopting more advanced methods used in other land models. Also, the evolution of the soil moisture tends to produce the largest discrepancies with observations, especially after the rainfall events. In the future, I will work to improve the soil representation in SLM as discussed in the Future Work section.

The new model, SAM-SLM, has first been applied to the case of the diurnal evolution of non-precipitating shallow clouds over land. In general, the computed surface energy budget was found to be in agreement with available observations. The sensitivity of simulations to various soil moisture conditions and various land surface types was also tested to see if the model results are consistent with our general understanding of the land-PBL coupling. The drier soil environment produces drier, deeper and warmer PBL with the higher cloud base as anticipated. The transpiration rate shows a significant sensitivity to the land type. For instance, the largest difference is between the baresoil and cornfield, which in turn leads to warmer, drier and deeper PBL over the baresoil than over vegetated land. The results generally confirm the notion that agricultural practices can indeed modify quite considerably the local PBL structure and associated mesoscale circulations.

Next, the SAM-SLM has been applied to an idealized case of diurnal cycle of convection over land. The main goal of the study was to see if the model is able to reproduce the observed

time of precipitation maximum over the most of continents, around of 5 pm of local time. The problem is not trivial, as most of the GCMs with convective parameterizations tend to simulate the peak of precipitation close to the local noon when the surface fluxes are at their maximum. The radiative-convective equilibrium (RCE) framework was used, in which the interactions between the radiation, clouds, atmospheric circulations and land processes are explicitly simulated over a two-dimensional island surrounded by an ocean. The RCE allows one to simulate the freely developing diurnal cycle without prescribing any large-scale forcing, lateral boundary conditions, and nudging that could, in a way, dictate the solution. The preliminary runs indicated that a free RCE over land would lead to a runaway greenhouse effect unless unrealistically small solar irradiation is used. Instead, the system was 'buffered' by surrounding the land with an ocean with constant prescribed SST. To study the effect of the surrounding ocean's temperature on the diurnal cycle of precipitation over land, the SST has been changed in rather wide range from 22 to 28^{o}C. This can also serve as a proxy for the effect of climate change on the continental convection. By using an island of two different sizes, relatively small (320 km) and large (1920 km), the various degree of influence of the ocean on the land diurnal cycle has been represented. Also, the differences in the diurnal cycle of precipitation between the midlatitudes and tropics have been studied by including the planetary rotation. It has to be noted that as far as I know, this work represents a first application of the RCE method to study the diurnal cycle of convection over land using a realistic land-surface model and applying no nudging of the large-scale profiles to observations.

The idealized simulations are able to reproduce a realistic timing of the precipitation maximum over land at about 5 pm, far later than the maximum of the surface fluxes. The delay has been explained by the inability of the PBL turbulence itself to produce large clouds without the gradual aggregation of convection during the shallow-to-deep convection transition via the cold-pool dynamics. The effect of planetary rotation has been shown to narrow the ascending branch of the large-scale thermally-direct circulation, which leads to drying of the coastal regions. One of the original findings of this study is that the peak precipitation over inland regions, that is, far away from the direct influence of the see-breeze, can be shifted to much earlier times in the case of a warmer ocean surrounding the land. In the ocean-atmosphere-land coupled system, the change of SST affects the atmospheric temperature and moisture profiles. The increment of SST indirectly leads to the drying of near surface humidity, hence reducing the mid-level cloud and

fog. The cloud-radiation feedback promotes an earlier moistening of the PBL because less solar radiation is reflected with the reduced cloud amount and more energy is partitioned into evaporating water vapor. While the cold pool dynamics is responsible for the transition from shallow into the deep convective clouds, the timing of precipitation onset and peak depends on the development of daytime mixed-layer, hence the diurnal cycle of surface heat fluxes. Therefore, as SST increases, the sequence that starts from the moistening of the PBL, appearance of the shallow clouds, initiation of cold pool dynamics for the clouds aggregation and then the dissipation of deep clouds tends to begin earlier; therefore, the onset and maximum of precipitation are shifted earlier over the inland regions when the remotely located ocean surface warms.

It has been also shown that the convection tends to favor organization into propagating convective systems over an island of larger size, with a timespan longer than 24-hour cycle. Different vegetation types have been also shown to modify this behavior quite considerably. Only the forested island shows a clear diurnal cycle of rainfall with the afternoon peak. The grass-covered and non-vegetated islands show a weak diurnal amplitude because the dry troposphere suppresses the development of deep convection. This feature that the diurnal cycle of precipitation is sensitive to the vegetation type can be applicable to its geographical differences.

CRM/LES has been extensively used to study the convection over land benefitting from its ability to explicitly resolve the convection. However, its application to the diurnal cycle of the precipitation over land has been limited to some idealized cases with the prescribed surface fluxes. There are other types of coupled land-atmosphere model, which takes a land model in GCMs and add it to LES/CRMs to enable the dynamic interaction between land surface and the PBL. However, such coupled models are not simple to use with LES/CRM because the land models have grown bulky with too many parameters and processes to be applicable globally. Therefore, SLM has been developed so that users have access to a more accessible and simpler version of land model that they can easily manipulate and incorporate into their research using SAM. The sensitivity simulations to study the land-atmosphere coupling can be easily prepared by changing the external parameter values to serve a users' research purpose, as presented throughout the dissertation research. The use of SAM-SLM can further contribute to gain insightful knowledge of the development of convection over land, especially its sensitivity to the vegetation types, soil moisture, or the even the influence from the remote ocean.

5.2 Future Work

5.2.1 Improving the representation of soil hydrology in SLM

The tests of SLM using observations have revealed several caveats that need to be fixed in the future. It has been mentioned in Chapter 2 that the evolution of soil moisture and temperature profiles show relatively large biases with respect to observations. The empirical parameterization of soil thermal and hydrological processes are believed to be the reason. I plan to conduct additional experiments to evaluate the accuracy of the soil model in SLM.

First, the natural soil column is composed of various layers of different textures. This complexity, not present in the current version of SLM, could affect the moisture transport within the soil and also the thermal conductive properties as they are parameterized mostly based on the instantaneous soil moisture content.

Another issue with the soil moisture transport process is the poorly parameterized rain infiltration rate. The observations suggest that the water during a rainfall event develops a finger-shaped flow even in homogenous soil and with uniform rain rate. However, the corresponding parameterizations are not well developed yet in literature and would, in general, go against my philosophy of a simple land model. Instead, I plan to use the soil observation data, along with the surface evaporation and rain data from the sites such as the SGP ARM sites or other sites, where the extensive data are available through AmeriFlux data community, to derive the new constants that provide the best infiltration estimates. Improvements in representation of the soil hydrology will be also beneficial for the prediction of the surface heat fluxes, as the transpiration, which dominates the overall evaporation rate, depends highly on the soil moisture level.

The current version of SLM assigns only one type of vegetation with 100 % coverage over each grid column. Although, the inhomogeneous surface representation is allowed in SLM, the sub-grid-scale extension has not been yet included. This may not be such a problem for LES studies because of high horizontal resolution, but may be a large problem for CRM studies when the surface inhomogeneity over grid cell of several kilometers can be quite important. Therefore, incorporating the fraction of a grid box to be covered by different vegetation types would be a further improvement.

In addition, a direct comparison of SLM performance on the same cases against other land models would be valuable test in a qualitative sense. One way to approach would be to incorporate the SLM into WRF model. The simulation results comparison with the default land model in WRF and WRF-SLM would be a good test of SLM performance. Focus of that work would be again on improving the soil model in SLM.

5.2.2 Extending 2D island simulations to 2.5D

The RCE simulations of an island using version of SAM without land model by Cronin et al. (2014) has shown the subsiding regions of the convectively generated circulations around a 3D island are narrower than over the 2D island cases presented here. As true 3D simulation over large islands would be prohibitively expensive, I will follow the methodology by Tompkins et al. (2001) who simulated an idealized tropical convection in a so-called 'bowling alley' domain which is simply a 3D domain with the size in one horizontal direction being much smaller than in the other. So, the large-scale circulation would be still quasi-2D, while much smaller clouds and turbulence in PBL would 3D, which is more realistic and may affect the results. For example, the horizontal winds are expected to be stronger in 2D because of different momentum transport dynamics than in 3D.

5.2.3 Diurnal rainfall variability over an inhomogeneous land surface

This dissertation has focused on exploring the statistically observed characteristics of the moist convection in idealized settings, such as convection over land with uniform surface properties. In reality, land surface is highly inhomogeneous (e.g., soil moisture gradients, sharp gradients in vegetation types, urban and vegetated land contrast, etc.), which tends to generate mesoscale circulations induced from the differential heating across the land, which may have implications on diurnal cycle of precipitation (e.g., Giorgi and Avissar, 1997). The SAM-SLM can be easily set up to incorporate cell-by-cell surface heterogeneity. Idealized SAM-SLM studies with the heterogeneous surface will be conducted using SAM in LES mode. In particular, the influence of soil moisture on the development of convection over land will be extensively investigated.

Bibliography

Abramopoulos, F., C. Rosenzweig, and B. Choudhury, 1988: Improved Ground Hydrology Calculations for Global Climate Models (GCMs): Soil Water Movement and Evapotranspiration. *J. Climate*, **1**, 921–941, doi:10.1175/1520-0442(1988)001<0921:IGHCFG>2.0.CO;2.

Alapaty, K., J. E. Pleim, S. Raman, D. S. Niyogi, and D. W. Byun, 1997: Simulation of Atmospheric Boundary Layer Processes Using Local- and Nonlocal-Closure Schemes. *J. Appl. Meteor.*, **36**, 214–233, doi:10.1175/1520-0450(1997)036<0214:SOABLP>2.0.CO;2.

Alfieri, J. G., D. Niyogi, P. D. Blanken, F. Chen, M. A. LeMone, K. E. Mitchell, M. B. Ek, and A. Kumar, 2008: Estimation of the Minimum Canopy Resistance for Croplands and Grasslands Using Data from the 2002 International H2O Project. *Mon. Wea. Rev.*, **136**, 4452–4469, doi:10.1175/2008MWR2524.1.

Anber, U., P. Gentine, S. Wang, and A. H. Sobel, 2015: Fog and rain in the Amazon, 1–15, doi:10.1073/pnas.1505077112.

Avissar, R., and T. Schmidt, 1998: An Evaluation of the Scale at which Ground-Surface Heat Flux Patchiness Affects the Convective Boundary Layer Using Large-Eddy Simulations. *J. Atmos. Sci.*, **55**, 2666–2689, doi:10.1175/1520-0469(1998)055<2666:AEOTSA>2.0.CO;2.

Bechtold, P., J.-P. Chaboureau, A. Beljaars, A. K. Betts, M. Köhler, M. Miller, and J.-L. Redelsperger, 2004: The simulation of the diurnal cycle of convective precipitation over land in a global model. *Q.J.R. Meteorol. Soc.*, **130**, 3119–3137, doi:10.1256/qj.03.103.

Betts, A. K., and C. Jakob, Evaluation of the diurnal cycle of precipitation, surface thermodynamics, and surface fluxes in the ECMWF model using LBA data, J. Geophys. Res., 107(D20), doi:10.1029/2001JD000427, 2002.

Betts, A. K., and M. A. F. Silva Dias, 2010: Progress in understanding land-surface-atmosphere coupling from LBA research. *Journal of Advances in Modeling Earth Systems*, **2**, doi:10.3894/JAMES.2010.2.6. http://doi.wiley.com/10.3894/JAMES.2010.2.6 (Accessed February 16, 2016).

B. J.J. van den Hurk, P. Viterbo, A. C.M. Beljaars, and A. Betts, 2000: Offline validation of the ERA40 surface scheme.

Böing, S. J., A. P. Siebesma, J. D. Korpershoek, and H. J. J. Jonker, 2012: Detrainment in deep

convection: DETRAINMENT IN DEEP CONVECTION. *Geophysical Research Letters*, **39**, n/a – n/a, doi:10.1029/2012GL053735.

Boybeyi, Z., and S. Raman, 1992: A three-dimensional numerical sensitivity study of convection over the Florida peninsula. *Boundary-Layer Meteorol*, **60**, 325–359, doi:10.1007/BF00155201.

Bretherton, C. S., 1987: A Theory for Nonprecipitating Moist Convection between Two Parallel Plates. Part I: Thermodynamics and "Linear" Solutions. *J. Atmos. Sci.*, **44**, 1809–1827, doi:10.1175/1520-0469(1987)044<1809:ATFNMC>2.0.CO;2.

——, and P. K. Smolarkiewicz, 1989: Gravity Waves, Compensating Subsidence and Detrainment around Cumulus Clouds. *J. Atmos. Sci.*, **46**, 740–759, doi:10.1175/1520-0469(1989)046<0740:GWCSAD>2.0.CO;2.

——, P. N. Blossey, and M. E. Peters, 2006: Interpretation of simple and cloud-resolving simulations of moist convection–radiation interaction with a mock-Walker circulation. *Theor. Comput. Fluid Dyn.*, **20**, 421–442, doi:10.1007/s00162-006-0029-7.

Brown, A. R., and Coauthors, 2002: Large-eddy simulation of the diurnal cycle of shallow cumulus convection over land. *Q.J.R. Meteorol. Soc.*, **128**, 1075–1093, doi:10.1256/003590002320373210.

Buckman, H. O., and N. C. Brady, 1969: *The nature and properties of soils*. Macmillan New York.

Burpee, R. W., and L. N. Lahiffi, 1984: Area-Average Rainfall Variations on Sea-Breeze Days in South Florida. *Mon. Wea. Rev.*, **112**, 520–534, doi:10.1175/1520-0493(1984)112<0520:AARVOS>2.0.CO;2.

Businger, J. A., J. C. Wyngaard, Y. Izumi, and E. F. Bradley, 1971: Flux-Profile Relationships in the Atmospheric Surface Layer. *J. Atmos. Sci.*, **28**, 181–189, doi:10.1175/1520-0469(1971)028<0181:FPRITA>2.0.CO;2.

Carbone, R. E., and J. D. Tuttle, 2008: Rainfall Occurrence in the U.S. Warm Season: The Diurnal Cycle*. *Journal of Climate*, **21**, 4132–4146, doi:10.1175/2008JCLI2275.1.

——, J. W. Wilson, T. D. Keenan, and J. M. Hacker, 2000: Tropical Island Convection in the Absence of Significant Topography. Part I: Life Cycle of Diurnally Forced Convection. *Mon. Wea. Rev.*, **128**, 3459–3480, doi:10.1175/1520-0493(2000)128<3459:TICITA>2.0.CO;2.

Chaboureau, J.-P., F. Guichard, J.-L. Redelsperger, and J.-P. Lafore, 2004: The role of stability and moisture in the diurnal cycle of convection over land. *Q.J.R. Meteorol. Soc.*, **130**, 3105–3117, doi:10.1256/qj.03.132.

Chemel, C., M. R. Russo, J. A. Pyle, R. S. Sokhi, and C. Schiller, 2009: Quantifying the Imprint of a Severe Hector Thunderstorm during ACTIVE/SCOUT-O3 onto the Water Content in the Upper Troposphere/Lower Stratosphere. *Mon. Wea. Rev.*, **137**, 2493–2514,

doi:10.1175/2008MWR2666.1.

Chen, F., and R. Avissar, 1994: The Impact of Land-Surface Wetness Heterogeneity on Mesoscale Heat Fluxes. *J. Appl. Meteor.*, **33**, 1323–1340, doi:10.1175/1520-0450(1994)033<1323:TIOLSW>2.0.CO;2.

——, and J. Dudhia, 2001: Coupling an Advanced Land Surface–Hydrology Model with the Penn State–NCAR MM5 Modeling System. Part I: Model Implementation and Sensitivity. *Mon. Wea. Rev.*, **129**, 569–585, doi:10.1175/1520-0493(2001)129<0569:CAALSH>2.0.CO;2.

Chen, S. S., and R. A. Houze, 1997: Diurnal variation and life-cycle of deep convective systems over the tropical pacific warm pool. *Q.J.R. Meteorol. Soc.*, **123**, 357–388, doi:10.1002/qj.49712353806.

Clapp, R. B., and G. M. Hornberger, 1978: Empirical equations for some soil hydraulic properties. *Water Resources Research*, **14**, 601–604, doi:10.1029/WR014i004p00601.

Collins, W. D., and Coauthors, 2006: The Formulation and Atmospheric Simulation of the Community Atmosphere Model Version 3 (CAM3). *J. Climate*, **19**, 2144–2161, doi:10.1175/JCLI3760.1.

Cooter, E. J., and D. B. Schwede, 2000: Sensitivity of the National Oceanic and Atmospheric Administration multilayer model to instrument error and parameterization uncertainty. *J. Geophys. Res.*, **105**, 6695–6707, doi:10.1029/1999JD901080.

Cosby, B. J., G. M. Hornberger, R. B. Clapp, and T. R. Ginn, 1984: A Statistical Exploration of the Relationships of Soil Moisture Characteristics to the Physical Properties of Soils. *Water Resources Research*, **20**, 682–690, doi:10.1029/WR020i006p00682.

Coudert, B., and C. Ottlé, 2007: An improved SVAT model calibration strategy based on the optimisation of surface temperature temporal dynamics. *Geophysical Research Letters*, **34**, doi:10.1029/2006GL028778. http://doi.wiley.com/10.1029/2006GL028778 (Accessed February 16, 2016).

Courault, D., P. Drobinski, Y. Brunet, P. Lacarrere, and C. Talbot, 2007: Impact of surface heterogeneity on a buoyancy-driven convective boundary layer in light winds. *Boundary-Layer Meteorol*, **124**, 383–403, doi:10.1007/s10546-007-9172-y.

Cronin, T. W., K. A. Emanuel, and P. Molnar, 2015: Island precipitation enhancement and the diurnal cycle in radiative-convective equilibrium: Island Rainfall Enhancement in Radiative-Convective Equilibrium. *Quarterly Journal of the Royal Meteorological Society*, **141**, 1017–1034, doi:10.1002/qj.2443.

Cueto-Felgueroso, L., and R. Juanes, 2008: Nonlocal Interface Dynamics and Pattern Formation in Gravity-Driven Unsaturated Flow through Porous Media. *Phys. Rev. Lett.*, **101**, 244504.

Cueto-Felgueroso, L., and R. Juanes, 2009: A phase field model of unsaturated flow. *Water Resour. Res.*, **45**, W10409, doi:10.1029/2009WR007945.

Curtis, P. S., P. J. Hanson, P. Bolstad, C. Barford, J. C. Randolph, H. P. Schmid, and K. B. Wilson, 2002: Biometric and eddy-covariance based estimates of annual carbon storage in five eastern North American deciduous forests. *Agricultural and Forest Meteorology*, **113**, 3–19, doi:10.1016/S0168-1923(02)00099-0.

Dai, A., 2001: Global Precipitation and Thunderstorm Frequencies. Part II: Diurnal Variations. *J. Climate*, **14**, 1112–1128, doi:10.1175/1520-0442(2001)014<1112:GPATFP>2.0.CO;2.

——, 2006: Precipitation Characteristics in Eighteen Coupled Climate Models. *J. Climate*, **19**, 4605–4630, doi:10.1175/JCLI3884.1.

——, and K. E. Trenberth, 2004: The Diurnal Cycle and Its Depiction in the Community Climate System Model. *J. Climate*, **17**, 930–951, doi:10.1175/1520-0442(2004)017<0930:TDCAID>2.0.CO;2.

——, X. Lin, and K.-L. Hsu, 2007: The frequency, intensity, and diurnal cycle of precipitation in surface and satellite observations over low- and mid-latitudes. *Climate Dynamics*, **29**, 727–744, doi:10.1007/s00382-007-0260-y.

Deardorff, J. W., 1977: A Parameterization of Ground-Surface Moisture Content for Use in Atmospheric Prediction Models. *J. Appl. Meteor.*, **16**, 1182–1185, doi:10.1175/1520-0450(1977)016<1182:APOGSM>2.0.CO;2.

——, 1978: Efficient prediction of ground surface temperature and moisture, with inclusion of a layer of vegetation. *J. Geophys. Res*, **83**, 1889–1903, doi:10.1029/JC083iC04p01889.

Del Genio, A. D., and J. Wu, 2010: The Role of Entrainment in the Diurnal Cycle of Continental Convection. *Journal of Climate*, **23**, 2722–2738, doi:10.1175/2009JCLI3340.1.

DeMott, C. A., D. A. Randall, and M. Khairoutdinov, 2007: Convective Precipitation Variability as a Tool for General Circulation Model Analysis. *Journal of Climate*, **20**, 91–112, doi:10.1175/JCLI3991.1.

Derbyshire, S. H., I. Beau, P. Bechtold, J.-Y. Grandpeix, J.-M. Piriou, J.-L. Redelsperger, and P. M. M. Soares, 2004: Sensitivity of moist convection to environmental humidity. *Q.J.R. Meteorol. Soc.*, **130**, 3055–3079, doi:10.1256/qj.03.130.

DiCarlo, D. A., 2004: Experimental measurements of saturation overshoot on infiltration. *Water Resour. Res.*, **40**, W04215, doi:10.1029/2003WR002670.

Dickinson, R, Henderson-Sellers, A, Kennedy, P, and Wilson, M, 1986: Biosphere-atmosphere Transfer Scheme (BATS) for the NCAR Community Climate Model. doi:10.5065/D6668B58. http://dx.doi.org/10.5065/D6668B58 (Accessed February 16, 2016).

Dickinson, R. E., 1988: The Force–Restore Model for Surface Temperatures and Its Generalizations. *J. Climate*, **1**, 1086–1097, doi:10.1175/1520-0442(1988)001<1086:TFMFST>2.0.CO;2.

——, and A. Henderson-Sellers, 1988: Modelling tropical deforestation: A study of GCM land-surface parametrizations. *Q.J.R. Meteorol. Soc.*, **114**, 439–462, doi:10.1002/qj.49711448009.

——, ——, and Kennedy, P, 1993: Biosphere-atmosphere Transfer Scheme (BATS) Version 1e as Coupled to the NCAR Community Climate Model. doi:10.5065/D67W6959. http://dx.doi.org/10.5065/D67W6959 (Accessed February 16, 2016).

Dirmeyer, P. A., and Coauthors, 2012: Simulating the diurnal cycle of rainfall in global climate models: resolution versus parameterization. *Climate Dynamics*, **39**, 399–418, doi:10.1007/s00382-011-1127-9.

Done, J. M., G. C. Craig, S. L. Gray, P. A. Clark, and M. E. B. Gray, 2006: Mesoscale simulations of organized convection: Importance of convective equilibrium. *Quarterly Journal of the Royal Meteorological Society*, **132**, 737–756, doi:10.1256/qj.04.84.

Dudhia, J., 1989: Numerical Study of Convection Observed during the Winter Monsoon Experiment Using a Mesoscale Two-Dimensional Model. *J. Atmos. Sci.*, **46**, 3077–3107, doi:10.1175/1520-0469(1989)046<3077:NSOCOD>2.0.CO;2.

Ek, M., and L. Mahrt, 1994: Daytime Evolution of Relative Humidity at the Boundary Layer Top. *Mon. Wea. Rev.*, **122**, 2709–2721, doi:10.1175/1520-0493(1994)122<2709:DEORHA>2.0.CO;2.

——, and A. a. M. Holtslag, 2004: Influence of Soil Moisture on Boundary Layer Cloud Development. *J. Hydrometeor*, **5**, 86–99, doi:10.1175/1525-7541(2004)005<0086:IOSMOB>2.0.CO;2.

Essery, R. L. H., M. J. Best, R. A. Betts, P. M. Cox, and C. M. Taylor, 2003: Explicit Representation of Subgrid Heterogeneity in a GCM Land Surface Scheme. *J. Hydrometeor*, **4**, 530–543, doi:10.1175/1525-7541(2003)004<0530:EROSHI>2.0.CO;2.

Estoque, M. A., 1961: A theoretical investigation of the sea breeze. *Q.J.R. Meteorol. Soc.*, **87**, 136–146, doi:10.1002/qj.49708737203.

Findell, K. L., and E. A. B. Eltahir, 2003: Atmospheric Controls on Soil Moisture–Boundary Layer Interactions. Part I: Framework Development. *J. Hydrometeor*, **4**, 552–569, doi:10.1175/1525-7541(2003)004<0552:ACOSML>2.0.CO;2.

Findell, K. L., P. Gentine, B. R. Lintner, and C. Kerr Probability of afternoon precipitation in eastern United States and Mexico enhanced by high evaporation, *Nat Geosci*, 4(7), 434–439, doi:10.1038/NGEO1174.

Fovell, R. G., 2005: Convective Initiation ahead of the Sea-Breeze Front. *Mon. Wea. Rev.*, **133**, 264–278, doi:10.1175/MWR-2852.1.

Garcia-Carreras, L., D. J. Parker, and J. H. Marsham, 2011: What is the Mechanism for the Modification of Convective Cloud Distributions by Land Surface–Induced Flows? *Journal of the Atmospheric Sciences*, **68**, 619–634, doi:10.1175/2010JAS3604.1.

Giorgi, F., and R. Avissar, 1997: Representation of heterogeneity effects in Earth system modeling: Experience from land surface modeling. *Rev. Geophys.*, **35**, 413–437, doi:10.1029/97RG01754.

Goudriaan, J., 1977: *Crop micrometeorology: a simulation study*. Pudoc, Center for Agricultural Publishing and Documentation, Wageningen, 249 pp.

Grabowski, W. W., 2001: Coupling Cloud Processes with the Large-Scale Dynamics Using the Cloud-Resolving Convection Parameterization (CRCP). *J. Atmos. Sci.*, **58**, 978–997, doi:10.1175/1520-0469(2001)058<0978:CCPWTL>2.0.CO;2.

——, 2006: Indirect Impact of Atmospheric Aerosols in Idealized Simulations of Convective–Radiative Quasi Equilibrium. *J. Climate*, **19**, 4664–4682, doi:10.1175/JCLI3857.1.

——, and M. W. Moncrieff, 2002: Large-scale organization of tropical convection in two-dimensional explicit numerical simulations: Effects of interactive radiation. *Q.J.R. Meteorol. Soc.*, **128**, 2349–2375, doi:10.1256/qj.01.104.

——, J.-I. Yano, and M. W. Moncrieff, 2000: Cloud Resolving Modeling of Tropical Circulations Driven by Large-Scale SST Gradients. *J. Atmos. Sci.*, **57**, 2022–2040, doi:10.1175/1520-0469(2000)057<2022:CRMOTC>2.0.CO;2.

——, P. Bechtold, A. Cheng, R. Forbes, C. Halliwell, M. Khairoutdinov, S. Lang, T. Nasuno, J. Petch, W.-K. Tao, R. Wong, W. Wu and K.-M., 2006: Daytime convective development over land: A model intercomparison based on LBA observations. *Quarterly Journal of the Royal Meteorological Society*, **132**, 317–344, doi:10.1256/qj.04.147.

Graham, D.N. and M. B. Butts (2005) Flexible, integrated watershed modelling with MIKE SHE. In Watershed Models, Eds. V.P. Singh & D.K. Frevert Pages 245-272, CRC Press. ISBN: 0849336090

Gray, W. M., and R. W. Jacobson, 1977: Diurnal Variation of Deep Cumulus Convection. *Mon. Wea. Rev.*, **105**, 1171–1188, doi:10.1175/1520-0493(1977)105<1171:DVODCC>2.0.CO;2.

Guichard, F., and Coauthors, 2004: Modelling the diurnal cycle of deep precipitating convection over land with cloud-resolving models and single-column models. *Q.J.R. Meteorol. Soc.*, **130**, 3139–3172, doi:10.1256/qj.03.145.

Gusev, E. M., O. N. Nasonova, and L. Y. Dzhogan, 2006: The simulation of runoff from small catchments in the permafrost zone by the SWAP model. *Water Resour*, **33**, 115–126, doi:10.1134/S0097807806020011.

van Heerwaarden, C. C., and J. V. Guerau de Arellano, 2008: Relative Humidity as an Indicator for Cloud Formation over Heterogeneous Land Surfaces. *J. Atmos. Sci.*, **65**, 3263–3277, doi:10.1175/2008JAS2591.1.

Held, I. M., R. S. Hemler, and V. Ramaswamy, 1993: Radiative-Convective Equilibrium with Explicit

Two-Dimensional Moist Convection. *J. Atmos. Sci.*, **50**, 3909–3927, doi:10.1175/1520-0469(1993)050<3909:RCEWET>2.0.CO;2.

Hendon, H. H., and K. Woodberry, 1993: The diurnal cycle of tropical convection. *J. Geophys. Res.*, **98**, 16623–16637, doi:10.1029/93JD00525.

Holton, J. R., 1967: The diurnal boundary layer wind oscillation above sloping terrain1. *Tellus*, **19**, 199–205, doi:10.1111/j.2153-3490.1967.tb01473.x.

Houston, A. L., and D. Niyogi, 2007: The Sensitivity of Convective Initiation to the Lapse Rate of the Active Cloud-Bearing Layer. *Monthly Weather Review*, **135**, 3013–3032, doi:10.1175/MWR3449.1.

Huang, H.-Y., and S. A. Margulis, 2009: On the impact of surface heterogeneity on a realistic convective boundary layer. *Water Resour. Res.*, **45**, W04425, doi:10.1029/2008WR007175.

——, and ——, 2013: Impact of soil moisture heterogeneity length scale and gradients on daytime coupled land-cloudy boundary layer interactions. *Hydrol. Process.*, **27**, 1988–2003, doi:10.1002/hyp.9351.

——, ——, C. R. Chu, and H.-C. Tsai, 2011: Investigation of the impacts of vegetation distribution and evaporative cooling on synthetic urban daytime climate using a coupled LES—LSM model. *Hydrol. Process.*, **25**, 1574–1586, doi:10.1002/hyp.7919.

van den Hurk, B. J. J. M., P. Viterbo, and S. O. Los, 2003: Impact of leaf area index seasonality on the annual land surface evaporation in a global circulation model. *J. Geophys. Res.*, **108**, 4191, doi:10.1029/2002JD002846.

Idso, S. B., R. D. Jackson, R. J. Reginato, B. A. Kimball, and F. S. Nakayama, 1975: The Dependence of Bare Soil Albedo on Soil Water Content. *J. Appl. Meteor.*, **14**, 109–113, doi:10.1175/1520-0450(1975)014<0109:TDOBSA>2.0.CO;2.

Jacquemin, B., and J. Noilhan, 1990: Sensitivity study and validation of a land surface parameterization using the HAPEX-MOBILHY data set. *Boundary-Layer Meteorol*, **52**, 93–134, doi:10.1007/BF00123180.

Jarvis, P. G., 1976: The Interpretation of the Variations in Leaf Water Potential and Stomatal Conductance Found in Canopies in the Field. *Philosophical Transactions of the Royal Society of London B: Biological Sciences*, **273**, 593–610.

Jiang, X., N.-C. Lau, and S. A. Klein, 2006: Role of eastward propagating convection systems in the diurnal cycle and seasonal mean of summertime rainfall over the U.S. Great Plains. *Geophysical Research Letters*, **33**, doi:10.1029/2006GL027022. http://doi.wiley.com/10.1029/2006GL027022 (Accessed February 17, 2016).

Johansen, O., 1977: *Thermal conductivity of soils*. DTIC Document.

Johnson, R. H., and B. E. Mapes, 2001: Mesoscale Processes and Severe Convective Weather. *Severe Convective Storms*, C.A. Doswell, Ed., American Meteorological Society, Boston, MA, 71–122 http://dx.doi.org/10.1007/978-1-935704-06-5_3.

——, P. E. Ciesielski, and J. A. Cotturone, 2001: Multiscale Variability of the Atmospheric Mixed Layer over the Western Pacific Warm Pool. *J. Atmos. Sci.*, **58**, 2729–2750, doi:10.1175/1520-0469(2001)058<2729:MVOTAM>2.0.CO;2.

——, ——, T. S. L'Ecuyer, and A. J. Newman, 2010: Diurnal Cycle of Convection during the 2004 North American Monsoon Experiment. *Journal of Climate*, **23**, 1060–1078, doi:10.1175/2009JCLI3275.1.

Jorgensen, D. P., and M. A. LeMone, 1989: Vertically Velocity Characteristics of Oceanic Convection. *J. Atmos. Sci.*, **46**, 621–640, doi:10.1175/1520-0469(1989)046<0621:VVCOOC>2.0.CO;2.

Kang, S.-L., and G. H. Bryan, 2011: A Large-Eddy Simulation Study of Moist Convection Initiation over Heterogeneous Surface Fluxes. *Mon. Wea. Rev.*, **139**, 2901–2917, doi:10.1175/MWR-D-10-05037.1.

——, D. Lenschow, and P. Sullivan, 2012: Effects of Mesoscale Surface Thermal Heterogeneity on Low-Level Horizontal Wind Speeds. *Boundary-Layer Meteorol*, **143**, 409–432, doi:10.1007/s10546-011-9691-4.

Khairoutdinov, M., and D. Randall, 2006: High-Resolution Simulation of Shallow-to-Deep Convection Transition over Land. *J. Atmos. Sci.*, **63**, 3421–3436, doi:10.1175/JAS3810.1.

——, and K. Emanuel, 2013: Rotating radiative-convective equilibrium simulated by a cloud-resolving model. *J. Adv. Model. Earth Syst.*, **5**, 816–825, doi:10.1002/2013MS000253.

——, D. Randall, and C. DeMott, 2005: Simulations of the Atmospheric General Circulation Using a Cloud-Resolving Model as a Superparameterization of Physical Processes. *J. Atmos. Sci.*, **62**, 2136–2154, doi:10.1175/JAS3453.1.

——, and D. A. Randall, 2001: A cloud resolving model as a cloud parameterization in the NCAR Community Climate System Model: Preliminary results. *Geophys. Res. Lett.*, **28**, 3617–3620, doi:10.1029/2001GL013552.

Kikuchi, K., and B. Wang, 2008: Diurnal Precipitation Regimes in the Global Tropics*. *J. Climate*, **21**, 2680–2696, doi:10.1175/2007JCLI2051.1.

Kingsmill, D. E., 1995: Convection Initiation Associated with a Sea-Breeze Front, a Gust Front, and Their Collision. *Mon. Wea. Rev.*, **123**, 2913–2933, doi:10.1175/1520-0493(1995)123<2913:CIAWAS>2.0.CO;2.

Kitoh, A., and O. Arakawa, 2005: Reduction in tropical rainfall diurnal variation by global warming simulated by a 20-km mesh climate model: REDUCTION IN RAINFALL DIURNAL CYCLE.

Geophysical Research Letters, **32**, n/a – n/a, doi:10.1029/2005GL023350.

Koster, R. D., M. J. Suarez, A. Ducharne, M. Stieglitz, and P. Kumar, 2000: A catchment-based approach to modeling land surface processes in a general circulation model: 1. Model structure. *J. Geophys. Res.*, **105**, 24809–24822, doi:10.1029/2000JD900327.

Krinner, G., and Coauthors, 2005: A dynamic global vegetation model for studies of the coupled atmosphere-biosphere system. *Global Biogeochem. Cycles*, **19**, GB1015, doi:10.1029/2003GB002199.

Kuang, Z., and C. S. Bretherton, 2006: A Mass-Flux Scheme View of a High-Resolution Simulation of a Transition from Shallow to Deep Cumulus Convection. *J. Atmos. Sci.*, **63**, 1895–1909, doi:10.1175/JAS3723.1.

Kucharik, C. J., and Coauthors, 2000: Testing the performance of a dynamic global ecosystem model: Water balance, carbon balance, and vegetation structure. *Global Biogeochem. Cycles*, **14**, 795–825, doi:10.1029/1999GB001138.

Kumar, A., F. Chen, D. Niyogi, J. G. Alfieri, M. Ek, and K. Mitchell, 2011: Evaluation of a Photosynthesis-Based Canopy Resistance Formulation in the Noah Land-Surface Model. *Boundary-Layer Meteorology*, **138**, 263–284, doi:10.1007/s10546-010-9559-z.

Lee, J. M., and M. Khairoutdinov, 2015: A Simplified Land Model (SLM) for use in cloud-resolving models: Formulation and evaluation. *J. Adv. Model. Earth Syst.*, **7**, 1368–1392, doi:10.1002/2014MS000419.

Lee, T. J., and R. A. Pielke, 1992: Estimating the Soil Surface Specific Humidity. *J. Appl. Meteor.*, **31**, 480–484, doi:10.1175/1520-0450(1992)031<0480:ETSSSH>2.0.CO;2.

Lin, X., D. A. Randall, and L. D. Fowler, 2000: Diurnal Variability of the Hydrologic Cycle and Radiative Fluxes: Comparisons between Observations and a GCM. *J. Climate*, **13**, 4159–4179, doi:10.1175/1520-0442(2000)013<4159:DVOTHC>2.0.CO;2.

Liu, C., and M. W. Moncrieff, 1998: A Numerical Study of the Diurnal Cycle of Tropical Oceanic Convection. *J. Atmos. Sci.*, **55**, 2329–2344, doi:10.1175/1520-0469(1998)055<2329:ANSOTD>2.0.CO;2.

——, and ——, 2004: Effects of Convectively Generated Gravity Waves and Rotation on the Organization of Convection. *J. Atmos. Sci.*, **61**, 2218–2227, doi:10.1175/1520-0469(2004)061<2218:EOCGGW>2.0.CO;2.

——, and ——, 2008: Explicitly simulated tropical convection over idealized warm pools. *J. Geophys. Res.*, **113**, D21121, doi:10.1029/2008JD010206.

Lu, T. X., J. W. Biggar, and D. R. Nielsen, 1994: Water movement in glass bead porous media: 2. Experiments of infiltration and finger flow. *Water Resour. Res.*, **30**, 3283–3290,

doi:10.1029/94WR00998.

Mahrt, L., 1991: Boundary-layer moisture regimes. *Q.J.R. Meteorol. Soc.*, **117**, 151–176, doi:10.1002/qj.49711749708.

Mapes, B. E., 1993: Gregarious Tropical Convection. *J. Atmos. Sci.*, **50**, 2026–2037, doi:10.1175/1520-0469(1993)050<2026:GTC>2.0.CO;2.

——, and R. A. Houze, 1993: Cloud Clusters and Superclusters over the Oceanic Warm Pool. *Mon. Wea. Rev.*, **121**, 1398–1416, doi:10.1175/1520-0493(1993)121<1398:CCASOT>2.0.CO;2.

——, T. T. Warner, and M. Xu, 2003: Diurnal Patterns of Rainfall in Northwestern South America. Part III: Diurnal Gravity Waves and Nocturnal Convection Offshore. *Mon. Wea. Rev.*, **131**, 830–844, doi:10.1175/1520-0493(2003)131<0830:DPORIN>2.0.CO;2.

Matsui, T., D. Mocko, M.-I. Lee, W.-K. Tao, M. J. Suarez, and R. A. Pielke, 2010: Ten-year climatology of summertime diurnal rainfall rate over the conterminous U.S. *Geophys. Res. Lett.*, **37**, L13807, doi:10.1029/2010GL044139.

McCaul, E. W., and C. Cohen, 2002: The Impact on Simulated Storm Structure and Intensity of Variations in the Mixed Layer and Moist Layer Depths. *Mon. Wea. Rev.*, **130**, 1722–1748, doi:10.1175/1520-0493(2002)130<1722:TIOSSS>2.0.CO;2.

McNider, R. T., and R. A. Pielke, 1984: Numerical Simulation of Slope and Mountain Flows. *J. Climate Appl. Meteor.*, **23**, 1441–1453, doi:10.1175/0733-3021-23.10.1441.

Miller, S. T. K., B. D. Keim, R. W. Talbot, and H. Mao, 2003: Sea breeze: Structure, forecasting, and impacts. *Rev. Geophys.*, **41**, 1011, doi:10.1029/2003RG000124.

Mocko, D. M., and Y. C. Sud, 2001: Refinements to SSiB with an Emphasis on Snow Physics: Evaluation and Validation Using GSWP and Valdai Data. *Earth Interact.*, **5**, 1–31, doi:10.1175/1087-3562(2001)005<0001:RTSWAE>2.0.CO;2.

Mori, S., and Coauthors, 2004: Diurnal Land–Sea Rainfall Peak Migration over Sumatera Island, Indonesian Maritime Continent, Observed by TRMM Satellite and Intensive Rawinsonde Soundings. *Mon. Wea. Rev.*, **132**, 2021–2039, doi:10.1175/1520-0493(2004)132<2021:DLRPMO>2.0.CO;2.

Muller, C. J., P. A. O'Gorman, and L. E. Back, 2011: Intensification of Precipitation Extremes with Warming in a Cloud-Resolving Model. *J. Climate*, **24**, 2784–2800, doi:10.1175/2011JCLI3876.1.

Nesbitt, S. W., and E. J. Zipser, 2003: The Diurnal Cycle of Rainfall and Convective Intensity according to Three Years of TRMM Measurements. *J. Climate*, **16**, 1456–1475, doi:10.1175/1520-0442(2003)016<1456:TDCORA>2.0.CO;2.

Nilsson, J., and K. A. Emanuel, 1999: Equilibrium atmospheres of a two-column radiative-convective

model. *Q.J.R. Meteorol. Soc.*, **125**, 2239–2264, doi:10.1002/qj.49712555814.

Niyogi, D. S., and S. Raman, 1997: Comparison of Four Different Stomatal Resistance Schemes Using FIFE Observations. *J. Appl. Meteor.*, **36**, 903–917, doi:10.1175/1520-0450(1997)036<0903:COFDSR>2.0.CO;2.

Noilhan, J., and J.-F. Mahfouf, 1996: The ISBA land surface parameterisation scheme. *Global and Planetary Change*, **13**, 145–159, doi:10.1016/0921-8181(95)00043-7.

Oleson, Keith, and Coauthors, 2010: Technical Description of version 4.0 of the Community Land Model (CLM). doi:10.5065/D6FB50WZ. http://dx.doi.org/10.5065/D6FB50WZ (Accessed February 16, 2016).

Patton, E. G., P. P. Sullivan, and C.-H. Moeng, 2005: The Influence of Idealized Heterogeneity on Wet and Dry Planetary Boundary Layers Coupled to the Land Surface. *J. Atmos. Sci.*, **62**, 2078–2097, doi:10.1175/JAS3465.1.

Petch, J. C., A. R. Brown, and M. E. B. Gray, 2002: The impact of horizontal resolution on the simulations of convective development over land. *Q.J.R. Meteorol. Soc.*, **128**, 2031–2044, doi:10.1256/003590002320603511.

Peters-Lidard, C. D., E. Blackburn, X. Liang, and E. F. Wood, 1998: The Effect of Soil Thermal Conductivity Parameterization on Surface Energy Fluxes and Temperatures. *J. Atmos. Sci.*, **55**, 1209–1224, doi:10.1175/1520-0469(1998)055<1209:TEOSTC>2.0.CO;2.

Philip, J. R., 1957: Evaporation, and moisture and heat fields in the soil. *J. Meteor.*, **14**, 354–366, doi:10.1175/1520-0469(1957)014<0354:EAMAHF>2.0.CO;2.

Pielke, R. A., 1974: A Three-Dimensional Numerical Model of the Sea Breezes Over South Florida. *Mon. Wea. Rev.*, **102**, 115–139, doi:10.1175/1520-0493(1974)102<0115:ATDNMO>2.0.CO;2.

——, 2001: Influence of the spatial distribution of vegetation and soils on the prediction of cumulus Convective rainfall. *Rev. Geophys.*, **39**, 151–177, doi:10.1029/1999RG000072.

Pierrehumbert, R. T., 1995: Thermostats, Radiator Fins, and the Local Runaway Greenhouse. *Journal of the Atmospheric Sciences*, **52**, 1784–1806, doi:10.1175/1520-0469(1995)052<1784:TRFATL>2.0.CO;2.

Pritchard, M. S., and R. C. J. Somerville, 2009a: Empirical orthogonal function analysis of the diurnal cycle of precipitation in a multi-scale climate model. *Geophysical Research Letters*, **36**, doi:10.1029/2008GL036964. http://doi.wiley.com/10.1029/2008GL036964 (Accessed February 17, 2016).

——, and ——, 2009b: Assessing the diurnal cycle of precipitation in a multi-scale climate model. *Journal of Advances in Modeling Earth Systems*, **2**, doi:10.3894/JAMES.2009.1.12. http://doi.wiley.com/10.3894/JAMES.2009.1.12 (Accessed February 17, 2016).

——, M. W. Moncrieff, and R. C. J. Somerville, 2011: Orogenic Propagating Precipitation Systems over the United States in a Global Climate Model with Embedded Explicit Convection. *Journal of the Atmospheric Sciences*, **68**, 1821–1840, doi:10.1175/2011JAS3699.1.

Qian, J.-H., 2008: Why Precipitation Is Mostly Concentrated over Islands in the Maritime Continent. *Journal of the Atmospheric Sciences*, **65**, 1428–1441, doi:10.1175/2007JAS2422.1.

Rabin, R. M., D. J. Stensrud, S. Stadler, P. J. Wetzel, and M. Gregory, 1990: Observed Effects of Landscape Variability on Convective Clouds. *Bull. Amer. Meteor. Soc.*, **71**, 272–280, doi:10.1175/1520-0477(1990)071<0272:OEOLVO>2.0.CO;2.

Randall, D. A., Harshvardhan, and D. A. Dazlich, 1991: Diurnal Variability of the Hydrologic Cycle in a General Circulation Model. *J. Atmos. Sci.*, **48**, 40–62, doi:10.1175/1520-0469(1991)048<0040:DVOTHC>2.0.CO;2.

Raymond, D. J., and X. Zeng, 2000: Instability and large-scale circulations in a two-column model of the tropical troposphere. *Q.J.R. Meteorol. Soc.*, **126**, 3117–3135, doi:10.1002/qj.49712657007.

Rennó, N. O., K. A. Emanuel, and P. H. Stone, 1994a: Radiative-convective model with an explicit hydrologic cycle: 1. Formulation and sensitivity to model parameters. *J. Geophys. Res.*, **99**, 14429–14441, doi:10.1029/94JD00020.

Rieck, M., C. Hohenegger, and C. C. van Heerwaarden, 2014: The Influence of Land Surface Heterogeneities on Cloud Size Development. *Monthly Weather Review*, **142**, 3830–3846, doi:10.1175/MWR-D-13-00354.1.

——, ——, and P. Gentine, 2015: The effect of moist convection on thermally induced mesoscale circulations: Moist Convection and Mesoscale Circulation. *Quarterly Journal of the Royal Meteorological Society*, **141**, 2418–2428, doi:10.1002/qj.2532.

Rio, C., F. Hourdin, J.-Y. Grandpeix, and J.-P. Lafore, 2009: Shifting the diurnal cycle of parameterized deep convection over land: DIURNAL CYCLE OF CONVECTION. *Geophysical Research Letters*, **36**, n/a – n/a, doi:10.1029/2008GL036779.

Rochetin, N., B. R. Lintner, K. L. Findell, A. H. Sobel, and P. Gentine, 2014: Radiative–Convective Equilibrium over a Land Surface. *J. Climate*, **27**, 8611–8629, doi:10.1175/JCLI-D-13-00654.1.

Romps, D. M., 2011: Response of Tropical Precipitation to Global Warming. *J. Atmos. Sci.*, **68**, 123–138, doi:10.1175/2010JAS3542.1.

Ronda, R. J., H. a. R. de Bruin, and A. a. M. Holtslag, 2001: Representation of the Canopy Conductance in Modeling the Surface Energy Budget for Low Vegetation. *J. Appl. Meteor.*, **40**, 1431–1444, doi:10.1175/1520-0450(2001)040<1431:ROTCCI>2.0.CO;2.

de Rooy, W. C., and Coauthors, 2013: Entrainment and detrainment in cumulus convection: an overview. *Quarterly Journal of the Royal Meteorological Society*, **139**, 1–19, doi:10.1002/qj.1959.

Ross, J. 1975. Radiative Transfer in Plant Communities, In: Vegetation and the Atmosphere, I. J.L. Ross (ed). Academic Press. pp 13-55

Sahoo, A. K., P. A. Dirmeyer, P. R. Houser, and M. Kafatos, 2008: A study of land surface processes using land surface models over the Little River Experimental Watershed, Georgia. *J. Geophys. Res.*, **113**, D20121, doi:10.1029/2007JD009671.

Saito, K., T. Keenan, G. Holland, and K. Puri, 2001: Numerical Simulation of the Diurnal Evolution of Tropical Island Convection over the Maritime Continent. *Mon. Wea. Rev.*, **129**, 378–400, doi:10.1175/1520-0493(2001)129<0378:NSOTDE>2.0.CO;2.

Sakaguchi, K., and X. Zeng, 2009: Effects of soil wetness, plant litter, and under-canopy atmospheric stability on ground evaporation in the Community Land Model (CLM3.5). *J. Geophys. Res.*, **114**, D01107, doi:10.1029/2008JD010834.

Sato, T., H. Miura, M. Satoh, Y. N. Takayabu, and Y. Wang, 2009: Diurnal Cycle of Precipitation in the Tropics Simulated in a Global Cloud-Resolving Model. *Journal of Climate*, **22**, 4809–4826, doi:10.1175/2009JCLI2890.1.

Schlemmer, L., and C. Hohenegger, 2014: The Formation of Wider and Deeper Clouds as a Result of Cold-Pool Dynamics. *Journal of the Atmospheric Sciences*, **71**, 2842–2858, doi:10.1175/JAS-D-13-0170.1.

——, ——, J. Schmidli, C. S. Bretherton, and C. Schär, 2011: An Idealized Cloud-Resolving Framework for the Study of Midlatitude Diurnal Convection over Land. *J. Atmos. Sci.*, **68**, 1041–1057, doi:10.1175/2010JAS3640.1.

Schneider, J. M., D. K. Fisher, R. L. Elliott, G. O. Brown, and C. P. Bahrmann, 2003: Spatiotemporal Variations in Soil Water: First Results from the ARM SGP CART Network. *J. Hydrometeor*, **4**, 106–120, doi:10.1175/1525-7541(2003)004<0106:SVISWF>2.0.CO;2.

Sellers, P. J., and J. L. Dorman, 1987: Testing the Simple Biosphere Model (SiB) Using Point Micrometeorological and Biophysical Data. *J. Climate Appl. Meteor.*, **26**, 622–651, doi:10.1175/1520-0450(1987)026<0622:TTSBMU>2.0.CO;2.

——, Y. Mintz, Y. C. Sud, and A. Dalcher, 1986: A Simple Biosphere Model (SIB) for Use within General Circulation Models. *J. Atmos. Sci.*, **43**, 505–531, doi:10.1175/1520-0469(1986)043<0505:ASBMFU>2.0.CO;2.

——, and Coauthors, 1996: A Revised Land Surface Parameterization (SiB2) for Atmospheric GCMS. Part I: Model Formulation. *J. Climate*, **9**, 676–705, doi:10.1175/1520-0442(1996)009<0676:ARLSPF>2.0.CO;2.

Shepherd, J. M., B. S. Ferrier, and P. S. Ray, 2001: Rainfall Morphology in Florida Convergence Zones:

A Numerical Study. *Mon. Wea. Rev.*, **129**, 177–197, doi:10.1175/1520-0493(2001)129<0177:RMIFCZ>2.0.CO;2.

Sherwood, S. C., 2004: Deep convective cloud-top heights and their thermodynamic control during CRYSTAL-FACE. *Journal of Geophysical Research*, **109**, doi:10.1029/2004JD004811. http://doi.wiley.com/10.1029/2004JD004811 (Accessed February 16, 2016).

——, and R. Wahrlich, 1999: Observed Evolution of Tropical Deep Convective Events and Their Environment. *Mon. Wea. Rev.*, **127**, 1777–1795, doi:10.1175/1520-0493(1999)127<1777:OEOTDC>2.0.CO;2.

Simpson, J. E., D. A. Mansfield, and J. R. Milford, 1977: Inland penetration of sea-breeze fronts. *Q.J.R. Meteorol. Soc.*, **103**, 47–76, doi:10.1002/qj.49710343504.

Singh, M. S., and P. A. O'Gorman, 2012: Upward Shift of the Atmospheric General Circulation under Global Warming: Theory and Simulations. *J. Climate*, **25**, 8259–8276, doi:10.1175/JCLI-D-11-00699.1.

Slingo, A., R. C. Wilderspin, and S. J. Brentnall, 1987: Simulation of the Diurnal Cycle of Outgoing Longwave Radiation with an Atmospheric GCM. *Mon. Wea. Rev.*, **115**, 1451–1457, doi:10.1175/1520-0493(1987)115<1451:SOTDCO>2.0.CO;2.

Stratton, R. A., and A. J. Stirling, 2012: Improving the diurnal cycle of convection in GCMs. *Quarterly Journal of the Royal Meteorological Society*, **138**, 1121–1134, doi:10.1002/qj.991.

Sui, C.-H., K.-M. Lau, Y. N. Takayabu, and D. A. Short, 1997: Diurnal Variations in Tropical Oceanic Cumulus Convection during TOGA COARE. *J. Atmos. Sci.*, **54**, 639–655, doi:10.1175/1520-0469(1997)054<0639:DVITOC>2.0.CO;2.

Tao, W.-K., and Coauthors, 2009: A Multiscale Modeling System: Developments, Applications, and Critical Issues. *Bulletin of the American Meteorological Society*, **90**, 515–534, doi:10.1175/2008BAMS2542.1.

Taylor, C. M., D. J. Parker, and P. P. Harris, 2007: An observational case study of mesoscale atmospheric circulations induced by soil moisture. *Geophys. Res. Lett.*, **34**, L15801, doi:10.1029/2007GL030572.

——, C. E. Birch, D. J. Parker, N. Dixon, F. Guichard, G. Nikulin, and G. M. S. Lister, 2013: Modeling soil moisture-precipitation feedback in the Sahel: Importance of spatial scale versus convective parameterization. *Geophys. Res. Lett.*, **40**, 2013GL058511, doi:10.1002/2013GL058511.

Tompkins, A. M., 2001: Organization of Tropical Convection in Low Vertical Wind Shears: The Role of Cold Pools. *J. Atmos. Sci.*, **58**, 1650–1672, doi:10.1175/1520-0469(2001)058<1650:OOTCIL>2.0.CO;2.

——, and G. C. Craig, 1998: Radiative–convective equilibrium in a three-dimensional cloud-ensemble

model. *Q.J.R. Meteorol. Soc.*, **124**, 2073–2097, doi:10.1002/qj.49712455013.

de Vries, D.A. 1963. Thermal Properties of Soils. In: W.R. van Wijk (editor) Physics of the Plant Environment. North-Holland, Amsterdam.

U.S. Dept. of Agriculture. Soil Conservation Service. Soil Survey Staff. 1951. Soil Survey Manual. U.S. Dept. of Agric. Handb. 18. U.S. Govt. Print. Off. Washington, DC. 503 pp., illus.

Wallace, J. M., 1975: Diurnal Variations in Precipitation and Thunderstorm Frequency over the Conterminous United States. *Mon. Wea. Rev.*, **103**, 406–419, doi:10.1175/1520-0493(1975)103<0406:DVIPAT>2.0.CO;2.

Wang, Y., L. Zhou, and K. Hamilton, 2007: Effect of Convective Entrainment/Detrainment on the Simulation of the Tropical Precipitation Diurnal Cycle*. *Monthly Weather Review*, **135**, 567–585, doi:10.1175/MWR3308.1.

Williams, E., and Coauthors, 2002: Contrasting convective regimes over the Amazon: Implications for cloud electrification. *J. Geophys. Res.*, **107**, 8082, doi:10.1029/2001JD000380.

Williams, E., T. Chan, and D. Boccippio, 2004: Islands as miniature continents: Another look at the land-ocean lightning contrast. *J. Geophys. Res.*, **109**, D16206, doi:10.1029/2003JD003833.

Wu, C.-M., B. Stevens, and A. Arakawa, 2009: What Controls the Transition from Shallow to Deep Convection? *J. Atmos. Sci.*, **66**, 1793–1806, doi:10.1175/2008JAS2945.1.

——, M.-H. Lo, W.-T. Chen, and C.-T. Lu, 2015: The impacts of heterogeneous land surface fluxes on the diurnal cycle precipitation: A framework for improving the GCM representation of land-atmosphere interactions. *J. Geophys. Res. Atmos.*, **120**, 2014JD023030, doi:10.1002/2014JD023030.

Xu, K.-M., and D. A. Randall, 1995: Impact of Interactive Radiative Transfer on the Macroscopic Behavior of Cumulus Ensembles. Part II: Mechanisms for Cloud-Radiation Interactions. *J. Atmos. Sci.*, **52**, 800–817, doi:10.1175/1520-0469(1995)052<0800:IOIRTO>2.0.CO;2.

Yang, G.-Y., and J. Slingo, 2001: The Diurnal Cycle in the Tropics. *Mon. Wea. Rev.*, **129**, 784–801, doi:10.1175/1520-0493(2001)129<0784:TDCITT>2.0.CO;2.

Yang, K., and Coauthors, 2008: Turbulent Flux Transfer over Bare-Soil Surfaces: Characteristics and Parameterization. *J. Appl. Meteor. Climatol.*, **47**, 276–290, doi:10.1175/2007JAMC1547.1.

Yang, S., and E. A. Smith, 2006: Mechanisms for Diurnal Variability of Global Tropical Rainfall Observed from TRMM. *J. Climate*, **19**, 5190–5226, doi:10.1175/JCLI3883.1.

Yang, Z.-L., 2004: *Modeling land surface processes in short-term weather and climate studies*. World Scientific Series on Meteorology of East Asia.

Zeng, X., 2001: Global Vegetation Root Distribution for Land Modeling. *J. Hydrometeor*, **2**, 525–530,

doi:10.1175/1525-7541(2001)002<0525:GVRDFL>2.0.CO;2.

——, and R. E. Dickinson, 1998: Effect of Surface Sublayer on Surface Skin Temperature and Fluxes. *J. Climate*, **11**, 537–550, doi:10.1175/1520-0442(1998)011<0537:EOSSOS>2.0.CO;2.

——, M. Barlage, R. E. Dickinson, Y. Dai, G. Wang, and K. Oleson, 2005: Treatment of Undercanopy Turbulence in Land Models. *J. Climate*, **18**, 5086–5094, doi:10.1175/JCLI3595.1.

Zhang, G. J., 2002: Convective quasi-equilibrium in midlatitude continental environment and its effect on convective parameterization. *J.-Geophys.-Res.*, **107**, ACL 12–1, doi:10.1029/2001JD001005.

Zhang, L., W. R. Dawes, and T. J. Hatton, 1996: Modelling hydrologic processes using a biophysically based model—application of WAVES to FIFE and HAPEX-MOBILHY. *Journal of Hydrology*, **185**, 147–169, doi:10.1016/0022-1694(95)03006-9.

Zhang, Y., and S. A. Klein, 2010: Mechanisms Affecting the Transition from Shallow to Deep Convection over Land: Inferences from Observations of the Diurnal Cycle Collected at the ARM Southern Great Plains Site. *Journal of the Atmospheric Sciences*, **67**, 2943–2959, doi:10.1175/2010JAS3366.1.

——, and Coauthors, 2008: On the diurnal cycle of deep convection, high-level cloud, and upper troposphere water vapor in the Multiscale Modeling Framework. *Journal of Geophysical Research*, **113**, doi:10.1029/2008JD009905. http://doi.wiley.com/10.1029/2008JD009905 (Accessed February 17, 2016).

Zhou, L., and Y. Wang, 2006: Tropical Rainfall Measuring Mission observation and regional model study of precipitation diurnal cycle in the New Guinean region. *J. Geophys. Res.*, **111**, D17104, doi:10.1029/2006JD007243.

Ziegler, C. L., T. J. Lee, and R. A. Pielke, 1997: Convective Initiation at the Dryline: A Modeling Study. *Mon. Wea. Rev.*, **125**, 1001–1026, doi:10.1175/1520-0493(1997)125<1001:CIATDA>2.0.CO;2.

Zipser, E. J., 1977: Mesoscale and Convective–Scale Downdrafts as Distinct Components of Squall-Line Structure. *Mon. Wea. Rev.*, **105**, 1568–1589, doi:10.1175/1520-0493(1977)105<1568:MACDAD>2.0.CO;2.

——, 2003: Some Views On "Hot Towers" after 50 Years of Tropical Field Programs and Two Years of TRMM Data. *Meteorological Monographs*, **29**, 49–49, doi:10.1175/0065-9401(2003)029<0049:CSVOHT>2.0.CO;2.

Zuidema, P., 2003: Convective Clouds over the Bay of Bengal. *Mon. Wea. Rev.*, **131**, 780–798, doi:10.1175/1520-0493(2003)131<0780:CCOTBO>2.0.CO;2.